Fabrication of thermally reversible self-healing CFRP composite through Diels-Alder bonding to maintain structural Integrity

Submitted in partial fulfilment of the requirements of the degree of

DOCTOR OF PHILOSOPHY

in

MECHANICAL ENGINEERING

By

GOTETI DHANARAJU

(Roll No: 719047)

Supervisor

Dr. B. SATISH BEN

(Professor)

Department of Mechanical Engineering

National Institute of Technology Warangal,

Warangal -506004, Telangana, India

February 2023

Dedicated to my family

NATIONAL INSTITUTE OF TECHNOLOGY WARANGAL (T.S.) INDIA 506 004

Certificate

This is to certify that the thesis entitled "**Fabrication of thermally reversible self-healing CFRP composite through Diels-Alder bonding to maintain structural Integrity**"**,** being submitted by **Mr. Goteti Dhanaraju** for the award of the degree of Doctor of Philosophy in Mechanical Engineering, is the record of bonafide research work carried out under my supervision. The thesis has fulfilled the requirements according to the regulations of this Institute and has reached the standards for submission. The results embodied in the thesis have not been submitted to any other University or Institute for the award of any degree.

Dr. B. Satish Ben
Research Supervisor
Professor
Department of Mechanical Engineering

Date:

Place: Warangal

NATIONAL INSTITUTE OF TECHNOLOGY
WARANGAL (T.S.) INDIA 506 004

Declaration

This is to certify that the work presented in the thesis entitled **"Fabrication of thermally reversible self-healing CFRP composite through Diels-Alder bonding to maintain structural Integrity",** is a bonafide work done by me under the supervision of Dr. B. Satish Ben and was not submitted elsewhere for the award of any degree.

I declare that this written submission represents my idea in my own words and where other's ideas or words have not been included. I have adequately cited and referenced the original sources. I also declare that I have adhered to all principles of academic honesty and integrity and have not misinterpreted or fabricated or falsified any idea/data/fact/source in my submission. I understand that any violation of the above will be a cause for disciplinary action by the Institute and can also evoke penal action from the sources which have thus not been properly cited or from whom proper permission has not taken when needed.

(Mr. Goteti Dhanaraju)

Date: Research Scholar

Place: Warangal (Roll No.719047)

Acknowledgement

It gives me immense pleasure to express my deep sense of gratitude and thanks to my beloved supervisor **Dr. B. Satish Ben**, Professor, Department of Mechanical Engineering, National Institute of Technology Warangal, for his invaluable guidance, support and suggestions. His knowledge, and suggestions, and discussions helped me to become a capable researcher. He has shown me the interesting side of this wonderful potential research area. His encouragement helped me to overcome the difficulties encountered in my research aswell in my life also. I am highly indebted to him for his expertise while sharing his knowledge, understanding, encouragement and patience.

I wish to express my sincere thanks to **Prof. N.V. Ramana Rao**, Director, NIT Warangal for his official support and encouragement. I am very much thankful to **Prof. V. Suresh Babu**, Head, Dept. of Mechanical Engineering for his constant encouragement, support andcooperation. I also express my sincere thanks to **Prof. A. Kumar** and **Prof. R. Narasimha Rao**, former Heads, Dept. of Mechanical Engineering for their constant encouragement, suggestions,support and cooperation.

I take this privilege to thank all my Doctoral Scrutiny Committee members, **Prof. K. V. Sai Srinadh**, Professor, Department of Mechanical Engineering, **Prof. R. Narasimha Rao**, Professor, Department of Mechanical Engineering and **Dr. P. Syam Prasad,** Professor, Department of physics for their detailed review, constructive suggestions and excellent advice during the progress of this research work.

I am highly indebted to **Prof. Srikanth Korla,** Design Section Head, Department of Mechanical Engineering for his valuable comments and guidance during semester presentations.

I am very much thankful to **Dr. Syed Ismail** Associate Professor**, Dr. G. Raghavendra** Assistant Professor Department of Mechanical Engineering and **Prof. M.J. Davidson,** Professor Departmentof Mechanical Engineering, for their guidance during course of project.

I would like to place on record my thanks to all the faculty and staff of Mechanical Engineering Department, NIT Warangal for the knowledge they have imparted to me.

I would like to express my sincere gratitude to **Science and Engineering Research Board (SERB)** New Delhi, INDIA, for providing the financial assistance during the course of current research work. [**Project No: EEQ/2020/000105** under DST-SERB Program 2020]

I am thankful to my student colleagues **Dr. Raj Kumar Pittala, Ms. G. Sivaparwati, Dr. Syam Kumar Chokka, Mr. Md. Babar Pasha, Mr. Satish, Mr. K. Naresh, Mr. Ch. Nikesh, Mr. B. Balaji, Mr. G B Amarnadh, Mr. Ajemra Suresh, Mr. G Chitti Babu, Mr. Bhargav, Mr. Ramana Reddy, Mr. M Raju, Mr. Ramesh, Mrs. Swapna** for the technical discussions that we had during my course work and research work. I would also like to thank my fellow research scholars from other departments, **Mr. Jayaram, Mr. Srinadh, Mr. Anil, Mr. Teja**. A very special thanks to my mentor **Dr. A. Gopala Krishna,** and my friends **Mrs. Divya Sri, Sk. Fareeduddin Baba, Mr. M. Deepak, Mr. A. Suribabu, Mr. Ch. Nukaraju** and all my well-wishers who were always there to support and encourage me.

A very special thanks to **IIT Bombay, CRF, Bangalore** and **Centre for Research & Instrumentation Facility** (**CRIF**)-NIT Warangal, for providing the technical assistanceto carry out some of the characterization analysis involved in my research work.

Words cannot express how grateful I am to my parents (my father **Mr. Goteti Satyanarayana**, my mother **Mrs. Durga)** for all of the sacrifices that they have made for my growth.Your prayers for me were what I am today. Finally, I render my respect to all my family members (my sister **Mrs. Sunitha,** my elder brother and his wife **Mr. Posiyya and Mrs. Amulya,** younger twin brothers **Ram, Lakshman,** my nephews and niece **Bhargav, Jithesh, Mohith** and **Likitha**) for giving me moral support and inspiration. They have motivated and helped me in my life. Also, I take this opportunity to thank all my relatives, friends and well-wishers who are part of this journey directly and indirectly.

Last but not the least; I want to express my deepest gratitude to **God Almighty** for giving me such a fulfilling life with the blessings of whom I believe nothing is impossible.

Goteti Dhanaraju

Abstract

Highly cross-linking polymers and fiber-reinforced composites (CFRP) have attained remarkable applicability in numerous structural applications such as automotive, marine, aerospace, wind, and sports industries due to their superior strength-to-weight ratio, lightweight, good corrosion, better thermal resistance and less manufacturing cost, etc. Epoxy resins are frequently used as a matrix for CFRP laminates due to their high glass transition temperature (Tg), chemical stability and stiffness unless these compounds are strengthened, for instance in the aerospace industry, they have a significant disadvantage: brittleness. As cracks are typically not apparent on the composite surface, the industry-standard periodically analyzes composite components using costly non-destructive techniques, such as ultrasound- or x-ray-based approaches. If a significant damaged area is found, components are disposed of, creating a lot of waste. On the other hand, expensive, invasive, and time-consuming approaches have been developed for on-site repair when damage is more limited but compromises structural stability. There is an option that entails repairing the damage that is already present, such as delamination and micro-cracks, before it progresses to catastrophic failure. This is precisely the reason behind the expanding research in the field of self-healing CFRP composites.

The majority of living organisms exhibit self-healing, which is an independent and intriguing process in nature. Inspired by biological systems from the past decades, researchers have explored how engineered materials can "self-heal" after being damaged externally. Self-healing thermosetting composite materials are an excellent technology and a cost-effective option which have the ability of linking moieties, to separate and reconstruct in response to a particular stimulus is important to the self-healing approach in thermosetting polymer. Reversible polymerization repairs microscopic cracks and completely restores the polymer original characteristics, and the process can be repeated numerous times.

Here, we report the remendability of the cross-linking polymers at the matrix as well as interface, which use Furan-Maleimide Diles-Alder (FMDA) adduct as reversible matrix to promotes self-healing capability and epoxy-hardener as irreversible matrix to retain strength. Furfuryl glycidyl ether (FGE) was synthesized and mixed with 4,4′-methylenebis (N-phenylmaleimide) (DPBMI) to prepare reversible matrix and DGEBA (epoxy resin), curing agent HY 906 (hardener) were used as irreversible matrix to synthesize thermally reversible polymer matrix. Under magnetic stimulation, 12 g DPBMI (0.027 mol) was diffused in 10.3 g FGE (0.054 mol) at 90 ^{o}C about 5 minutes mixed with 10.01 g DGEBA (35 wt. % in BMI, FGE and DGEBA compound followed by MHHPAcuring and degassing. The developed compound was poured into a silicon mould and cured using autoclave

at 85 ^{o}C / 8 h, 130 ^{o}C / 8 h, and 85 ^{o}C / 8 h. The molecular architecture of the synthesized self-healing resin was investigated using FTIR, NMR and DSC analysis. TDCB sample was used to evaluate self-healing performance in polymer composite.

The mechanical performance of self-healing composite was improved by reinforcing with GNPs and MWCNTs, but these are prone to agglomeration. Amine based silane functionalization is used to address GNP and MWCNT agglomeration. However, functionalization with a silane coupling agent, necessitates oxygenated chemical moieties named hydroxyl, carboxylic and epoxide connected to the nanoparticles surface to aid condensation and hydrolysis reaction in covalently linking silane group. Various oxidation times (0/48/60/72 h) was processed to maximize the exfoliation level of nanofillers. The GNPs and MWCNTs were oxidized with HNO_3 and silanized with APTES, followed by bismaleimide grafting and then dispersed evenly in the self-healing polymer matrix using a probe sonicator. To assess the impact of functionalization on laminated hybrid CFRP, the nanoparticles were initially diffused in a hardener/epoxy matrix using an ultrasonic-mechanical dual stirring process and then hybrid CFRP composite was prepared using a vacuum bagging technique and further assisted in autoclave curing.

Restoration of the structural integrity of damaged CFRP composite through thermally reversible Diels-Alder bonds with the exact interface between matrix/fiber is extremely desirable for manufacturing high-performance self-healing laminates. This work demonstrates the fabrication of functionalized MWCNT (with different weight ratios 0.5, 1.0, 1.5 wt.%) reinforced thermally reversible self-healing CFRP composite. The morphological changes, surface functional elements, elemental groups, and degradation of functionalized MWCNTs were characterized by FESEM/HR-TEM, FTIR, XRD, and TG-DTA analysis. The results demonstrated that CFRP reinforced with functionalized MWCNT enhanced the dispersion, exhibited 82% of healing efficiency and improvement in flexural strength - 82.65%, tensile strength - 98.9% compared to pure CFRP. FE-SEM fractography of composites indicated that nanotube pull-out was the predominant failure criteria in CFRP-pristine-MWCNTs whereas crack suppression and strong interface dominated in CFRP-MWCNTs due to strong interfacial interaction with the matrix. The CFRP interphases with reversible DA-bonds exhibited repeatable self-healing ability. The impact of initial damage and nanoparticle content on composite strength before and after fracture is also examined through flexural and I.E.T. technique. 1.0 wt.% of MWCNTs filler concentration and 85^{o}C/8 h, 130^{o}C/8 h, and 85^{o}C /8 h +2 bar healing condition are recommended to fabricate self-healing CFRP composite. The main objective of this paper is to investigate matrix/fiber/nanofillers interface junction healing properties of the CFRP composite before and after fracture, to re-form structural stability over the CFRP interface of the damaged area and also examine the average healing efficiency.

Table of Contents

List of Figures

List of Tables

List of Abbreviations

APTS	Triethoxysilane
ASTM	Society for Testing and Materials
Bm-MWCNT	Bismaleimide grafted Multiwalled Carbon Nanotubes
CFRP	Carbon Fibre Reinforced Polymer
DA	Diels-Alder
DGEBA	Diglycidylether of bisphenol-A
DI	Deionized water
DPBMI	Bismaleimide Formaldehyde 4,4-bismaleimide diephynylmethane
DSC	Differential Scanning Calorimetry
DTA	Differential Thermal Analysis
DY070	Accelerator
EDX	Energy Dispersive X-ray
FE-SEM	Field Emission Scanning Electron Microscope
FGE	Furfuryl Glycidyl Ether
FMDA	Furan maleimide based Diels Alder
FTIR	Fourier Transform Infrared Spectroscopy
GNP	Graphene Nano Platelets
GNPBm	Bismaleimide grafted Graphene Nanoplatelets
GNPOx	Oxidized Graphene Nanoplatelets
GNPSi	Silanized Graphene Nanoplatelets
HPC	Hybrid Polymer Composite
HR-TEM	High Resolution Transmission Electron Microscope
HW	Halder Wagner plots
HY906	TETA based amine hardener of viscosity 0.01 - 0.022 Pa.s at 25˚C
IET	Impulse Excitation Technique
ILSS	Inter laminar shear strength
LY556	DGEBA based epoxy resin of viscosity 10 - 12 Pa.s at 25˚C
MWCNT	Multiwalled Carbon Nanotubes

OAC	Oxidized followed by silanized MWCNTs
Ox-MWCNT	Oxidized Multiwalled Carbon Naotubes
Pr-MWCNT	Prstine Multiwalled Carbon Nanotubes
rDA	retro Diels-Alder
S.B.S	Short beam strength test
Si-MWCNT	Silanized Multiwalled Carbon Nanotubes
TDCB	Double Tapered Cantilever Beam
TGA	Thermogravimetric Analysis
UTM	Universal Testing Machin
w.o.f	Work of fracture
XRD	X-ray Diffraction
^{1H}NMR	Proton Nuclear Magnetic Resonance spectroscopy
^{13C}NMR	Proton Nuclear Magnetic Resonance spectroscopy

Chapter 1

Introduction

1.1 Motivation

Scientists have modified the characteristics of materials such as metals, polymers, alloys, and others, to meet the ever changing requirements of our world. Materials subjected to unexpected fractures and continuous degradation of properties during their service life. The objective therefore is to create novel technologies that can provide unique materials with improved safety, enhanced lifetime and less maintenance or a very less repairing costs. In the modern world finding innovative materials with long-term durability and crack avoidance was of extreme significance. Self-healing, according to S.R. White [1], a pioneer in the study of self-healing materials, is "the capacity to repair fracture and reestablish lost and degraded features or performance utilizing resources intrinsically available to the system."

Highly cross-linking polymers and fiber reinforced composites (CFRP) have attained remarkable applicability in numerous structural applications such as automotive, marine, aerospace, wind and sports industries due to their superior strength-to-weight ratio, lightweight, good corrosion, better thermal resistance and less manufacturing cost etc. Epoxy resins are frequently used as matrix for CFRP laminates due to their high glass transition temperature (Tg), chemical stability and stiffness, unless these compounds are strengthened, for instance in the aerospace industry they have a significant disadvantage: brittleness. As cracks are typically not apparent on the composite surface, the industry standard is to periodically analyze composite components using costly non-destructive techniques, such as ultrasound- or x-ray-based approaches. If a very significant damage area is found, components are simply changed and disposed, creating a lot of waste. On the other hand, expensive, invasive, and time-consuming approaches have been developed for on-site repair when damage is more limited but compromises the structural stability. There is an option, which entails repairing damage that is already present, such as delamination and micro-cracks, before it progresses to catastrophic failure. This is precisely the reason behind the expanding research in the field of self-healing CFRP composites.

Biological systems given another inspiration for designing materials with a longer service life, like human skins. The reaction of human skin to injuries is triggered by the blood clotting. Following that, additional biological substances are delivered to the affected area to promote skin regrowth and heal the wound. This method of recovery is considered to be self-healing, and it was intended to be the standard for engineering materials designed to be self-healing. The majority of

living organisms exhibit self-healing, which is an independent and intriguing process in nature. However, it is extremely challenging to create a self-healing material with all the features of the human skin due to its sophistication. Inspired from biological systems from the past decades, researchers have been explored how engineered materials can "self-heal" after being damaged externally. Structural defects are repaired by the methodical transfer of the repaired material and the polymerization-dependent mending process of the damaged site.

Restoration of structural integrity of damaged CFRP composite through thermally reversible Diels-Alder bonds with exact interface between matrix/fiber is extremely desirable for manufacturing of high performance self-healing laminates. Composite structures experience micro-cracks during service conditions and might not fulfill their functionality if the crack is not revamped. The cracking or breaking of a material starts at the microscopic level, and usually goes unnoticed until the material fails and requires mending. Traditional repairs are expensive, because to design (never two the same); to implement (removal from service or in-situ repair); to certify & monitor (additional inspection often required) throughout remaining operational life. There is a requirement to develop a method which enhances the functionality of the material without affecting its inherent properties. Thermally reversible self-healing carbon fiber reinforced polymer (CFRP) composites are an excellent technology and cost-effective option for non-reversible thermosetting applications and extends the service life of material.

1.2 Applications

The main objective of the self-healing technique is to restore the structural integrity after damage, extended functionality without effecting inherent properties, enhanced service conditions. According to these aspects, self-healing polymers and composites are finding applications in numerous fields such as paintings or coating industries, building constructions, automotive, aerospace applications, electronics industries and biological fields. For example, the world's first self-healing clear coat for automotive surfaces was marketed by Nissan Motor Co. Ltd. under the name Scratch Guard Coat [2]. According to the manufacturer, the created paint contains high elastic resin that stop scratches from penetrating a painted automotive surface. The complete healing process takes between 1-8 days, depending on the severity of the scratch and the temperature of the surrounding area. The Bayer Material Science [3] developed two component polyurethane clear coats under the trade names Desmophen and Desmodur. According to corporate

sources this coating repairs minor scratches when exposed to heat or sunlight, utilized dense polymer structure with flexible linkages to create paint. Self-healing anticorrosive coatings could be useful for structural metallic materials like steel, in order to achieve long-term service life with minimal maintenance costs.

Self-healing materials have a wide range of uses in the building industry. Concrete has long served as the foundation in the construction industry because of its strong compressive strength, heat resistance, and inexpensive. But because of its low tensile strength, poor design errors, poor material choices, and other environmental conditions, concrete is susceptible to micro-cracking. These defects serve as a host for additional foreign substances including carbonate, chlorine, and sulphur, which weaken the structure and the concrete. Controlling or repairing the micro-cracks while they are still in their early stages is one of the greatest ways to stop concrete deterioration. Due to their capacity to increase the lifespan of a structure, cementitious elements that can cure themselves have recently attracted interest from both academics and business. Self-healing can be accomplished by adding the appropriate healing agents to the concrete.

The aviation sector is the next industrial sector where self-healing material applications are anticipated. Composite materials are now used much more frequently in aircraft. Composites with hollow fiber reinforcement could be used to repair cracks or other defects. Space applications have benefited from the use of self-healing polymers. Although, structural components like aircraft frames and frames being built to withstand harsh weather conditions, thermal loads, and UV radiation, during service conditions may develop micro-voids and micro-cracks as a result of unforeseen circumstances. If these flaws are not fixed in time, they will degrade the components structural integrity and cause an early failure. Medical industries also use self-healing materials in other contexts. Artificial bone, artificial teeth, and other prosthetics may last longer if they are made with biocompatible self-healing composite. Self-healing rubber, which was recently discovered, might have uses in the toy sector.

Hydrogel, a 3D structure with a high moisture content, can be used to simulate soft tissues due to its adaptable structure. Because of their excellent rheological behavior and capacity to naturally repair damage, self-healing hydrogels have become more useful in tissue engineering during the last ten years. Injectable self-mending hydrogels have found relevance in cell treatment,

tumor therapy and injury healing [4]. Conductive hydrogels have also been utilized in tissue engineering to create cardiac muscles and neurons.

Self-healing methods are increasingly finding applications in a variety of industries. According to Grandview research survey of the self-healing market globally [5], the market was valued at $291.6 M in 2018 and is projected to increase at a CAGR of 46.5% from 2019 to 2025. The demand for self-healing polymers and fiber reinforced composites, as well as an increase in the demand for energy-efficient construction methods, are expected to increase growth. The survey even predicted that the expansion of polymers and fiber-reinforced composites will increase at a CAGR of 46.5% from 2019 to 2025, with the automotive, construction, transportation, and energy generating industries expected to contribute significantly to this expansion.

1.3 Diels-Alder covalent bonding

Although many self-healing materials have been created till now, it is still uncertain whether the fabrication methods that have been suggested are both economically viable and expandable to the industrial scales. Thermally reversible Diels-Alder intrinsic technique rely on covalent linkage, uses reversible chemical reactions to provide self-healing capabilities. Diels-Alder covalent bond cycloaddition is well-known for its simplicity, high efficacy, heat-repairability, and lack of the requirement for catalysts or other materials that can subsequently compromise the structural integrity of the polymer. The DA cycloaddition chemistry specifically activates two carbon-carbon bonds to result in a cyclic (bi-cyclic) product. When diene or dienophile linkage-containing monomers react, a cross-linked polymer is created. By raising the polymer's temperature to that required for the retro-DA reaction, cracks can be repaired. The heat applied encourages partial polymer chain separation, which enhances the mobility of each individual chain. New DA bonds develop when the liquid cools, and the chains re-crosslink. The DA covalent reaction's drawback is that it needs outside influences to unite the two damaged surfaces.

The Diels-Alder (DA) reaction is a stimulus-dependent, entirely reversible reaction among a dienophile and a diene that produces cyclohexene and returns to the dienophile at a higher temperature known as the rDA reaction (retro Diels-Alder) [6]. The DA reversible process can produce healing because, DA moieties are less strong than other covalent linkages. As a result,

when extreme loads are applied, cracks often spread across the DA moieties, and at high temperatures, these broken DA bonds might reconnect. Intrinsic healing, however, does not left any gaps after healing has been completed and other healing agent is not required to process healing [7].

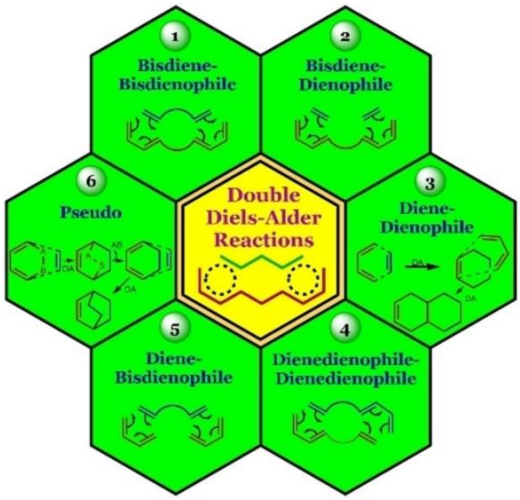

Figure 1.1: Classifications of Diels-Alder bonding [8]

1.4 Graphene nano platelets and Multiwalled carbon nanotubes

Numerous research attempts have been made over the past ten years to create multi - functional polymer nanocomposites that benefit from the distinct structural and mechanical characteristics of newly discovered graphitic forms like graphene nano platelets (GNPs) and multiwall carbon nanotubes (MWCNTs). Due to their outstanding thermal and electrical conductivities and favorable mechanical characteristics, GNPs and MWCNTs have prospective applications in the fields of gas storage, microelectronics, battery electrodes, catalyst supports etc. [9]. They are typically added to polymer matrices as fillers to change the physical properties of composites. They are simple to interlink and bundle together because of their nanoscale size, extremely low surface energy, and low bulk density. Therefore, homogenous GNP and MWCNT dispersion in polymer matrix is challenging.

Physical characteristics and composite structures don't always have a strong connection. Numerous efforts have been carried to identify the factors influencing the properties of polymer composite, including interfacial bonding between matrix and fillers, surface modification of fillers, and filler dispersion in matrix. It is found that chemically modified surface of GNPs and

MWCNTs can prevent filler aggregation, unwind bundles, and create strong bonding between the polymer matrix and fillers. Therefore, it is extremely desired to carry out surface chemical treatment of GNPs and MWCNTs to promote uniform filler dispersion in polymer matrix. Furthermore, the covalent connections between the fillers and matrix material can optimize the efficient stress transmission from the matrix to the GNP and MWCNT and thus enhance the mechanical features of polymer composites. The surface modification of GNP and MWCNT can be carried into two methods: direct adhesion of functional groups to the unmodified graphitic structure; attachment of oxygenated functional groups to the fillers. Carbon atoms mainly form sp^2 hybrid bonds on the sidewalls of GNPs and MWCNTs, which are electron-rich because of the highly delocalized π electrons, therefore it is easy to take part in surface modification.

The incorporation of oxygenated functional groups to the surface can be achieved by treating with HNO_3, H_2SO_4, O_5O_4, $KMnO_4$, plasma etc. [10]. The sp^2 bonding at sidewall defects can be easily attacked by oxidants, which causes the sp^2 hybridization to change into sp^3 hybridization. In order to maximize their potential as fillers for enhancing the characteristics of polymer composites, it is essential to find a balance between the surface graphitic structures and aspect ratio of GNP and MWCNT as well as adhering chemical moieties with strong affinities to matrix materials. Due to their bi-functionality, silane coupling agents are well known for being an excellent choice for linking both inorganic fillers and polymer matrix. Without affecting the filler graphitic structure, the silane coating on GNPs/MWCNTs might trigger further reactions with the polymeric matrix. Therefore, a comprehensive investigation of GNP and MWCNT silanization is important.

1.5 Fiber reinforced polymer composites

Composite material is a structural substance made up of two or more macroscopically joined parts that do not dissolve in one another. The constituent components have significantly different characteristics as well as chemically separate phases. Composite materials are technically heterogeneous at the microscopic level and statistically homogeneous at the macroscopic level. Due to the composites inherent characteristics, its properties are superior to those of its individual elements. Carbon fiber-reinforced polymer (CFRP) composites have recently been used in a wide range of industries including aerospace, automotive and naval due to their lightweight, high

strength/stiffness towards weight ratio, good corrosion resilience, excellent thermal resistance and low manufacturing cost etc.

Composites are divided into three categories based on type of matrix: metal matrix, polymer matrix, and ceramic matrix composites. Similar based depending on type of reinforcement, they have been categorized as particle reinforced and fiber reinforced composites. polymer composites are further divided into thermoplastic and thermosetting polymer composites and fiber reinforced composites are further divided into uni-directional and bi-directional continuous fiber composites. The main function of the reinforcement is to carrying loads/stresses, contributing to desirable characteristics, and transferring strength to matrix material. The matrix component is responsible for binding fibers together, shielding them from the outside atmosphere, distributing loads uniformly among fibers, and producing good surface finish to the composite.

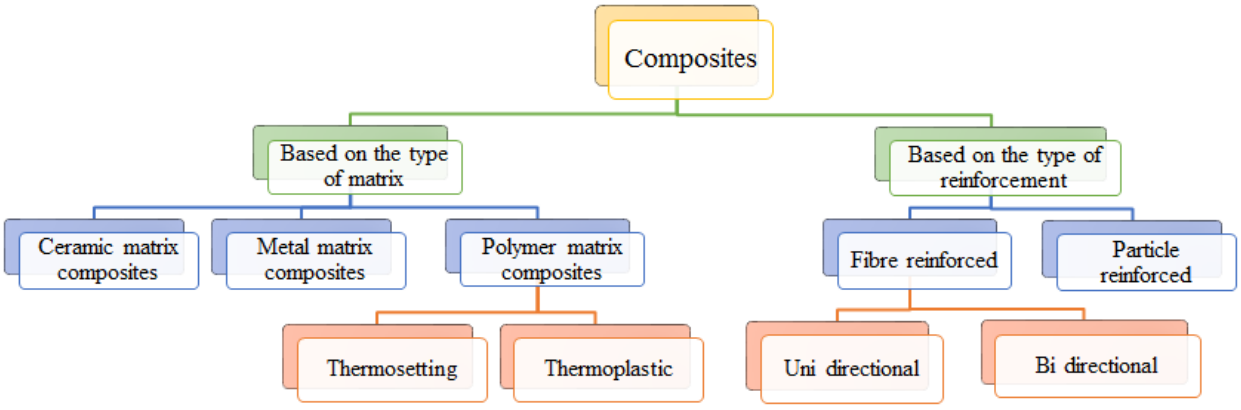

Figure 1.2: Classification of composites

1.6 Organization of the Thesis

The outline of the thesis is organized as follows.

Chapter 1: In this chapter, motivation behind the current research work and the applications of the work are explained. Different terms related to current work have been introduced and discussed.

Chapter 2: Provides brief literature review on the common types of damages in polymer composites and different self-healing mechanisms with major focus on the Diels-Alder self-healing mechanism. Furan-maleimide self-healing resin preparation, GNP/MWCNT silane and

maleimide functionalization, mechanical and self-healing performance of GNP/MWCNT reinforced epoxy composites have been discussed.

Chapter 3: This chapter deals with the materials and synthesis procedures involved in the development of thermally reversible self-healing resin and discusses the effect of different stoichiometric ratios of resin by various epoxy wt.%. The characterization techniques used to analyze the developed polymer composite have been presented. A brief discussion on the characterization procedures and the equations used to find different properties have been discussed.

Chapter 4: This chapter describes the exfoliation level effect of different oxidation times (48/60/72 h) of graphene nano platelets (GNP) and multiwalled carbon nanotubes (MWCNT). The oxidized GNP/MWCNT was functionalized with APTES silane agent followed by maleimide grafting was used as reinforcement. The characterization techniques used to analyze effective grafting of silane followed by maleimide have been presented.

Chapter 5: Discusses the effect of functionalized GNP/MWCNT concentration on the mechanical properties (Tensile, Flexural, shear strength) of carbon fiber reinforced epoxy composite. Brief discussion on the damping characterization of GNP/MWCNT reinforced CFRP have been presented.

Chapter 6: Discusses the effect of functionalized GNP/MWCNT concentration on the flexural strength and self-healing efficiency of carbon fiber reinforced epoxy composite. Brief discussion on the damping characterization of capsules reinforced CFRP and pure epoxy composites have been presented.

Chapter 7: Discusses the overall conclusions of the study and presents the scope for future works.

Chapter 2

Literature Review

This chapter discusses the fundamentals of self-healing materials as well as previous findings conducted by various researchers on the self-healing performance assessment of thermosetting polymer composites. This chapter, in particular, focuses on thermally reversible self-healing strategies and briefly describes the techniques employed to determine the healing efficiency.

2.1 Various damages in polymer composites

Because of the inherent properties of the materials and the manufacturing process, some flaws may already exist in the composites before they are placed into service. Under service, the existing defects intensify and further defects surface. Due to the anisotropic structure of CFRP composites, damage and failure can take many distinct and complicated forms. The main forms of CFRP composite damage mechanisms will be briefly discussed in this section as they relate to loading conditions as sown in Figure 2.1.

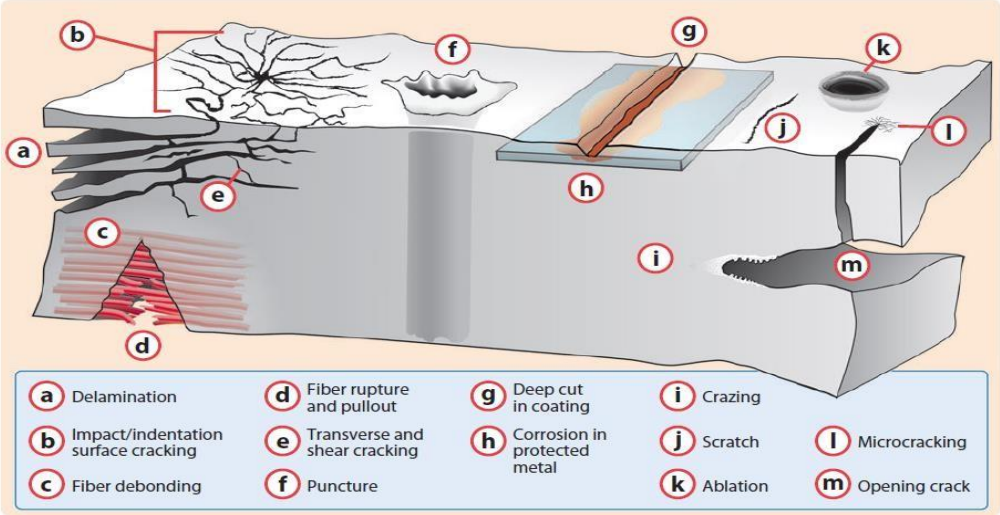

Figure 2.1 Various damages in polymer composite [13]

We begin with fiber breaking, a fundamental form of damage process. It is an important energy-absorbing mechanism that typically occurs at high velocity [11]. High stress intensity or maximum bending stress would occur during a through-thickness impact event, which would result in fiber breaking. This kind of failure can be located using resistance change. Carbon fibers start to deform elastically under severe tension and breakage of some weaker fibers results in a considerable increase in resistance. The broken fibers remain intact and are unable to transfer load to the unbroken ones if the strain is still high enough throughout the unloading phase. The

interaction of damaged fibers as the strain decreases to a low level would be the primary reason for the resistance shift, which is significant [12]. Therefore, the resistance restoration is caused by the restoration of elastic deformation which is not very significant.

A more frequent type of damage mechanism is matrix damage. It is a severe type of failure, because it reduces the load carrying capacity of CFRP composites up to 50% [14]. Matrix damage primarily consists of two types. One is caused by extremely high shear stress, and the cracks are angled at roughly 45 degrees to the mid-surface. Since it results in increased fiber-to-fiber contact, which lowers resistivity, this kind of failure can also be identified by a change in resistance. Another kind matrix damage attributed due to excessive in-plane normal stress. Cross-ply cracks develop transverse to the laminate plane when the stress is greater than the plies tensile strength [15].

Another typical damage mechanism is delamination, which is the dissociation of the individual plies caused by deboning at the matrix-fiber interface attributes to significant reduction in compression strength [16]. Delamination frequently occurs on multi-directional composites at the junction of fibers with multiple orientations. Initial damage may occur at the interfaces more frequently if the interface's bond strength is lower than the fracture strengths of both the matrix and the fibers or if force is concentrated on the broken fibers. Additionally, unidirectional composites are vulnerable to delamination. It separates several fiber layers and expands parallel to the direction of the fibers. It damages the network structure inside composites, which interferes with transverse conduction, breaking the fiber-to-fiber contact. Overall, delamination reduces the durability of composites and is typically invisible and extremely challenging to detect using traditional methods.

In order to increase structural integrity, prevent failure, and increase the component's service life, numerous researchers have employed ideas like self-healing, self-lubricating, and self-cleaning etc. Damage detection and self-healing are both the capabilities of self-healing materials. Inspired from autonomous healing systems in biological structure, constant efforts are being made by researchers to integrate these self-healing principles in structural applications of the polymer composites.

2.2 Self-healing materials and types of self-healing techniques

Self-healing materials are artificially created smart materials with the capacity to reform the microscopic cracks that appear on a structure without any human involvement. Biomimetic healing, autonomous healing, self-repair and self-mending are the substitute words used to define the characteristics of self-healing materials. Numerous examples of self-healing are found in biology. For instance, a cut or injury on the skin immediately starts the healing process. Depending on the type and size of damage, the skin will reconstruct itself within a day or week. Three phases: inflammation response, cell proliferation, and remodeling which together provide a brief explanation of the Self-healing process in biological systems [17]. The three phases of both biological and synthetic self-healing systems are shown in figure 2.2. Similar to biological systems, the self-healing in man-made materials can be achieved in chain cleavage, reactive chain ends to contact and bonds reformation.

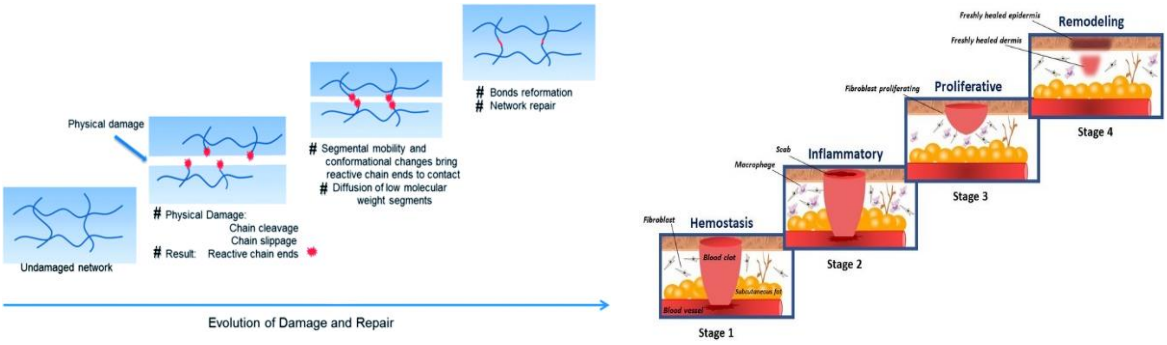

Figure 2.2 Schematic illustration of damage to repair in biological and synthetic routes [17,18]

There are currently two methods that are frequently used to treat internal micro-nano fractures. Extrinsic healing systems; [19] contain a healing agent that is enclosed in a polymer matrix, while intrinsic healing systems; [20] produce numerous intrinsic reversible covalent bond that reconstruct the fracture when stimulated. Micro-encapsulation [21] microvascular networks [22] and hollow fibers [23] are the examples of extrinsic healing mechanisms and Supra-molecular interactions [24], Host-guest chemistry [25], thermally reversible Diels-Alder bonds [26] are the examples of intrinsic healing system.

In encapsulation approach, healing agent is embedded in to the polymer matrix, when crack initiated the capsule subjected to breakage and releases the substance in to the crack region and

heal the crack surface. But they, cannot be returned to their monomeric, oligomeric, or cross-linked states. Extrinsic healing is therefore dependent on a liquid state healing agent as a separate phase in matrix, which has significant limits in terms of one-time healing and synthesis complexities [27]. One of the intrinsic self-healing techniques Diels-Alder chemistry is popular due to its simplicity, high efficacy, heat-repairability, and lack of dependence on a catalyst or other materials. The Diels-Alder (DA) reaction is a stimulus-dependent, entirely reversible reaction among a dienophile and a diene that produces cyclohexene and returns to the dienophile at a higher temperature known as the rDA (retro Diels-Alder) reaction [28].

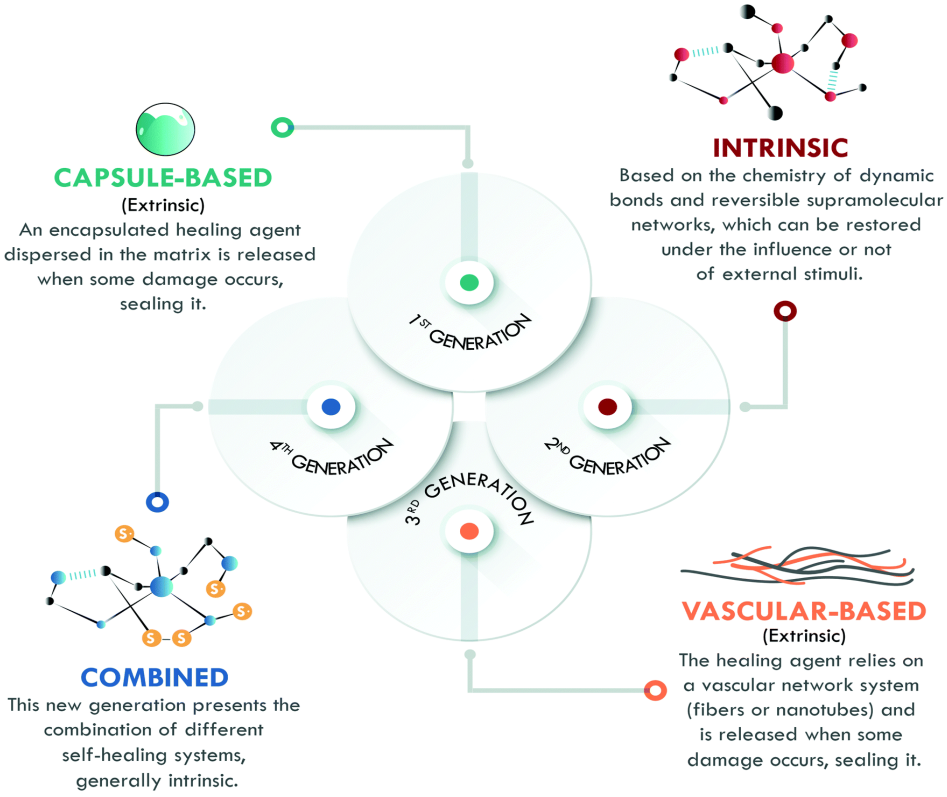

Figure 2.3 Evolution of self-healing approaches [28]

2.2.1 Extrinsic self-healing approach

One of the promising extrinsic self-healing approach is encapsulation based healing system, White et al. [29] were the first to present the idea of capsule-based self-healing. DCPD-Dicyclopentadiene was used as a healing agent in this investigation and was enclosed in a PUF-poly urea formaldehyde shell. The healing substance from the DCPD capsules releases whenever

the crack comes into contact with them, reacting with Grubb's catalyst to seal the crack through polymerization. The healing can be accomplished by embedding either a single microcapsule carrying a catalyst for healing or two capsules each having a distinct healing agent in the host material. Numerous studies have been done to examine the self-healing behaviour of various healing agents, including isocyanates [30], 5-ethylidene-2-norbornene (ENB) [31], paraffin [32], polydimethylsiloxane [33], and epoxy [34].

The arteries in the human body provided as an inspiration for the concept of a vascular network-based healing mechanism. The three kinds of vascular networks such as 1D, 2D, and 3D are being developed with the intention of promoting multiple healing. Hollow fiber-based healing systems are also referred to as 1D vascular network systems. Similar to capsules, the 1D network technique will encapsulate the healing agent in hollow tubes with the help of capillary action, surface pores, or vacuum support [13]. To achieve self-healing functionality, the open end of the healing agent tube will be sealed after filling, and the tube will be merged with the polymer matrix. This hollow fiber healing technique was first used by Dry et al. [35] to repair concrete cracks. Trask et al. [36] studied on the optimization of the hollow fiber production method resulted in the manufacture of ideal hollow glass fibers with a hollowness of around 65%, ranging in size from 30 to 100 m. The method is primarily constrained by the size of the hollow fibers, how they are distributed throughout the matrix material, and how this affects mechanical characteristics.

Some of the techniques that can be used to create vascular structures include soft lithography, fugitive inks, laser micromachining, and 3D printing [37]. After producing, healing agent will be introduced via syringe or pump into the vascular network [38]. Using the direct ink writing approach, Toohey et al. [39] created 3D vascular structure using Grubb's catalyst and DCPD as the healing compound and up to seven healing cycles, they showed good healing efficiency. In a later version of the design, Hansen et al. [40] included the monomer and catalyst in two separated vascular structure and showed good healing efficiency up to 30 healing cycles. Further refining the design led to the 100% healing efficiency, according to Patrick et al. [41]. The microcapsules based self-healing approach frequently performs healing well and can trigger healing function is only as effective as the amount of integrated healing agent in the composites, which limits the autonomous healing response. Additionally, the healing agent is often a liquid

phase that does not offer reinforcement and leaves a void after capsule rupture, which might subsequently lower the composite fracture strength [42].

2.2.2 Intrinsic self-healing approach

In contrast to micro-capsulation and vascular self-healing procedures, intrinsic approaches do not require the pre-embedding of the healing substances into the polymer matrix. Instead, healing is accomplished by the host polymer hidden healing activity with the aid of macromolecular processes. Intrinsic healing systems are broadly classified as, healing based on dynamic covalent bonds such as reversible Diels-Alder bonds and healing based on non-covalent bonds such as supramolecular interactions. Intrinsic self-mending materials are intended with implicit repeatable reform capability after mechanical or thermal damages where the habitation of healing agent and catalyst are not needful. Intrinsic self-healing also known as stimuli-responsive self-mending, prescribes some external stimulus such as thermal, electrical and photochemical to trigger micro-nano crack healing activity [43]. Due to tiny T_g of polymers, where cooling and heating activity trigger to molecular randominasation, interdiffusion, reamalgamation etc., has an advantage to attain molecular level intrinsic mending structure [44]. Amongst the intrinsic self-healing polymers, upmost earlier explorations were focused on developing self-healing mechanisms evolved from thermal stimulation.

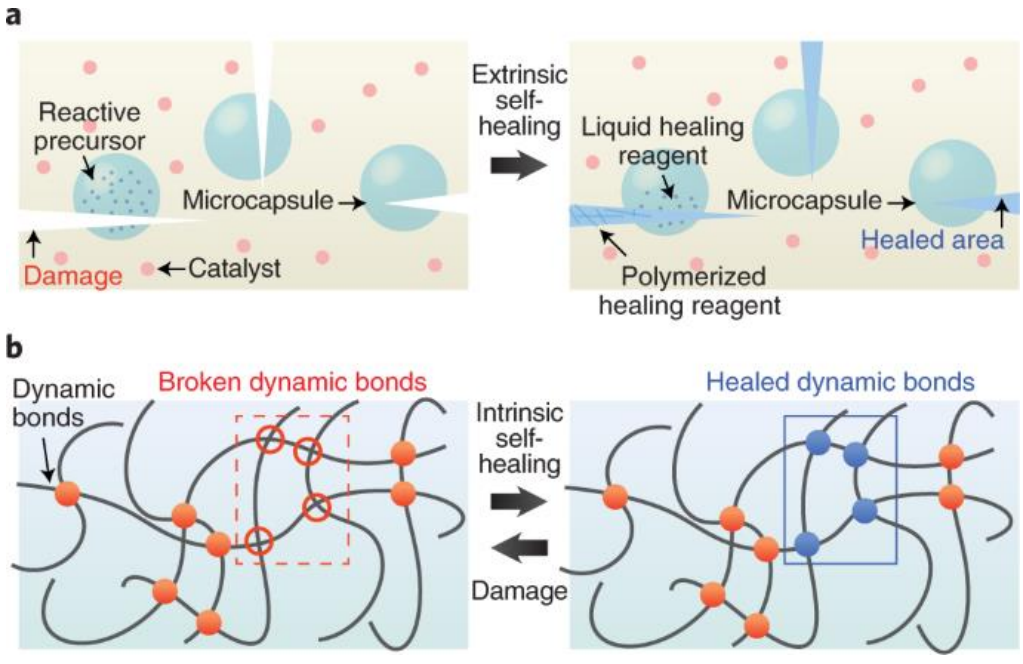

Figure 2.4 (a) Extrinsic and (b) Intrinsic self-healing approaches healing mechanism [28]

2.2.2.1 Non-covalent bonds (Supra-molecular chemistry)

Researches founded that noncovalent bond included polymeric materials are proficient of achieving self-healing cycles, which is a much needed in practical application. Supramolecular polymer chemistry networks have been illustrated to have the potential to reform without the requisite for external material component or the use of trigger stimuli [45]. According to the group of noncovalent bonds engaged in self-healing, the self- healing networks are categorized as follows: self-healing structure through hydrogen bonding [46] self-healing structure through π-π stacking interaction [47] self-healing structure through metal-ligand interaction [48], self-healing structure through ionomer [49].

Biyani et al. [50] designed, a revised cellulose nanocrystals (CNCs) based light-mendable supramolecular nanocomposite. UPy end-group was employed to end-functionalize the poly(ethylene-co-butylene) (PEB) matrix, in addition to that it modifies CNC surface which appears as nanofillers. Anderson et al. [51] described the DNA base-pair, ureido-7-deazaguanine (DeUG) and mimics 2,7-diamidonaphthyridine (DAN) having high-fidelity, high-affinity quadruple hydrogen-bonding supramolecular coupling agents. The proposed Dan-DeUG supramolecular network is category of improved DNA base-pair, exhibiting greater affinity and stability than other pairs like adenine-thymine and guanine-cytosine.

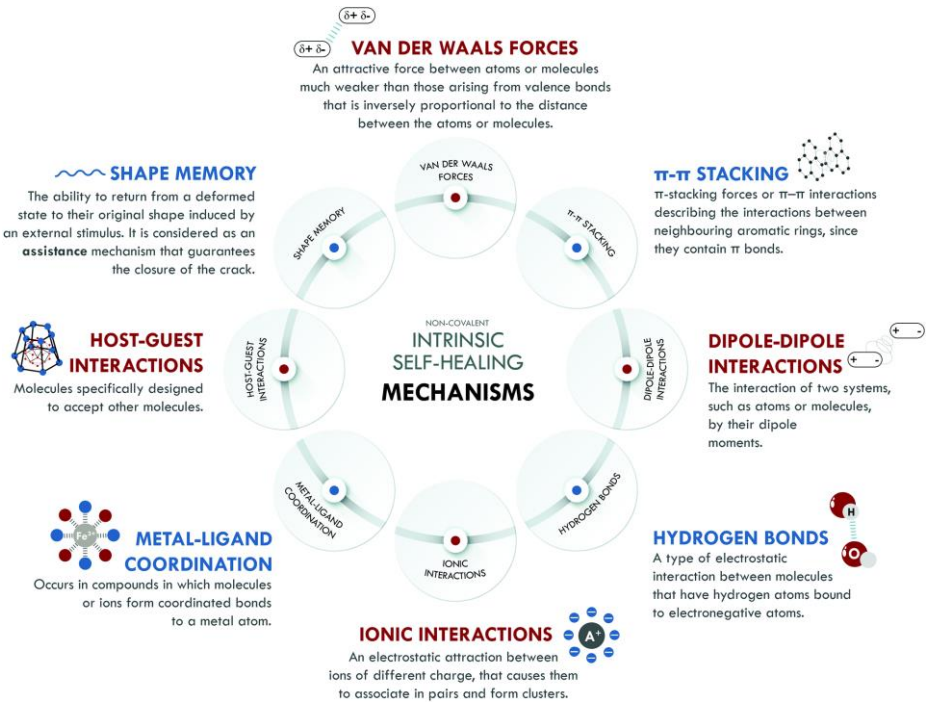

Figure 2.5 Types of non-covalent intrinsic self-healing mechanisms [28]

Further π-π stacking non-covalent interaction between aromatic rings has been adapted self-healing smart material synthesis. In an π-π stacking interaction system, end-capped π-electron deficient batch communicate with backbone of π-electron rich leads to the thermally stimuli reversible network. Generally, the pyrenyl group (electron rich) end-capped polyamide chain and co-polyimide (electron poor) chain folding, exhibits π-π stacking interaction chain reaction. Burattini et al. [48] combined pyrenyl groups with electron-rich di-imide groups which were electron-poor, in order to accomplish self-healing in elastomers.

On the other side, supramolecular based metal-ligand coordination polymer can exhibit self-healing behavior. Schubert et al. [52] designed metallo-supramolecular polymer using 2,2':6,2"-terpyridine (tpy) ligand to Fe(II) with the aid of facile coordination. Further this tpy moieties are associated through diethylene glycol bridge and the resulting were reacted with equimolar amount of $FeCl_2$ leaves a purple soluble water. This obtained polymer chain deconstructed by HEDTA treatment, results quantitative de-complexation. Holten Andersen et al. [53] designed a simple stepwise approach for fabrication of self-healing polymer by engaging prebinding Fe3+ catechol complexes. They combined Fe3+ ions and catechol-amended PEG polymer (cPEG) at small pH value and with the NaOH supplement the pH value increased to desired level, that results without iron hydroxide precipitation structure. The originated catechol-Fe3+ cross-linked polymer gel exhibits good elastic moduli as well as excellent self-healing properties.

2.2.2.2 Covalent bonds (Diels-Alder chemistry)

Chen et al. [54] created the first repairable polymers based on dynamic covalent connections with the use of external stimulus. As the healing process happens through macromolecular interactions, it is essential to maintain the proper chemicals at the nanometer level in order to have reversible bonding and consequently to initiate the healing action. To accomplish self-healing functionality, it is always important to bring injured parts back into contact. The type of external stimulus used, chain mobility and entanglement, the ability to reversibly polymerize, are the factors to impact healing functionality. The DA cycloaddition substance specifically activates two carbon-carbon bonds to result in a cyclic (bi-cyclic) product. When diene or dienophile linkage-containing monomers react, a cross-linked polymer is created. By heating the polymer to the level required

for the reversible DA reaction, cracks can be repaired. The applied heat encourages partial polymeric chains splitting, which enhances the mobility of each individual chain. New DA bonds develop when the liquid cools, and the chains re-crosslink [55]. The DA covalent reaction has the limitation that the two fracture surfaces must be stimulated externally in order to achieve self-healing functionality.

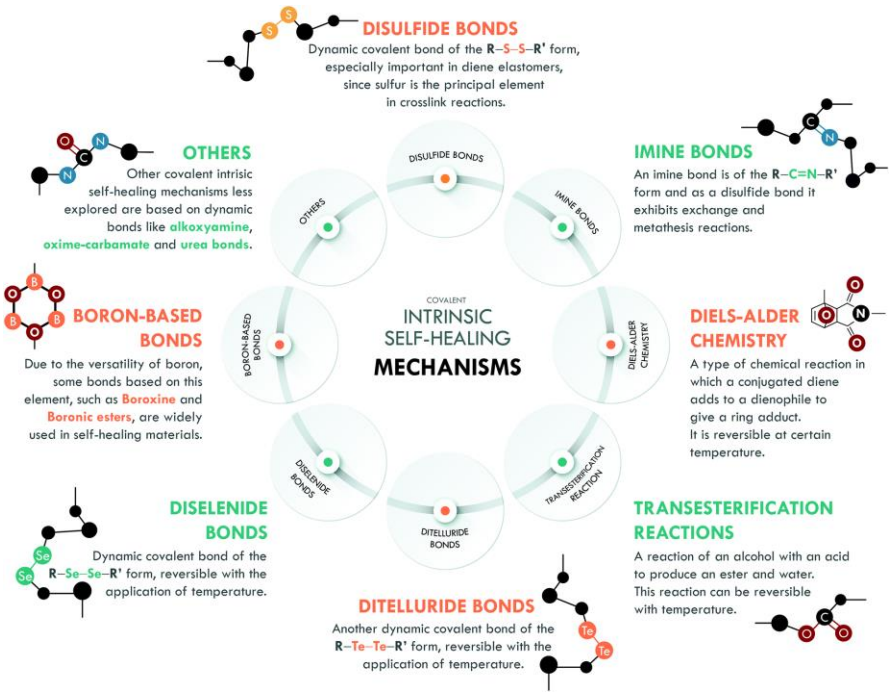

Figure 2.6 Types of covalent intrinsic self-healing mechanism [28]

2.3 Diels-Alder (furan-maleimide) based self-healing epoxy composite

Due to their high strength to weight ratio and strong corrosion resistance, epoxy-based thermosetting polymers are used in the transportation, energy, and automotive industries. But due to their inherent brittleness, they are prone to micro-cracks. In recent years, several self-healing techniques have been used on epoxy composites to prevent the cracks progression and extend the component life by self-healing the damage. In their study of the theory behind polymer crack healing, Wool R P et al. [56] conducted an in-depth analysis. They noted that the healing process involves five stages: (a) surface rearrangement, which influences preliminary diffusion function followed by topological feature; (b) surface approach, associated to healing trends; (c) wetting; (d) diffusion, which is the primary controlling factor that regulates recovery of mechanical

characteristics; and (e) randomization, ensuring elimination of cracking interface. Furthermore, Kim and Wool et al. [57] suggested a microscopic model for the final two phases based on the repetition model, which depicts longitudinal network diffusion as the cause of crack mending.

In order to assess crack-healing behavior, Jud and Kaush et al. [58] tested a variety of PMMA -polymethyl methacrylate and MMA-MEA copolymer- polymethyl methacrylate-comethyl ethylacrylate samples with varying molecular weights and levels of copolymerization. By heating samples over the glass transition temperature and applying a modest pressure, they achieved crack healing. It was discovered that during short-term loading studies, complete resistance was recovered. It is important to keep in mind that crack healing only occurs at or above the glass transition temperature. In order to lower the glass transition temperature of PMMA, it was subjected to methanol and ethanol treatments by Lin et al. [59]. They discovered that there are two separate stages for crack healing: the first one pertaining to the progressive healing owing to wetness, and the second connected to diffusion improvement of the quality of healing behavior.

2.3.1 Thermally reversible bonds

Thermally reversible crosslinking behavior, has been known for a while. In order to create healable polymers, Wudl et al. [60] paired this with the idea of "self-healing". They used the Diels-Alder (DA) process to create highly cross-linked polymeric polymers using multi-furan and multi-maleimide. The "intermonomer" connections separate at temperatures over 120 °C (relating to the retro-DA reaction), but they reattach when the temperature drops (i.e. DA reaction). This procedure can be employed to repair broken portions of the polymers and is completely reversible. The polymers are translucent and have mechanical qualities that are similar to those of unsaturated polyester and commercial epoxy. It is theoretically possible to mend cracks indefinitely without the use of extra catalysts, monomers, or other surface treatments.

Wudl's methodology was changed in a later work by Liu and Hsieh et al. [61]. Utilizing epoxy compounds as precursors, the multifunctional furan and maleimide molecules were made utilizing straightforward processes. In order to include the beneficial properties of epoxy resins, such as solvent and chemical stability, electrical and thermal properties, and good adhesion to their corresponding cured polymers, the furan/maleimide monomers were infused with epoxy-based compounds. In addition, Liu and Chen et al. [62] created polyamides with furan pendent groups (PA-F) by using a Michael addition reaction to combine furfuryl amine with polyamides

containing maleimide (PA-MI). Through the use of the DA and retro-DA reactions, thermally reversible cross-linked polyamides of the PA-MI and PA-F polyamides were produced. The thermo-reversible cross-linked polyamides also exhibited the ability to self-repair and restoration of mechanical properties.

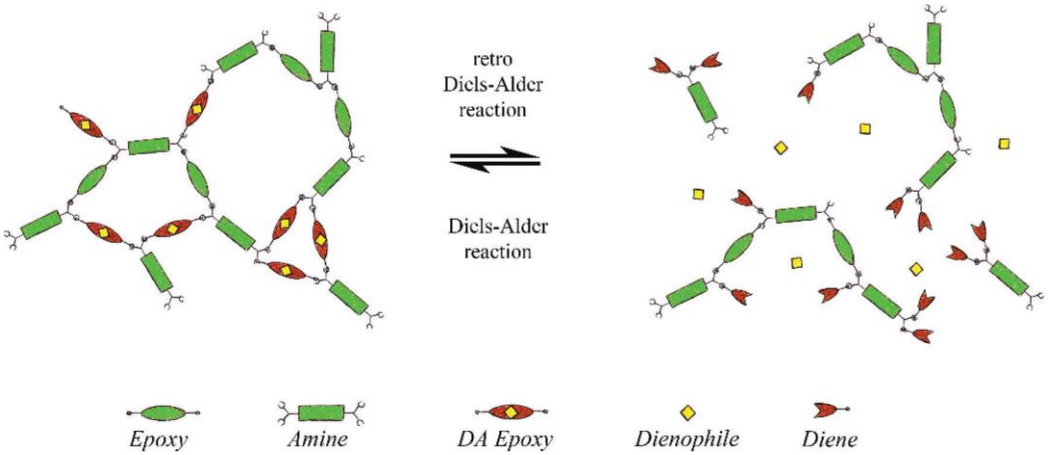

Figure 2.7. Self-healing epoxy network [55]

Characterization of healing efficiency is required in order to calculate the extent of structural recovery after injuries have been corrected, but there is currently no established testing protocol. Sometimes, various testing techniques produce different results. Wudl's team measured thermally reversible cross-linked polymers self-healing efficiency from compact tension test (CT) through fracture toughness recovery. As the starting crack spread along the specimen's central plane under the critical stress, data for the virgin and healed fracture toughness were calculated. In spite of the challenges in precise fracture surface and pre-notching complexities, Plaisted and Nemat-Nasser et al. [63] used double cleavage drilled compression (DCDC) to assess the mending efficiency of the reversible cross-linked polymer based on Diels-Alder bonding. The testing geometry permitted for progressive control ability to prevent crack propagation so that the broken sample survived the test intact before healing, to straighten the fracture surfaces.

2.3.2 Synthesis of furfuryl glycidyl ether (FGE)

Tian et al. [64] synthesized furfuryl glycidyl ether through a two-step process, to fabricate epoxy composite with high intrinsic self-healing efficiency with each FGE molecules contained one epoxide and one furan group. N,N-(4,4-diphenylmethane) maleimide and

methylhexahydrophthalic anhydride were used to cure the FGE before it was polymerized with two different kinds of intermonomer links. Specifically, thermo-irreversible bonds from the interaction of anhydride and epoxide groups and thermo-reversible Diels-Alder (DA) bonds from the interaction of maleimide and furan groups. These two different kinds of bonding give the healing functionality and load carrying capacity to the polymer, respectively. Lower activation energy is required for FGE to react with maleimide, and the resulting DA bonds are more reversible. They utilized double cleavage drilled compression tests and discovered that, the cured FGE had increased crack healing ability by nearly 100% recovery of fracture toughness.

Markus J. Barthel et al. [65] has demonstrated the use of well-defined PFGE-polyfurfuryl glycidyl ether homopolymers and PEO-b-PFGE-poly(ethylene oxide)-b-poly(furfuryl glycidyl ether) block copolymers as self-healing materials through anionic polymerization. They have created thermo-reversible network through retro-Diels-Alder chemistry between the furan groups on the side chains of the PFGE elements and a bi - functional bismaleimide cross linker in drop-cast polymer films. The developed network mended complex scratches and also exhibited multiple times healing capability. In a solvent-free synthesis proposed by Jeannette Hilf et al. [66], well-defined P((FGE-co-GME)C)-poly((furfuryl glycidyl ether)-co-(glycidyl methyl ether) carbonate) copolymers with varying FGE-furfuryl glycidyl ether composition in the range of 26% -100% are produced directly from CO_2 and the corresponding epoxide. The amorphous nature of the polymers is reflected in their thermal characteristics. Diels-Alder chemistry is used to do post-functionalization and cross-linking, which results in the production of reversible networks. At 110 °C, it is demonstrated that this change is thermally reversible. The first random terpolymerization and copolymerization of FGE-furfuryl glycidyl ether with EO-ethylene oxide and ECH-epichlorohydrin were accomplished by Ming Deng et al. [67] using an alkylaluminium catalyst system called i-Bu3Al/H3PO4/1,8-diazabicyclo[5.4.0]undec-7-ene (DBU). In comparison to conventional vulcanised polyepichlorohydrin elastomers, this DA cross-linked polyepichlorohydrin elastomers showed much improved mechanical properties, allowing them to be employed as structural materials without the need for reinforcement and also exhibited self-healing performance without inherent property damage.

2.3.3 Self-healing resin characterization and techniques

To assess the self-healing performance and investigate the healing through Diels-Alder bonding, FGE characterization techniques are essential. The most frequently used methods for characterizing the furfuryl glycidyl ether and the furan-maleimide based self-healing resin include, Fourier transform infrared spectroscopy (FTIR), nuclear magnetic resonance (^{1}H NMR,^{13}C NMR), differential scanning calorimetry analysis (DSC), optical, and field emission scanning electron microscopy (OM, FE-SEM) to monitor self-healing functionality and structural changes before and after healing.

FTIR is a technique used to monitor the functional elements (chemical linkages) present in the FGE as well as self-healing resin. This method was primarily employed in hydrogels, autonomous corrosion systems, healing systems based on capsules, and intrinsic healing systems to evaluate the functionality of the healing process and chemical interactions. Tian et al. [64] carried out the chemical architecture analysis of synthesized FGE through FTIR and confirmed both oxirane and furan functional rings in FGE. FTIR was utilized to investigate the cycloaddition phenomenon in DA-rDA based reversible self-healing thermosets in the study reported by Araya-Hermosilla et al. [68]. In this investigation, the molar ratio of the furan and maleimide groups was changed to monitor the strength of the bond and, consequently, the development of the DA reaction. In a different investigation by Garcia et al., [69] FTIR was used to verify the hydrolysis of the silyl ester healing substance that was later included into a self-healing anticorrosive coating technique. The ability of silyl ester to function as a hydrophobic protective layer in self-mending coatings was demonstrated through the use of the FTIR technique.

The NMR method employs the nuclear magnetic resonance phenomenon to investigate at the products chemical composition, interactions between the thermally reversible covalent bonds, the status of chemical reactions, and the development of self-healing systems. Felipe Orozco et al. [70] created a furan-grafted polyketone and subjected it to isothermal treatments at 150 °C after crosslinking it with a common aromatic bismaleimide (1,10 -(methylenedi-4,1-phenylene)bismaleimide). By ^{1}H NMR, the changes in the chemical structure and thermo-mechanical characteristics were primarily investigated. Mohsen Zolghadr et al. [71] synthesized and characterized self-mending Diels-Alder polymer and the related semi-interpenetrated polymer structure (semi-IPNs). Differential scanning calorimetry (DSC) and sol-gel transitional tests were

used to demonstrate the thermo-reversibility through retro Diels-Alder (rDA) reaction. The DA poly adduct was successfully subjected to three further DSC cycles, confirming the repeatability of the DA/rDA connection and disconnection.

2.3.4 Self-healing epoxy composite temperature range

To create self-healing capabilities in the powder coating system, depending on a commercially produced OH-polyester resin and uretdione cross-linker Negin Farshchi et al. [72] proposed a single molecule that is generated via Diels-Alder and retro Diels-Alder reaction. The prepared sample exhibiting self-healing functionality at 120 ºC temperature around 30 min with acceptable surface features and roughness. POSS-Polyhedral oligomeric silsesquioxane and maleimide resin were employed by Xu et al. [73] to incorporate a DA adduct at the interface. The self-healing composites showed signs of mending of the cracks upon visual examination after being heated to 135 °C and naturally cooling to room temperature.

Qiao Tian et al. [74] created the sample mixture using DPMBMI and DGFA, stoichiometric DPMBMI was dissolved in DGFA at 90 °C for five minutes before being immediately cooled to room temperature. The mixture exhibited a DA response from 30 to 85 °C with an exothermal spike at 65 °C and the retro-DA reaction is represented as an endothermic spike at 110 °C to perform healing functionality. Using a bi-functional DA based epoxy resin, Eugenio Amendola et al. [75] created a hybrid epoxy resin with inherent self-healing capabilities. The created network, which is based on common DGEBA and DA epoxy, allows for simultaneous modification of chemical-physical properties and healing potential. At 90 ºC, the mixture of 2Ph2Epo-DGEBA (65:35) and DDM-Jeff500 (60:40) was reacted, and DSC was used to track the degree of curing. As per data, Tg reaches 88 ºC at the conclusion of crosslinking, and no additional residual reaction is seen during the initial heating scan. When doing a DSC scan at 123 ºC, a broad endothermic phenomenon related to the r-DA reaction is seen at higher temperatures. From the above findings, it was observed that by increasing the polymers temperature to that needed for the retro-DA reaction (more than 110 ºC), cracks can be repaired. The applied heat encourages partial polymer chain dissociation, which enhances the mobility of each individual chain. Fresh DA bonds develop when the liquid cools, and the polymer chains will re-cross-link throughout the structure.

2.4 Graphene nano platelets (GNP) and Multiwalled carbon nanotubes (MWCNT)

Graphene is made of single atom thick sheet of carbon atoms, these carbon atoms are sp^2 hybridized in structure and are typically synthesized from bulk graphite using bottom-up and top-down methods. Since it was first introduced in 2004 [76], graphene has drawn interest from the whole world of research. The graphene has exceptional electrical, mechanical, and thermal properties, particularly when it is exfoliated into a single layer. Its usage is restricted in a number of applications due to a lack of cost-effective production techniques and the difficulties involved in producing fully exfoliated graphene on a large scale. The graphene can be easily substituted out for a more affordable alternative material such graphite nano platelets (GNPs), which typically contain square-shaped platelets with nanometer scale thickness less than 200 nm and micrometer scale lateral dimensions. Through a simplified chemical process, the GNPs can be produced in large quantities from bulk graphite [77].

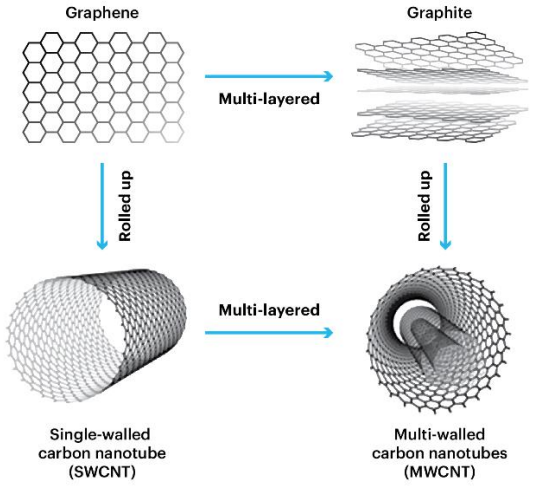

Figure 2.8 Graphene and carbon nanotube structure [78]

Similar to graphene, these nanotubes are created from carbon atoms arranged in a lattice just one atom thick, but they are formed into long, hollow tubes rather than a sheet. Multiwall Carbon Nanotubes (MWCNTs) are regarded of as a number of tubes stacked within of one another, similar to the rings of a tree or a folding telescopic antenna [78]. The majority of commercial uses in the past involved MWCNTs. Since the discovery of CNTs and graphene, the scientific community's interest in these two nanomaterials has expanded significantly, and there have been a significant number of papers on these materials.

2.4.1 Physical, chemical properties and applications of GNPs and MWCNTs

Graphene is chemically the most reactive form of carbon. Only form of carbon in which each single atom is in exposure of chemical reaction from two sides (due to the 2D structure). Carbon atom at the edge of graphene sheets have special chemical reactivity. Graphene is commonly modified with oxygen and nitrogen containing functional groups. While GNPs has a two-dimensional sheet nanostructure, CNTs have a one-dimensional cylindrical nanostructure. Both of these two nanomaterials are made of tightly packed honeycomb crystal lattices of sp^2 hybridized carbon atoms, but their geometric structures are very different. With Young's moduli of 0.27-0.95 TPa and 1 TPa, respectively, and ultimate strengths of 11-63 GPa and 130 Gpa, respectively [79], MWCNTs and GNPs were said to have superior mechanical properties. Additionally, MWCNTs and GNPs anticipated to perform remarkably in areas like thermal and electrical conductivity. Electrical and thermal conductivity for MWCNTs is up to 1800 S/cm and 3,000 W/mK respectively. Meanwhile, the electrical and thermal conductivity for GNPs is up to 6,000S/cm and 5,000 W/mK respectively [80]. It is anticipated that small concentrations of MWCNTs and GNPs can greatly enhance the performance of epoxy nanocomposites due to their exceptional thermal, mechanical, and electrical capabilities.

GNPs and MWCNTs have a wide range of existing and potential practical applications, where they are incorporated into materials to improve either existing qualities or to provide new functionality. These nanoparticles can be used as effective reinforcement in epoxy and CFRP based composite to improve electrical, thermal and mechanical characteristics. GNPs and MWCNTs can be used in the production of vehicles to increase the strength of components or to obtain the same strength with less material, thereby lowering weight. Examples include carbon-fiber bicycle components where the strength-to-weight ratio is enhanced by adding nanoparticles to the resin. Sports equipment like tennis racquets and golf clubs are also made with these nanomaterials. The resistance of silicon anodes for Li-ion batteries can be decreased and reinforced using MWCNTs, making them more resistant to the impacts of cracking during hundreds and thousands of discharge/charge cycles to promote new functionality [81].

2.4.2 Functionalization effect on GNPs and MWCNTs

The MWCNTs and GNPs based polymer nanocomposites have the potential to produce materials with outstanding mechanical properties and multifunctional features. However, due to the challenges involved in processing accumulated nanoparticles and the weak interfacial interactions between MWCNTs and GNPs and polymer, the potential for using reinforcements has been severely constrained. Effective reinforcements for polymer composites require excellent interfacial bonds between nanoparticles and the polymer matrix, which must be ensured by uniform dispersion [82]. By suitable chemical functionalizing nanoparticles, its inherent properties are maintained, and the accumulation of single-layer graphene following reduction in solvent phase is also avoided. The surfaces of GNPs and MWCNTs are highly oxygenated and contain functional groups including hydroxyl, ketone, diol, epoxide, and carboxyl that can significantly change the van der Waals interactions and cause a wide range of solubility in organic solvents and water [83]. The structural modification may occur on the surface, at the ends of the GNPs and MWCNTs, or both. In order to achieve surface functionalization, one or more sp^2 carbon atoms in the carbon network must be rehybridized into the sp^3 configuration while simultaneously losing their electronic conjugation [84]. The covalent modification of GNPs/MWCNTs can be achieved in four different ways: nucleophilic substitution, condensation, electrophilic addition, and addition [85]. M. Andrade-Guel et al. [86] treated graphene nano platelets with organic acids through under ultrasonic radiation of 350 W at various time periods 30 and 60 min. and achieved modified graphene surface with functional groups and as well as improved graphene dispersion.

Recent times, several salinization process have been implemented to modify MWCNTs for use in epoxy base composites with promising properties. Epoxy matrices reinforced with MWCNTs that have been functionalized with 3-aminopropyltriethoxysilane (APTES) have significantly improved thermo-mechanical characteristics. According to research by Lee et al., 0.2 wt.% APTES-modified MWCNTs enhanced an epoxy resins flexural modulus by 23% and Tg by 11.5 ^{o}C [87]. Lee and Rhee et al. [88] have demonstrated that APTES modified MWCNTs disperse more easily in epoxies and increase their wear resistance more than unmodified MWCNTs. Kim et al. [89] reported enhancement in tribological, thermo-mechanical properties for 3-glycidoxypropyltrimethoxysilane (GPTMS) functionalized nanotube reinforced epoxy composite and resulted in stronger interfacial adhesion between the matrix and nanotube.

2.5 Mechanical properties of pure and functionalized GNP and MWCNT reinforced composites

It is important to understand how the integration of covalent bond chemistry affects the pristine properties of the host polymer matrix and the composite in order to configure self-healing composites in real-time applications. The properties of the polymer matrix, such as its fracture toughness, stiffness, strength, elastic modulus, and glass transition temperatures need to be necessary to comprehend self-healing technology.

2.5.1 Polymer epoxy composite

In most of the self-healing composites, due to its structural features epoxy is chosen as the matrix material. The change in physical properties, such as the coefficient of thermal expansion, glass transition temperature, and viscoelastic properties, is often studied using a dynamic mechanical analyzer (DMA). The mechanical properties of epoxy composites with covalent bonding are investigated using tensile, flexural, impact, and mode I fracture tests.

Wudl et al. [54] made use of the thermally revertible covalent bonding capability of the DA/rDA adduct among furan (diene)/maleimide (dienophile) to produce a cross-linking structured polymer composite with self-mending capabilities. Xu et al. [90] integrated the DA adduct at the interface of bismaleimide resin and a POSS-furfurylamine functionalized polyhedral oligomeric silsesquioxane to create self-healing structure. The prepared self-healing nanocomposites showed signs of crack repair when heated to 135 °C and then naturally cooled to room temperature under visual inspection. Wang et al. [91] developed a novel approach for epoxy resin composite, reinforced with silane functionalized GNPs, and reported uniform dispersion along with an 82% improvement in fracture toughness and better mechanical properties. Lin et al. [92] produced a nanocomposite by combining the infusion of a maleimide-functionalized graphene oxide sheet with a polyurethane-based double crosslinked DA covalent group and reported 99% healing efficiency for the developed nanocomposite. Jang-Kyo Kim et al. [93] successfully functionalized silane MWCNT and fabricated MWCNT/epoxy nanocomposite and reported enhanced fracture resistance, thermal and mechanical properties compared to pristine sample. Alireza Yaghoubi et al. [94] reported a modified surface of hydroxylated multi-walled carbon nanotubes (OH-MWCNTs) using silanization with 3-aminopropyltriethoxysilane (APTS) and developed a rigid polyurethane (PU) foam nanocomposites. According to Ayatol Lahi et al., reinforcing 0.1, 0.5, and

1.0 weight percent of MWCNTs to epoxy, enhanced tensile strength of samples with the infusion of 0.1 and 0.5 wt. %. With 1.0 wt. % MWCNT, they came to the conclusion that agglomeration had taken place [95]. The investigations mentioned above show that the nanoparticle reinforcement frequencies were relatively low, these nanoparticles form agglomerations in the composite and cannot be disseminated uniformly. Shekar et al. [96] dispersed amine modified MWCNTs into the polymer composition evenly using a sonication technique. It was observed that, reinforcement with carbon nanotubes improved the flexural properties, namely flexural strength, flexural modulus, total flexural toughness and nonlinear deformation.

2.5.2 Fiber reinforced epoxy composite

The most popular FRP composites utilized in structural applications are CFRP and GFRP. The process of incorporating healing resin into the matrix material, the level of integration, and the bonding between the healing resin and matrix material all have an impact on the mechanical properties of the matrix material and, consequently, the mechanical performance of the overall composite. After analyzing the impact of acid and silane functionalization on the tensile and thermal properties of CNT-Basalt-epoxy nanocomposite, J.H. Lee and his coworkers [97] reported that the tensile strength and Young's modulus of silane-based CNT-Basalt-epoxy nanocomposite were significantly higher than those of unmodified nanocomposite. Park et al. [98] grafted maleimide group on to the carbon fiber surface, and the furan group functionalization was applied to the matrix. In comparison to a carbon fiber epoxy system, there has been a noticeable increase in interfacial shear strength was observed. A thermally stimulated DA interaction between maleimide and furan groups produced the healing effect. The healing process was initiated via electrical resistive heating. Kostopoulos et al. [99] prepared a carbon fibre reinforced composite using a self-healing epoxy system, and their findings indicate that although the DA-bond modified composite would have improved fatigue properties and fracture toughness, mode I interlaminar fracture toughness could still be recovered to 20-30% after healing the damaged specimens at 150 °C for 5 min with an applied pressure of about 1 kN and cooling at room temperature.

The ability of interface self-healing in epoxy: carbon composite materials has been achieved by W. Zhang et al. [100] through the utilization of thermo-reversible Diels-Alder (DA) bonds created between maleimide and furan groups to create an interphase between the surface of carbon fiber and an epoxy matrix. The single fiber micro-debonding test was used to assess the

interfacial shear strength (IFSS) and reported improved IFSS strength than un treated carbon fibers. Athanasios Kotrotsos et al. [101] integrated self-healing resin (Bismaleimide prepolymer, BMI pp) into high performance carbon fiber reinforced plastics (CFRPs) through Diels–Alder mechanism. Under mode I fracture loading, the impact of the (self-healing agent) SHA concentration on the toughening and healing capabilities of CFRPs was investigated. The SHA was able to moderately increase the composites interlaminar fracture toughness as well as its thermally activated healing capabilities. Flexural characteristics, flexural strength (σ_{max}) and flexural modulus (E_{flex}), both decrease as SHA concentration rises to 240 gsm.

2.6 Self-healing efficiency of pure and functionalized GNP and MWCNT reinforced composites

Self-healing assessment of the composite are typically evaluated on both a qualitative and quantitative terms. Different microscopes including optical, SEM, and confocal laser microscopes are frequently employed for qualitative evaluation. Quantitative healing performance is evaluated based on capacity of the sample to restore its original or virgin properties. The self-healing approach main objective in both evaluations is to repair the damage and extend the component service life by limiting crack propagation. Different material properties such as fracture toughness, stiffness and strength are used to measure the healing efficiency. For convenience, researchers defined healing efficiency as being common to any material property of interest

The virgin material properties, healing process, and desired failure mode may all influence the material property that must be chosen to define the healing efficiency. For instance, determining the healing efficiency based on the fracture toughness necessitates mode I fracture crack opening which is nearly identical to the micro crack growth phenomenon that manifests in real-time applications [102]. It is preferable to assess the elastomer healing efficiency using tear strength or strain energy. Restoration of impact or flexural properties after damage is a better criterion for assessing the efficiency of the healing process of fiber reinforced composites. Flexural and impact loadings cause delamination, micro-cracking, and fiber-matrix de-bonding failure damages, therefore it is ideal to assess the healing efficiency of fiber reinforced polymer composites based on the recovery of those damages.

2.6.1 Self-healing of polymer epoxy composite

Researchers are focusing on epoxy resin-based polymer composites to create thermosetting polymer-based self-healing composites. Cracks can emerge anywhere in the structure as a result of various loading scenarios and types of application. Based on the type of damage recovery, several approaches for evaluating the healing effectiveness of epoxy composites have been developed. Damage in epoxy composites frequently involves some sort of fracture, in order to have structural applications, it is required to analyze the self-healing capacity of the composite based on the fracture toughness recovery.

2.6.1.1 Healing performance based on fracture toughness recovery

On the basis of the fracture toughness recovery, quasi-static fracture tests are frequently used to create self-healing systems. The fracture toughness can be measured using a variety of mechanical techniques, including CT- compact tension, DCB- double cantilever beam, TDCB- tapered double cantilever beam, WTDCB- width tapered double cantilever beam, SENB- single edge notch bending, DCDC- double cleavage drilled compression, three-point bending, and four- point bending. However, due to controlled and anticipated crack propagation, DCB and TDCB are the most often used techniques to assess mode I fracture toughness. Additionally, with these geometries smaller damage volumes can be created and all the fracture parameters can be measured. The type of geometry used and the loads applied during testing often affect the damage volume. The TDCB geometry suggested by White et al. [1] can be used to precisely model the micro cracking that takes place in real-time applications. The TDCB geometry also provides the ability to quantify fracture toughness independent of crack length in addition to crack progression along the specimen centerline. It is challenging to estimate the length of repaired sample cracks in the majority of investigations, researchers used TDCB geometry to assess the healing performance.

The self-healing efficiency for mode I quasistatic fracture testing is defined as the ratio of healed to virgin sample fracture toughness as the fracture resistance of the damaged state approaches zero.

$$\eta = \frac{K_{IC}healed}{K_{IC}Virgin} = \frac{P_C healed}{P_C Virgin} \qquad \text{Equation 2.1}$$

$$K_{IC} = 2P_C \frac{\sqrt{m}}{\beta}$$ Equation 2.2

$$K_{IC} = 11.2 \times 10^{-3} P_C \quad MPam^{1/2}$$ Equation 2.3

Where K_{IC} (virgin) and K_{IC} (healed) are the fracture toughness of virgin and healed samples respectively and P_C - Critical failure load.

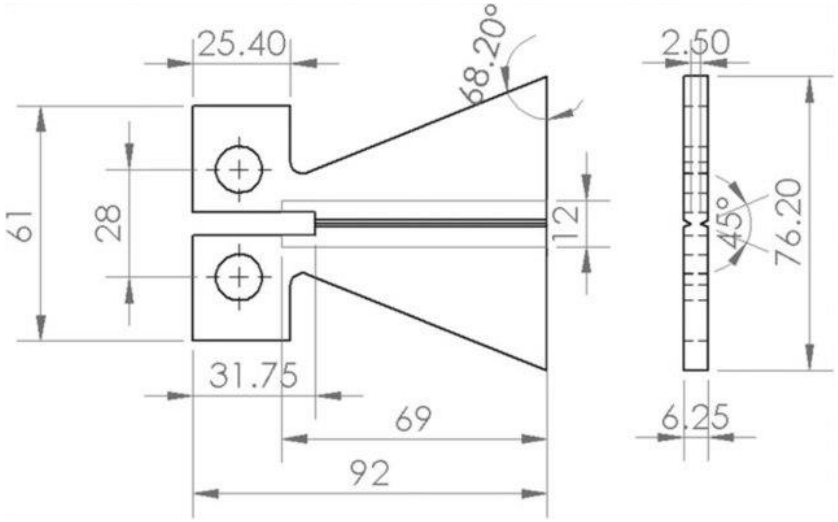

Figure 2.9 Double Tapered Cantilever Beam (TDCB) geometry [1]

Through the use of a DCPD/Grubbs' healing system, Kirkby et al. [103] examined the impact of minimizing crack separation by activating embedded shape memory alloy (SMA) wires to seal the crack in epoxy fracture samples. For manually injected samples, the localized heating of the crack plane caused by the activation of the SMA wire resulted in a combination of reduced crack gap and fracture toughness recovery that boosted healing efficiency by a factor of 1.6. In order to study fracture toughness, Shelesh-Nezhad et al. [104] used TDCB- taper double cantilever beam geometry with nanofiller infusion. They reported a 165% and 59% increase in fracture energy, and fracture toughness respectively. As a substitute to TDCB geometry, Jin et al. [105] used WTDCB geometry (which further provides crack growth independent fracture toughness assessment), to analyze the healing effectiveness of steel adherents coupled self-healing epoxy adhesive system utilizing quasi static fracture test. They reported recovering 56% of the initial fracture toughness after 24 hours of healing at room temperature.

2.6.2 Self-healing fiber reinforced epoxy composite

Composite materials perform differently under various thermomechanical loadings since they are composed of several components. But for use as structural materials, maintaining structural integrity is crucial. In self-healing systems, the component structural integrity can be preserved by regaining their original or virgin mechanical properties. As a result, it is crucial to gauge the effectiveness of self-healing based on the recovery of mechanical properties. The efficiency of the healing process is assessed using factors including fracture toughness, ultimate tensile strength, impact strength, fatigue resistance, and compressive and bending strength.

2.6.2.1 Healing performance based on mode I damage assessment

Numerous fabrication techniques, such as vacuum bagging, hand lay-up, and vacuum-aided resin infusion, have been used to fabricate fiber-reinforced self-repairing epoxy composites. Due to ease of manufacturing, customizable mold sizes and shapes, simple up- or down-scaling, and higher strength rating of composite, the vacuum bagging method is most frequently employed. Laminates of epoxy/carbon fiber composites with various proportions of CNT and sizing agent were produced using a hand lay-up assisted vacuum bagging process and reported a 20 % improvement in Young's modulus [106].

The effect of GNPs on the mechanical characteristics, microstructure, and electrical conductivity of cu-based carbon fiber reinforced composites has been studied by Zeng et al. [107]. According to the research findings, reinforcing nanoparticles significantly improved the composite hardness and tensile strength, even if the increased nanoparticles content initially reduced the composite ultimate tensile strength. After analyzing the impact of acid and silane functionalization on the tensile and thermal properties of CNT-Basalt-epoxy nanocomposite, J.H. Lee and his coworkers [97] reported that the tensile strength and Young's modulus of silane-based CNT-Basalt-epoxy nanocomposite were significantly higher than those of unmodified nanocomposite. In order to repair the matrix micro-cracks, Shabani et al. [108] infused intrinsic self-mending resin in the epoxy/glass fiber cross-ply composite. Flexural loading was used to generate the initial damages, and the recovery in flexural modulus and strength was used to assess the efficiency of the composite. Peterson et al. [109] have focused on the incorporation of thermally reversible Diels-Alder adduct into the glass fiber-reinforced epoxy composite by incorporating furan on the

thermosetting epoxy resin and maleimide on the glass fiber surface. The micro droplet debonding test was used to determine the efficiency of the healing process. Some specimens exhibited a maximum healing efficiency of 100%, and up to five times healing was successfully demonstrated.

2.6.2.2 Healing performance based on other mechanical property recovery

In a few investigations, the criteria utilized to assess the self-healing capability of fibre reinforced epoxy composites include, recovery in compressive strength, ultimate tensile strength, and flexural strength, interlaminar shear strength (ILSS) after impact. Pan Wu et al. [110] prepared Diels-Alder (DA) thermo-reversible compound consisting of a bismaleimide (DPBMI) and a furan (FA) group, followed by grafted to a low-viscosity epoxy resin to prepare a self-healing epoxy matrix system. The synthesized self-healing epoxy system was incorporated in a unidirectional fiberglass cloth and prepare a structural FRP with excellent self-healing efficiency. The ILSS was used to measure the self-healing efficiency and reported 108.5 % healing efficiency for the first time healing. W. Post et al. [111] reported the fabrication of an organic-inorganic thermoset matrix-based intrinsically healing glass fibre reinforced polymer (GFRP) composite. The newly designed matrix has been demonstrated by thermomechanical testing to have a Young's modulus value in the region of (800-1200 MPa), the capacity to withstand thermally induced healing delamination (70-85 °C). After that, GFRPs were created, and standard flexural, fracture, and low-velocity impact testing was used to assess their various healing capacities below 100 °C. It was discovered that only a modest amount of pressure is necessary for the repair of small scale ($<cm^2$) sized damage. Whereas, for larger scale damage ($>cm^2$) necessitates additional healing pressure to completely align the broken surfaces and put the fracture regions back in touch.

2.7 Research gaps and Objectives

After conducting a thorough literature survey on the past available research pertaining to self-healing of epoxy based fibre reinforced polymer composites, the following gaps were identified.

- Limited literature reported on the synthesis of thermally reversible self-healing composites and their self-healing assessment through TDCB model.
- Most of the self-healing applications are limited to anticorrosion coatings and less focus had been done on the structural integrity of components using self-healing approach.
- Not many researchers focused on controlling of unwanted irreversible site reactions encountered in DA chemistry which in-turn downgrades the healing efficiency.
- Maintaining a perfect balance between reversible bonds (responsible for healing) and irreversible bonds (responsible to retain strength) in the epoxy matrix was very less exposed.
- Limited work available on the effect of nanoparticle infused epoxy composites mechanical, self-healing performance.
- Solution to nanofiller agglomeration and the bulk thermo-reversible matrix healing was hardly found.
- Preparation of bismaleimide grafted nanofillers which have both strength and interfacial healing capability were not found.
- Very few studies reported the self-healing of CFRP composites and there is a need to crosscheck the reliability of the results.
- No literature was found on the damping characterization of self-healing CFRP composites and the self-healing efficiency evaluation through stiffness regain.

In order to address above mentioned research gaps, the following objectives are outlined for the current research work.

1. Synthesis and characterization of furan (FGE) and maleimide (DPBMI) based thermally reversible self- healing polymer composite through Diels-Alder bonding
2. Evaluation of the exfoliation level effect of oxidation, silane functionalization followed by bismaleimide grafting on graphene nano platelets (GNPs) / Multiwalled carbon nanotubes (MWCNTs) as reinforcement in composite

3. Integration of optimized self-healing matrix with functionalized MWCNT (at various exfoliation levels) infusion in CFRP composites and evaluating the impact of filler content on mechanical performance
4. Self-healing performance evaluation and damping characterization of functionalized MWCNT reinforced carbon fibre epoxy composites and healing efficiency assessment through flexural and IET technique

Integration of above objectives towards the main aim of the research can be seen in Figure 2.10. The main objective of this work is to investigate matrix/fiber/nanofillers interface junction healing properties of the CFRP composite before and after damage through Diels-Alder bonding. Furthermore, it is intended to re-form structural stability over the CFRP interface junction of the damaged area and also examine the average healing efficiency. After consecutive damage cycle over the same region, the amount of strength recovery for each damage cycle were also investigated.

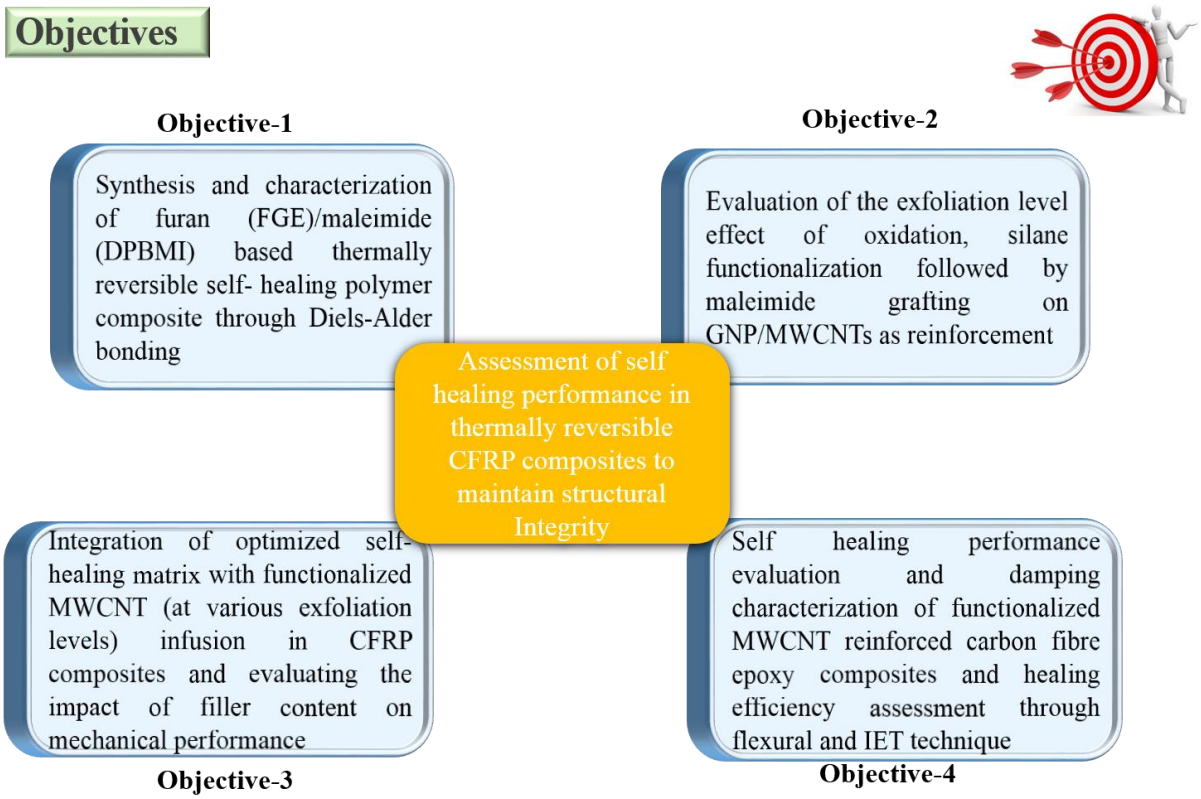

Figure 2.10 Integration of the objectives

2.8 Work plan

The following work plan is followed to accomplish the main objective of the research.

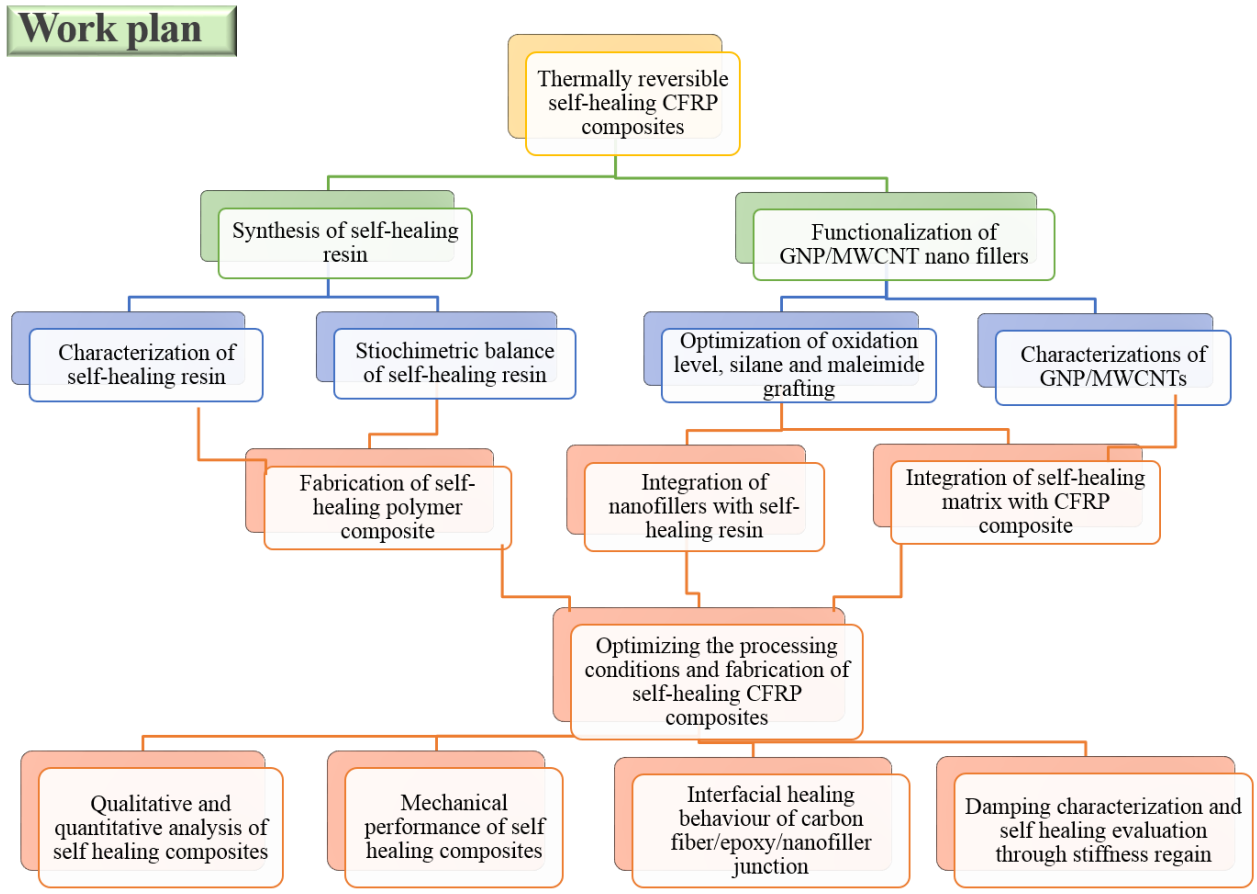

Figure 2.11 Work plan

Chapter 3

Synthesis and characterization of furan-maleimide based self-healing polymer composite

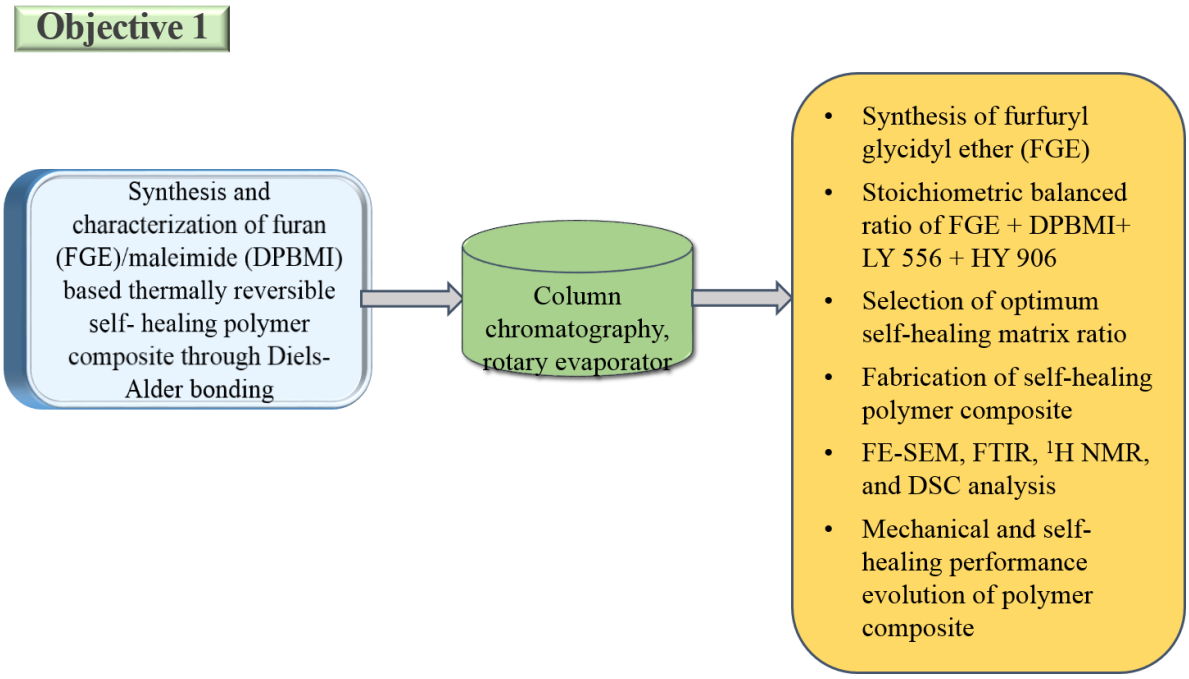

This chapter deals with the materials and synthesis procedures involved in the development of thermally reversible self-healing resin and discusses the effect of different stoichiometric ratios of resin by varying epoxy wt.%. The characterization techniques used to analyze the developed polymer composite have been presented. A brief discussion on the characterization procedures and the equations used to find different properties have been discussed.

3.1 Introduction

The primary objectives of self-healing materials are to provide autonomous repair of invisible micro-cracks, increased component service life, and increased structure reliability and durability. While various strategies were examined, one of the most successful and versatile method to achieve self-healing is diene-deinophile based Diels-Alder (DA) cycloaddition, which is fully reversible and undergoes subsequent rDA and DA reactions under stimulus conditions. The DA reaction is a reversible cycloaddition reaction between diene and dienophile, and the adduct is reversible at temperatures above 110 ^{o}C. Generally, a furfuryl group is used as the diene, whereas a maleimide group is used as the dienophile. Healing of cracks can be achieved by heating the polymer above the temperature required for a reversible-DA (rDA) reaction.

In the event of crack, under stimulus conditions, the inter-monomer cross-linking structure (the combined diene and dienophile network) can be separated known as r-DA reaction and upon cooling the separated crosslinking structure will be reunited and that's how the crack will be mended. This process is fully reversible and can be used to restore a fractured part of the polymer multiple times, and it does not require additional ingredients such as catalyst, additional monomer or special surface treatment of the fractured interface. Epoxy resin and amine based hardener are well known for their better flowability, room temperature curing ability, better adhesion features, good compatibility, and rapid solidification. Hence, in the present work, the stoichiometric ratios of synthesized furan-maleimide group: epoxy-hardener group; were used former responsible to develop healing functionalities and later responsible to retain the strength of the polymer composite. Whenever, the crack generated the DA adduct formed throughout the polymer crosslinking network will be separated as diene, dienophile and upon cooling mobility of each polymer chain will be improved by forming DA adduct again.

3.2 Materials and Methods

Different materials used in the synthesis of furfuryl glycidyl ether (FGE) and stoichiometric self-healing preparation procedures of FGE, bismaleimide, epoxy resin and hardener are discussed in this section.

3.2.1 Materials

Epichlorohydrin, tetrabutylammonium hydrogensulfate, and furfuryl alcohol were used to synthesize furfuryl glycidyl ether (diene), Silica gel (150 mesh size) and obtained from Sisco Laboratory, India. 4,4-bismaleimide diphenylmethane (BMI/DPBMI) were used as dienophile and received from Alfa Aesar, India. Tetrafunctional methylhexahydrophthalic anhydride curing hardener (MHHPA-HY906) and Diglycidylether of bisphenol-A based epoxy resin (DGEBA-LY556) were used to fabricate host polymer matrix and obtained from Huntsman, India. Analytical grade reagents diethyl ether, hexane, ethyl acetate, were used without any additional purification, obtained from Finar chemicals Ltd., India, and NaOH (50 w/v.%) obtained from Merck & Co., DI (Deionized) water was used throughout the synthesis. Table 3.1 specifies the list of materials used in the current study and Table 3.2 specifies the materials key data specifications obtained from standard data sheets. Figure 3.1 shows the chemical architecture of the materials used in the current study.

Table 3.1 List of materials used in the present study

Material	Purpose	Purchased from	Remarks
Epichlorohydrin	Hydroxyl group in DA adduct	Sisco Laboratory, India	Oxiarane
Tetrabutylammonium hydrogensulfate	Ring opening reaction	Sisco Laboratory, India	Sulfate
Furfuryl alcohol	Oxirane group in DA adduct	Sisco Laboratory, India	Hydroxyl
DPBMI	Dienophile in DA adduct	Alfa Aesar, India	Oligomers
DGEBA basedepoxy resin	Host polymer matrix material	Huntsman, india	Araldite® LY556 (Trade name)
MHHPA hardener	Curing agent	Huntsman, india	Aradur® HY06 (Trade name)

Diethyl ether1, hexane, ethyl acetate	Solvents	Finar chemicals Ltd., Mumbai, India	AR grade
NaOH	Ring closing of DA adduct	Merck & Co.	AR grade

Table 3.2 Key data specifications of materials used in synthesis

Material	Visual appearance	Density (g/cc)	Viscosity (pa.s) at 25 ºC	Storage life (in years)
Epichlorohydrin	clear, liquid	1.18		1
Tetrabutylammonium hydrogensulfate	solid	--	1.01	1
Furfuryl alcohol	clear, liquid	1.13	--	1
DPBMI	solid, spherical moieties	1.2-1.25	--	2
DGEBA basedepoxy resin	clear, viscous liquid	1.15 – 1.20	10 – 12	3
MHHPA hardener	clear, liquid	1.162	53.0	1

Material	Chemical Structure
Epichlorohydrin	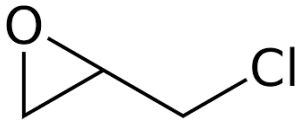
Tetrabutylammonium hydrogensulfate	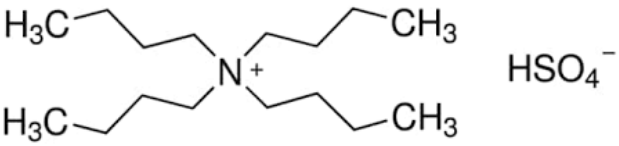
Furfuryl alcohol	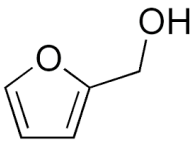
DPBMI	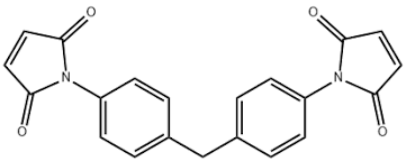

DGEBA based epoxy resin

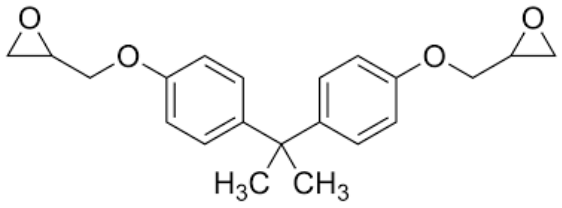

MHHPA hardener

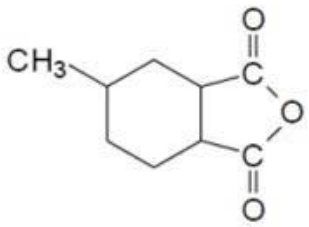

Figure 3.1 Representative chemical structures of materials used in the study

3.2.2 Synthesis of furfuryl glycidyl ether (FGE)

FGE synthesis involved a two-step approach proposed by Tian et al. [64]. In a three necked round bottom flask equipped with inlet charging, thermometer, and Nitrogen flow, 76 g (0.82 mol) epichlorohydrin was mixed with 3 g tetra-butylammonium hydrogen sulfate under magnetic stirring. Then, 72 g of furfuryl alcohol was added dropwise by maintaining a 1:1.1 molar ratio of epichlorohydrin and furfuryl alcohol followed by 6 h stirring. Tetra-butylammonium hydrogen sulfate assists in the synthesis of chlorohydrin ether by beginning the ring opening reaction between epichlorohydrin oxirane and furfuryl alcohol hydroxyl groups. The chlorohydrin ether ring closure reaction was carried by adding 120 ml NaOH (50 w/v % diluted solution) followed by 3 h of stirring.

The obtained solution was blended with 120 ml of diethyl ether (prevents subsequent ring opening reaction of oxirane and hydroxyl group) and 120 ml of DI water using a separating funnel, resulting in organic phase layer separation. For column chromatography, a 150 mesh silica gel containing 9 ml ethyl acetate and 100 ml hexane was employed as the stationary phase and mobile phase respectively, to extract purified FGE. Thin-layer chromatography was used to determine the purity of the resulting solvent, which was collected in test tubes. Finally, to extract the purest FGE solvent possible, a rotary evaporator was used.

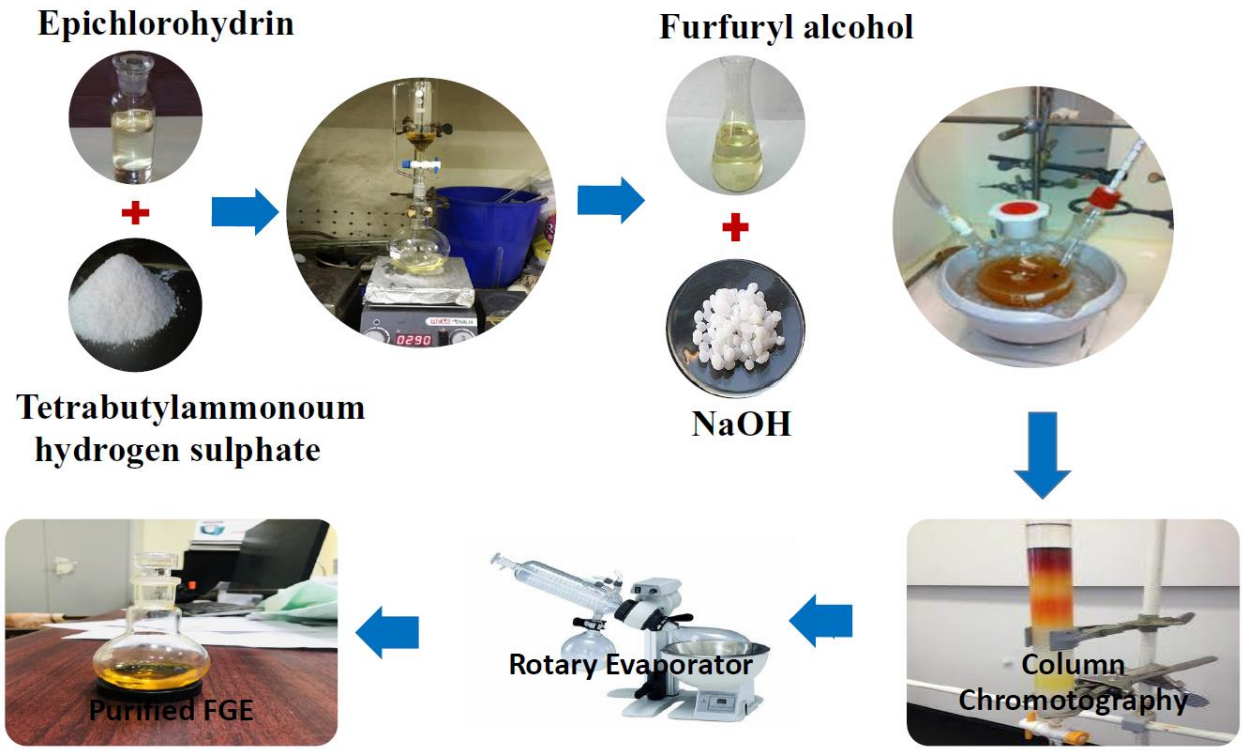

Figure 3.2 Synthesis process of furfuryl glycidyl ether (FGE)

3.2.3 Thermally Reversible Self-healing resin preparation

The thermally reversible self-healing resin matrix was created by compounding irreversible and reversible matrix at their stoichiometric ratios, with (DGEBA+ MHHPA) resin as the irreversible system and (FGE + DPBMI) compound as the reversible system.

Under magnetic stirring, 12g (0.027 mol) of DPBMI was dissolved in 10.3 g of (0.054 mol) of FGE in an oil bath at 90 ^{o}C for 5 minutes at 2:1 molar ratio. Using mechanical agitator, the resultant was mixed with 10.01 g of DGEBA epoxy resin (35 wt. % DGEBA in the combined weight of DGEBA, FGE, and DPBMI) and cured with MHHPA anhydride hardener. The molar ratios of FGE: MHHPA and DGEBA: MHHPA are maintained as 1:0.8 and 1:2 respectively. The DA based epoxy mixture was subjected to high speed mechanical stirrer for 15 min. The resultant was degassed for 40-50 minutes in a vacuumed desiccator to remove any trapped air. The developed compound was surged into a silicon mould and cured using autoclave at 85 ^{o}C / 8 h, 130 ^{o}C / 8 h, and 85 ^{o}C / 8 h. The cured polymer composite was coded as 35DA. Using a similar

approach, by fixing FGE and BMI quantities, and varying DGEBA wt. %. 45DA and 55DA were prepared.

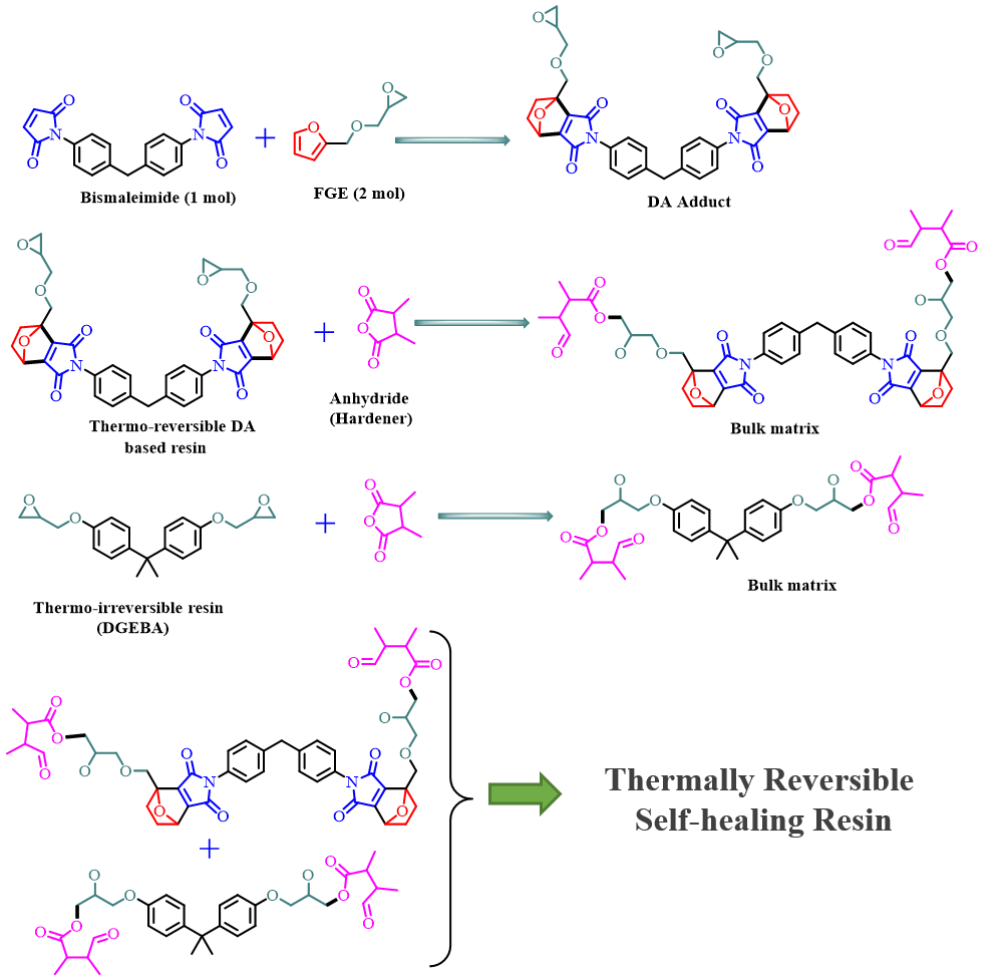

Figure 3.3. Schematic representation of thermally reversible self-healing composite preparation

3.3 Characterization of Self-healing resin

Various characterization techniques used to investigate the chemical structure of the synthesized FGE were discussed in this section.

3.3.1 Molecular architecture analysis

Using a Bruker Alpha II Fourier transform Infrared spectrometer (FTIR) with a wavenumber range of 4000 cm^{-1} to 400 cm^{-1} and a resolution of 2 cm^{-1}, the molecular architecture and functional

groups present in the synthesized FGE and thermally reversible self-healing resin. The synthesized FGE and thermally reversible self-healing resin were blended with potassium bromide (Kbr). The FTIR spectra was observed in the transmittance mode.

To cross-check the precise functional groups, present in the FGE, Bruker Avance III HD 400 Nuclear magnetic resonance spectrometer (NMR) was used. Deuterated chloroform (CDCl3) was utilized as the solvent for the ^{1}H NMR spin echo technique for sample, and tetramethyl silane (TMS) was employed as the reference material. For complete solubility of FGE in CDCl3, the mix was rotated for 20 min and filtered. For the study, the soluble fraction was taken into consideration. To know the information of the backbone of the FGE molecules, ^{13}C NMR was performed with the chemical shift range from 150 ppm to 40 ppm.

3.3.2 Differential Scanning Calorimetry (DSC) analysis

The differential scanning calorimetry is an instrument used for thermal analysis, measures change in physical characteristics of a sample along with temperature over time. DSC measures a heat quantity that is excessively radiated or absorbed by the sample during a temperature shift based on the difference in temperature between the sample and the reference material.

The DSC analysis was performed on thermally reversible self-healing resin to evaluate the impact of hybridization on the production of Diels-Alder (DA) bonds and retro-Diels-Alder (r-DA) bonds, The heat flow change that occurred during curing of the resin in its liquid form were examined with TG-DSC to determine the curing behavior.

In the present study, the healing properties of prepared thermally reversible self-healing resin were examined using a DSC- differential scanning calorimeter analyzer (DSC 8000 system, PerkinElmer). The experiment was carried at 10 °C/min heating rate from room temperature to 800 ^{o}C in nitrogen environment.

3.3.3 Mechanical characterization of self-healing polymer composite

Tensile tests were carried out using an Advance Equipments (AE) 30kN universal testing machine (UTM) at a crosshead speed of 1 mm/min and a 5 kN load cell to examine the mechanical behaviour of thermally reversible self-healing epoxy composites. Type v ASTM D-638 (l× w× t is 60×12.5×3.2 mm respectively) sample was used to assess the structural integrity of self-healing

polymer composites. Three identical samples were examined for each result, and the average was taken into account for reporting.

3.3.4 FE-SEM fracture morphology of tensile sample

FE-SEM uses high energy electrons to scan the surface of the specimen and the interaction of the electrons with the specimen's atoms results in a variety of signals. Respective detectors pick up these signals and generate scan images that contain details about the surface composition and morphology.

Surface morphology of the fracture samples is one of the important aspects to be investigated to achieve better self-healing performance. In this study (JSM-7600F FEG-SEM) field emission scanning gun electron microscope at 5 kv acceleration voltage was used. Before testing, samples were attached to conductive carbon tape and gold sputtering to avoid charging of the samples during experimentation and to get better image resolution.

3.4 Results and Discussions

This section deals with chemical structure confirmation of synthesized FGE, the optimized stoichiometric ratio of thermally reversible self-healing resin to balance healing characteristics and mechanical strength.

3.4.1 Chemical architecture of furfuryl glycidyl ether

To verify the molecular structure and functional groups present in the synthesized furufuryl glycidyl ether (FGE), FTIR, ^{1}NMR and ^{13}C NMR analysis are used. Both of these techniques verifies the DA adduct formation possibilities of FGE with DPBMI by examining the functional groups present in the FGE.

3.4.1.1 FTIR analysis of furfuryl glycidyl ether

Epichlorohydrin and furfuryl alcohol were used to synthesize FGE, the chemical architecture was determined by FTIR, and the spectra data was represented by Figure 3.4 The absorption spikes at 3148 cm^{-1}, and 3114 cm^{-1} represent the C-H broadening vibration of the furan ring, the characteristic spike at 1504 cm^{-1} represents the C-C broadening vibration of the furan ring, the

peaks at 1105 cm^{-1}, 1019 cm^{-1}, and 752 cm^{-1} corresponds to C-O stretching vibration [112] of furan ring, furan breathing, and mono-substituted furan ring, respectively.

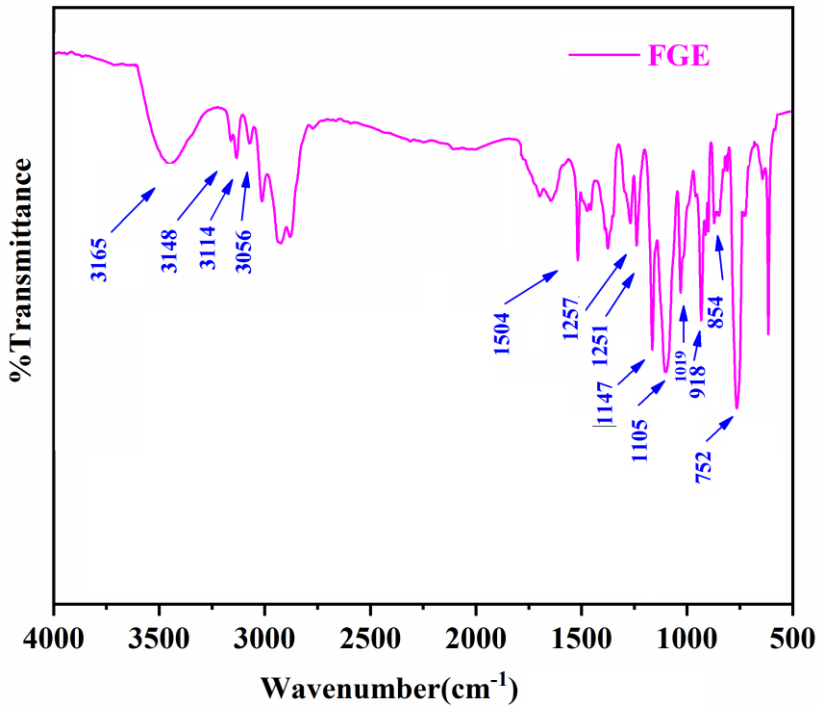

Figure 3.3 FTIR spectra analysis of synthesized furfuryl glycidyl ether

The characteristic intensity spike at 3056 cm^{-1} represents the C-H vibration stretching of the oxirane ring, and the intensity peaks identified at 1257 cm^{-1}, 1252 cm^{-1}, and 854 cm^{-1} represents C-O-C stretching vibration of oxirane group and 916 cm^{-1} peak corresponds to oxirane ring breathing of FGE. The characteristic peak at 3465 cm^{-1} attributed to O-H stretching of FGE. The FTIR data demonstrated that the FGE product has both oxirane and furan rings, which corresponds to the chemical structure of the target substance FGE.

Table 3.3 Functional groups present in the furfuryl glycidyl ether

Wavenumber (cm^{-1})	Peak	Intensity
3465	O-H stretching of FGE	strong
3148, 3114	C-H broadening vibration of the furan ring	medium
1504	C-C broadening vibration of the furan ring	medium
1105	C-O stretching vibrations of furan ring	strong
1019	C-O stretching vibrations of furan breathing	medium

752	C-O stretching vibrations of mono substituted furan ring	strong
3056	C-H vibration stretching of the oxirane ring	medium
1257, 1252, 854	C-O-C stretching vibration of oxirane group	medium
918	oxirane ring breathing of FGE	strong

3.4.1.2 ^{1}H NMR and ^{13}C NMR analysis of furfuryl glycidyl ether

The product's ^{1}H NMR spectra were studied for confirmation of both oxirane and furan rings existence in FGE Figure (3.5 a). The characterization data of ^{1}H NMR of FGE shown in Figure 3.5 (a) is as follows: the two dd peaks at δ 2.49 and 2.67 ppm represent CH_2 protons of oxirane moiety. The oxirane CH proton appears as a multiplet from δ 3.02-3.06 ppm. The CH2 protons linked to oxirane are represented by the twin dd spikes at δ 3.32 and 3.65 ppm, respectively. Between δ 4.37 and 4.46 ppm, the CH_2 protons linked to the furan ring showed as two doublets. The furan protons appeared in the aromatic region [74]. As a result, the feasibility of oxirane and furan rings has been established by synthesized FGE.

The characterization spikes of ^{13}C nuclear magnetic resonance of FGE are as follows, Figure (3.5 b). The peaks at δ 151, 142, 110, and 109 ppm represent the carbons present in the furan ring [113]. The peaks at δ 70 and 64 ppm correspond to the two CH_2 carbons attached to the furan ring and oxirane ring, respectively. The peak at δ 50 ppm is respective to the CH carbon of the oxirane ring, and the peak at δ 44 ppm belongs to the CH_2 carbon of the oxirane ring.

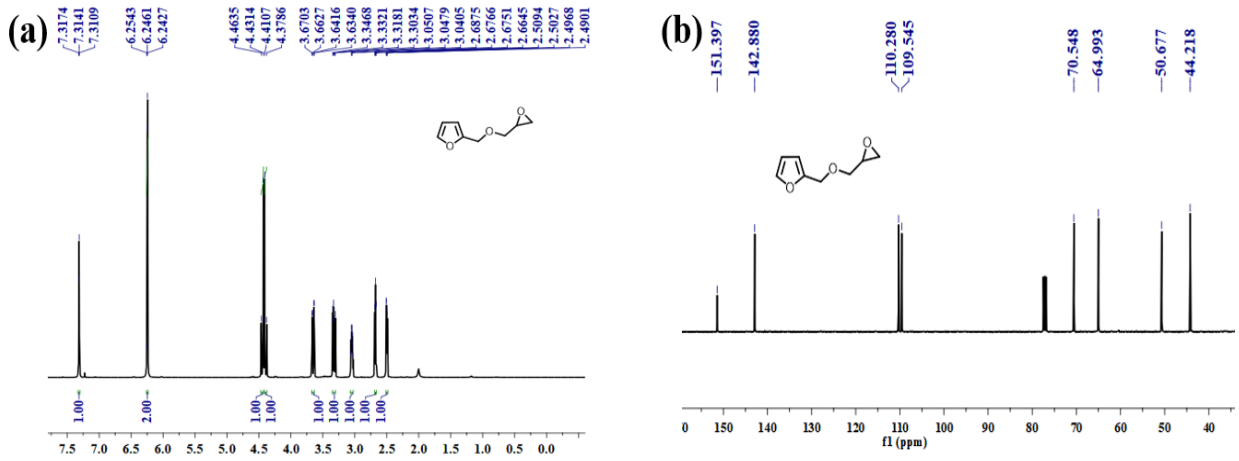

Figure 3.5 (a) ^{1}H NMR and (b) ^{13}C NMR of furfuryl glycidyl ether

Table 3.4 Functional groups and type of proton present in the furfuryl glycidyl ether

Approximate chemical shift (ppm)	Type of proton
2.49-2.67	CH_2 protons of oxirane moiety.
3.02-3.06	CH proton of oxirane
3.32 -3.65	CH_2 protons attached to oxirane
4.37-4.46	CH_2 protons attached to furan ring
51, 142, 110 and 109	Carbons present in furan ring
70 and 64	Two CH_2 carbons attached to furan ring and oxirane ring
44	CH_2 carbon of oxirane ring
50	CH carbon of oxirane ring

3.4.1.3 DSC analysis of thermally reversible self-healing resin

The temperature ranges of furan and maleimide DA self-healing resin thermally remendable properties were revealed by the DSC heating experiment Figure 3.6. The stoichiometric sample mixture of FGE/malemide/epoxy was heated in a DSC pan; the mixture executed DA reaction at an exothermic spike of 85 ^oC and retro DA reaction at an endothermic spike of 130 ^oC.

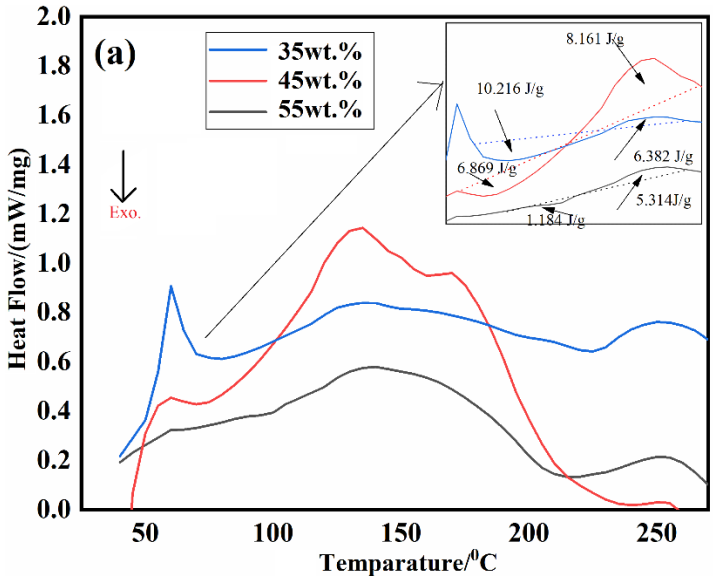

Figure 3.5 DSC analysis of thermally reversible self-healing resin

Further, the furan/epoxide ring opening and glycidyl ether degradation were identified at an exothermic trace of 172 ^{o}C and 250 ^{o}C, respectively. The area below the curve corresponding to that peak determines how much energy is absorbed during the separation of the DA adduct [54]. As the epoxy percentage rises from 35 to 55 wt.%, the exothermic and endothermic trace area reduces, resulting in lesser DA bonds formation and increased irreversibility. The specific enthalpy at 130 ^{o}C (area of endothermic peak) was reported as 6.382 J/g and 8.161 J/g for 35 and 45 wt.%, respectively, and the specific enthalpy reduced to 5.31 J/g for 55 wt.% attributed to lesser retro DA bond formations which in turn reduces the healing efficiency. Based on the DSC data, 45 wt.% resin has higher number of DA and rDA bonds and exhibited maximum specific enthalpy.

3.4.1.4 FTIR analysis of thermally reversible self-healing resin

Characteristic peak (cm^{-1})	Type of proton
3480	OH-hydroxyl groups identified as a broad absorption appearance due to etherification process between epoxide and FGE.
1707-1777	DA adduct peak and is responsible for the production of succinimide rings due to maleimide involvement with the furan group in DA cycloaddition
747	C-H bond out-plane stretching of mono-substituted furan group
1120-972	furan ring breathing, signifying the successful incorporation of the furan group into the epoxide structure
1452-1144	Maleimide moiety C-N-C band

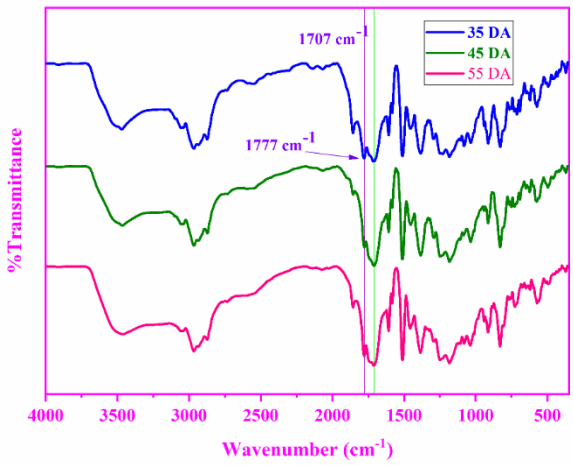

Figure 3.7 (a) Peak and respective proton description (b) FTIR spectra data of furan maleimide (DA) based self-healing resin

The FTIR spectra of polymer composite were carried out to investigate the association of maleimide in polymer epoxy resin matrix. Figure 3.7 (b) shows the FTIR spectra of Furan-maleimide Diels-Alder (FMDA) polymer samples of 35DA, 45DA and 55DA. It is clearly seen that a new characteristic peak was observed at 1777 cm^{-1} near 1707 cm^{-1} (C=O) stretching peak [114]. The relative height of the C-O stretching correlates to the number of DA covalent bond formation between furan and maleimide groups, as shown in the spectra. DGEBA epoxy resin content increase leads to a decrease in the intensity of the characteristic peak from 35DA to 55DA.

3.4.1.5 Tensile characteristics of self-healing polymer composite

The tensile strength, percent strain, and elastic modulus of self-mending polymer composites were evaluated under a 5 kN load cell at 1 mm/min cross speed, via Type-v ASTM (D 638). Tensile strength, percent of strain, and modulus of elasticity graphs are illustrated in Figure 3.8 (a,b,c) respectively.

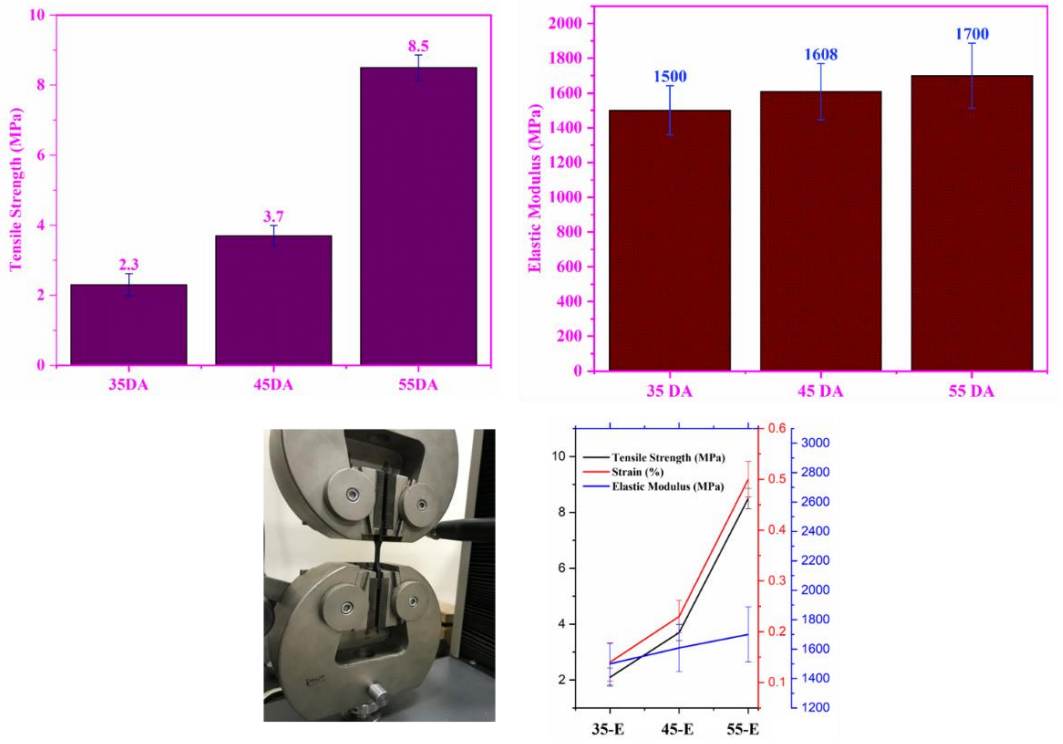

Figure 3.8 (a) Tensile strength (b) Elastic modulus (c) Sample loading of self-healing polymer composite

35DA exhibited a tensile strength of 2.1 MPa, strain of 0.14 percent and modulus of 1500 MPa respectively. For 45DA, the tensile strength, strain and modulus were 3.7 MPa, 0.23 percent and 1608 MPa respectively, which increased to 8.5 MPa, 0.5 percent and 1700 MPa for 55FMDA. The higher values of 45DA and 55DA are attributable to an raise in epoxy weight percentage, which enhances the cross linkages consisting of stable anhydride-epoxy bonds and reversible DA bonds of the polymer [115]. The increase in tensile properties is due to the effective hybridization of high modulus irreversible DGEBA epoxy resin with the low modulus reversible furan maleimide DA resin.

3.4.1.6 Fracture analysis of tensile self-healing polymer composite

FE-SEM images of tensile fracture surfaces were used to evaluate the influence of hybridization of self-healing polymer matrix. FESEM morphological patterns of fracture surfaces via tensile tests at higher magnification were shown to detect fracture behavior (i.e. brittle or ductile). Figure 3.9 (a,b,c) show fractured surfaces of polymer composites with varied epoxy content. The roughness of the fracture surfaces was considered to determine the fracture behavior and crack diversion mechanism of the composites. The fracture surface of 35DA sample was noticeably smooth with river-like stripes due to lower epoxy weight percentage that is ascribed to brittle fracture, as shown in Figure 3.9 (a). As the epoxy content (45DA) increases, the characteristic stripe structure does not change, however, as the amount of stripes on the surface rises, ensuring a rough morphological surface along with non-homogeneous nature [116], as shown in Figure 3.9 (b). A similar case may be seen with (55DA), where the stripe structure is the same but the edges have more irregularity and the surface roughness is higher, resulting in higher tensile strength than 35DA and 45DA sample.

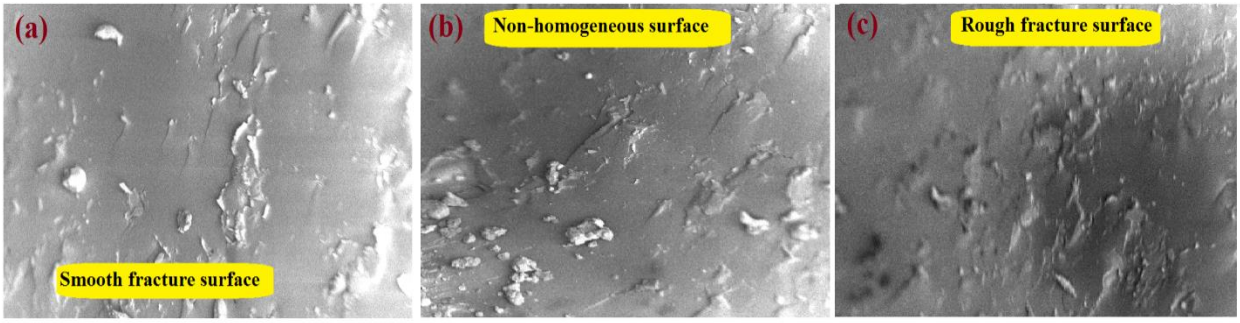

Figure 3.9 FE-SEM fractography images of (a) 35 DA (b) 45 DA (c) 55 DA tensile self-healing polymer composite

3.5 Conclusions

Furfuryl glycidyl ether (FGE) was synthesized and furan maleimide based thermally reversible self-healing polymer composite was fabricated by maintaining stoichiometric ratio of (FGE + DPBMI + DGEBA + MHHPA). The self-healing polymer composites was fabricated through silica mould by exposing to temperature followed by autoclave curing. The chemical architecture

of synthesized self-healing resin, mechanical characterization and fracture morphology of the polymer samples was investigated. The following conclusions can be drawn from the present study.

- Optimum stoichiometric ratio of self-healing resin:
  - 12 g BMI (0.027 mol) + 10.3 g FGE (0.054 mol) mixed at 90 ^{o}C about 5 minutes.
  - With mechanical agitator, 15.21 g DGEBA (45 wt % in BMI, FGE and DGEBA compound) was added to the resultant solution and cured using MHHPA.
- Optimum curing conditions of self-healing polymer:
  - Autoclave - 85 ^{o}C / 8 h, 130 ^{o}C / 8 h, and 85 ^{o}C / 8 h.
- The characterization data of ^{1}H NMR, ^{13}C NMR successfully demonstrates the interaction of furan and oxirane rings in synthesized FGE.
- TG-DSC data reveals that, the formation successive exothermic and endothermic peaks refer to the DA-rDA bond creation and a maximum enthalpy release of 8.16 J/g for 45DA was observed due to superior DA-rDA bond formations.
- The successful integration of low modulus of self-healing resin to high modulus epoxy was revealed through FTIR spectra.
- Healing cycle of fractured polymer composite:
  - Autoclave - 130 ^{o}C / 2 h, and 85 ^{o}C / 2 h.
- The 45 DA sample exhibiting optimum strength with non-homogeneous surface.
- The experimental data demonstrate successful fabrication of thermally reversible furan-maleimide based self-healing polymer composite.

Chapter 4

Evaluation of the exfoliation level effect of oxidation, silane, maleimide functionalization of GNP and MWCNTs

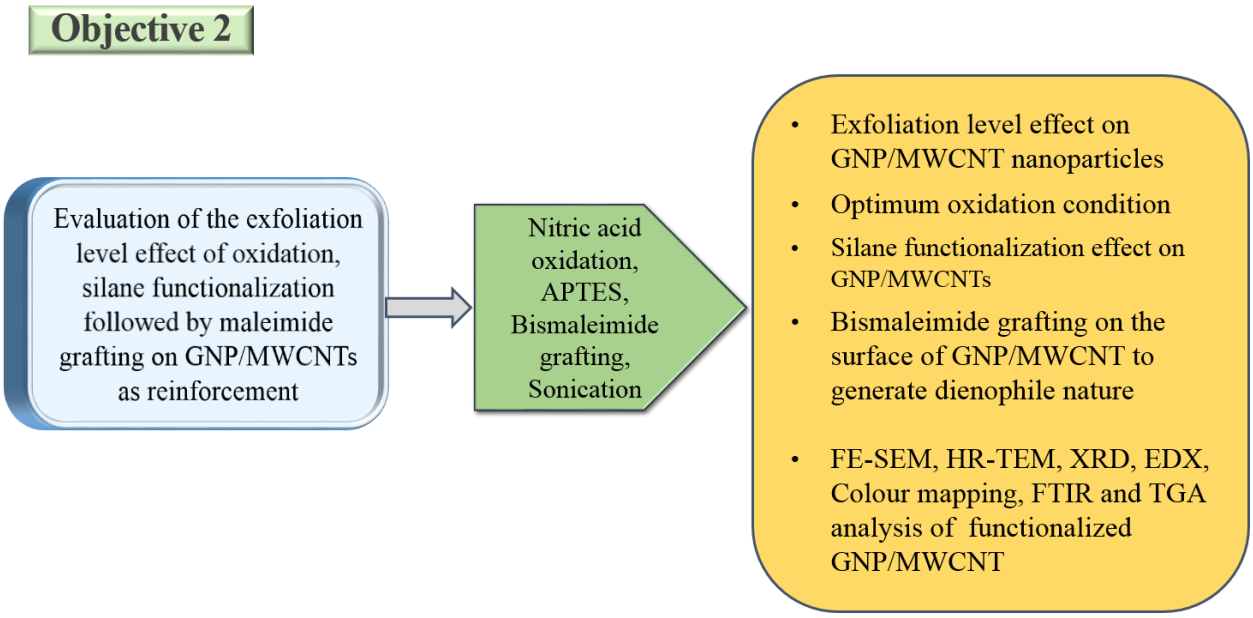

This chapter describes the exfoliation level effect of different oxidation times of graphene nano platelets (GNP) and multiwalled carbon nanotubes (MWCNT). The oxidized GNP and MWCNT was functionalized with APTES silane agent followed by maleimide grafting was used as reinforcement in self-healing matrix. The characterization techniques used to analyse effective grafting of silane and maleimide moieties on the GNP and MWCNT surface.

4.1 Introduction

The self-healing epoxy composite strength can be improved by adding reinforcement in the resin matrix. Nanofiller reinforcement in composites is one of the potential techniques for increasing strength. Generally, nanofillers are prone to agglomeration and have weak interfacial interaction between nanoparticles and matrix. If nanofillers exfoliated as a single atom thick, it can be used as a filler to create high-performance hybrid CFRP self-healing laminates with better interfacial properties. In this work, demonstrates Graphene nanoplatelets (GNPs) and Multiwalled carbon nanotubes (MWCNTs) exfoliation level through facile oxidation process followed by silane coupling functionalization. Nitric acid-HNO_3 was used as oxidation agent and 3-Aminopropyl Triethoxysilane -APTES was used as silane agent. The nanofillers were oxidized with various time periods like 0,48,60,72 h followed by characterization to optimize the period of oxidation for better exfoliation level preceded by silane layer deposition. The oxidation followed by silane functionalization of GNPs and MWCNTs, will not affect their physical properties even after silanaization, and promotes single-layer nanoparticle exfoliation. The structural modification after functionalization may occur on the surface, at the ends of the GNPs and MWCNTs, or both.

The oxidized and silane functionalized GNPs and MWCNTs are grafted with bimaleimide moiety to inherit the self-healing characteristics along with being promoted as a dienophile in the DA adduct. The oxidization-silanization-bismalimdie grafted GNPs and MWCNTs were finally characterized to know the effective grafting of silane and maleimide moieties on the surface and/or at the ends of the nanofillers.

4.2 Materials and Methods

Different types of materials used in preparation of oxidized-silanized-bismaleimide grafted (functionalized) GNPs/MWCNTs are discussed in this section along with method of preparation.

4.2.1 Materials

3-Aminopropyl Triethoxysilane-APTES, 4,4-bismaleimide diphenylmethane (BMI/DPMBMI) were received from Alfa Aesar, India. Finar chemicals Ltd., Mumbai, India supplied analytical quality acetone, toluene, ethanol and Dimethylformamide-DMF. Finar chemicals, India supplied Nitric acid (HNO3). Nanoshell intelligence Materials Ltd. supplied Graphene Nano Platelets with thickness range from 8-20 nm. Nanoshell intelligence Materials Ltd. provided Multiwall Carbon Nanotubes with diameter varying from 2 to 8 nm and length varying from 10 to 20 μm which were used as nanofillers in epoxy. All of the compounds were analytical grade and did not require any further refining. Table 4.1 specifies the list of materials used in the current study and Table 4.2 specifies the materials key data specifications obtained from standard data sheets. Figure 4.1 shows the chemical architecture of the materials used in the current study.

Table 4.1 List of materials used in the present study

Material	Purpose	Purchased from	Remarks
APTES	Silane coupling agent	Alfa Aesar, India	---
DPBMI	Dienophile in DA adduct	Alfa Aesar, India	Spherical grains
HNO3	Exfoliation acid	Finar chemicals Ltd., Mumbai, India	AR grade
Acetone, Ethanol, Toluene, DMF	Solvents	Finar chemicals Ltd., Mumbai, India	AR grade
GNPs	Reinforcement	Nanoshell intelligence Materials Ltd	t- (8-20 nm)
MWCNTs	Reinforcement	Nanoshell intelligence Materials Ltd	d- (2-8 nm)

Table 4.2 Key data specifications of materials used in synthesis

Material	Visual appearance	Density (g/cc)	Storage life (in years)
APTES	clear, liquid	0.946	2
DPBMI	solid	1.2-1.25	1
HNO_3	clear, liquid	1.51	2
Acetone, Ethanol, Toluene, DMF	clear, liquid	--	2
GNPs	Nano platelets	2.3	3
MWCNTs	Nano tubes	1.75	3

Material	Chemical structure
APTES	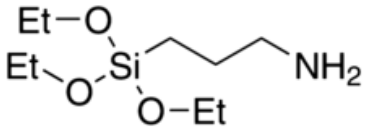
DPBMI	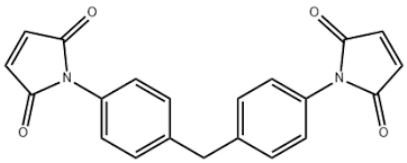
HNO_3	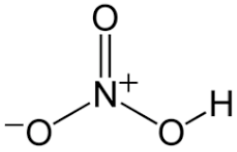
GNPs	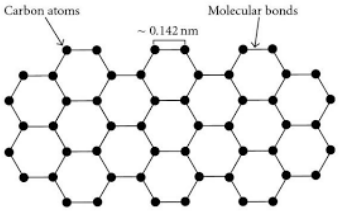
MWCNTs	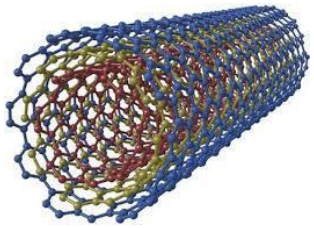

Figure 4.1 Representative chemical structures of materials used in the study

4.2.2 Preparation of bismaleimide grafted functionalized GNPs

Graphene Nano Platelets (GNPs) were functionalized with the maleimide group in three-step approach: GNP oxidation, silane/amine functionalization, and (BMI) maleimide infusion, as illustrated in Figure.4.2.

In a round bottom flask, 0.3 g of GNPPr (pristine GNPs) was reacted to Nitric acid 69 % conc. (HNO_3) about 60 h at 80 ^oC persistent magnetic stimulation under condensation. The resultant mixture was diluted, filtered using DI water (pH7) followed by acetone, ethanol washing. The resultant was cured at 80 ^oC for 12 h using vacuum furnace and named GNPOx (Oxidized GNPs). Using magnetic stirrer, 0.3g of GNPOx was diffused in toluene (20 ml) and combined with

APTES (1wt% GNPOx) using a probe sonicator (69% amplitude) for 20 minutes. The resultant was then stimulated at 1250 rpm at 110 °C, for 8 h in presence of a reflux condenser and then filtered using moisture trap, purified with toluene, ethanol, and acetone successively.

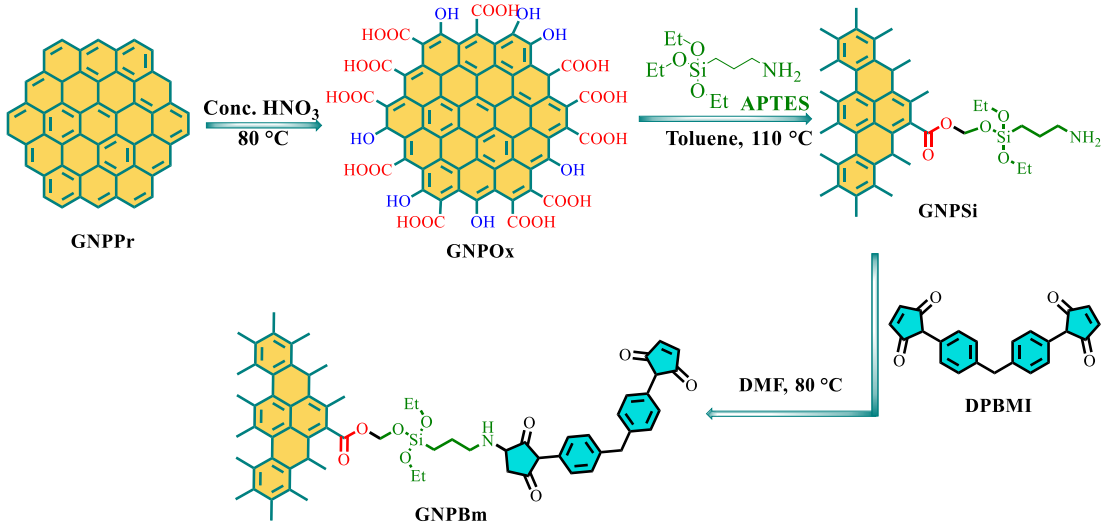

Figure.4.2: Schematic representation of bismaleimide infused GNP functionalization

The resultant mixture was cured at 70 °C overnight using vacuum furnace and named GNPSi (silanized GNPs). For nucleophilic Michael addition, in a round bottom flask saturated DMF-DPBMI solution was prepared by mixing 15 ml DMF with 2 g DPBMI, and added 0.3 g GNPSi, followed by curing at 80 °C for 2 h. The resulting compound was cleaned with DMF, ethanol, and acetone and then cured next to room temperature, named GNPBm (bismaleimide GNPs).

4.2.3 Preparation of bismaleimide grafted functionalized MWCNTs

As illustrated in Figure.4.3, the maleimide group functionalization on Multiwall Carbon Nanotubes (MWCNT) in three steps: oxidation, silane functionalization, and bismaleimide infusion. Initially, 0.3 g of unmodified Pr-MWCNT (pristine) were reacted with 69 % conc. Nitric acid (HNO_3) in a round bottom flask for 60 hours at 80 °C oil bath temperature with persistent magnetic stimulation. Using DI water, the resulting was diluted, filtered, and purified, and pH 7 was obtained using ethanol and acetone washing. The resulting solution was cured in a vacuum furnace at 80 °C for 12 hours and designated as Ox-MWCNT (Oxidized MWCNTs). Under magnetic stirring, 0.3 g of Ox-MWCNT was completely dissolved in 20 mL toluene. Using probe sonicator (69 % amplitude) 5 mL toluene was combined with APTES (1 wt% Ox-MWCNT) in a

previously prepared solution for 15 minutes. The resulting solution was then stirred for 8 hours at 1200 rpm in a reflux condenser at 110 ^{o}C, then filtered and purified using toluene, ethanol, and acetone successively [30].

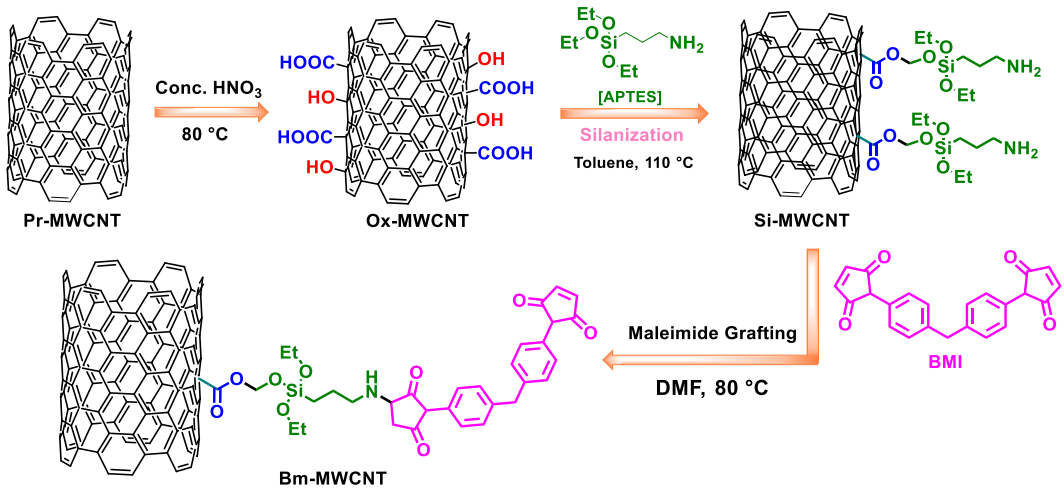

Figure 4.3: Schematic representation of bismaleimide infused MWCNT functionalization

The resulting was heated in a vacuum furnace at 70 °C and given a name Si-MWCNT (silanized MWCNTs). Following that, using the Michael addition technique, Si-MWCNT were fused with the Bismaleimide (DPBMI) moiety using solvent. Saturated DPBMI and DMF solutions were generated in a round bottom flask by mixing (2 g DPBMI with 15 ml DMF), followed by 0.3 g Si-MWCNT addition, and then exposed to 80 ^{o}C temperature for 2 hours using paraffin oil bath to complete nucleophilic Michael addition. After cleaning with DMF, ethanol, and acetone, the resulting was dried at room temperature and given the name Bm-MWCNT (bismalimide MWCNTs).

4.3 Characterization of functionalized GNPs and MWCNTs

Various characterization techniques used to investigate the effect of oxidation and silanaization followed by bismaleimide grafting of the functionalized GNPs and MWCNTs were discussed in this section.

4.3.1 FE-SEM and HR-TEM analysis

Filed emission scanning electron microscopy (FE-SEM) uses high energy electrons to scan the surface of the specimen and the interaction of the electrons with the specimen atoms results in a

variety of signals. Respective detectors pick up these signals and generate scan images that contain details about the surface's composition and morphology.

Surface morphology of the functionalized GNPs and MWCNTs is one of the important aspects to be investigated to confirm the optimum exfoliation level and effective grafting of silane layer and bismaleimide moieties on the surface. In this study (JSM-7600F FEG-SEM) field emission scanning gun electron microscope at 5 kv acceleration voltage was used. Before testing, samples were attached to conductive carbon tape and gold sputtering to avoid charging of the samples during experimentation and to get better image resolution.

High-resolution Trasmission Electrom Microscope (HR-TEM), which differs slightly from other TEM types in its approach, produces a high resolution that can structurally analyse samples at the atomic level. Therefore, it is a highly helpful technique in the investigation of all nanoscale structures. In this study JEM 2100F, HR-TEM transmission scanning electron microscopy was used.

4.3.2 XRD, EDX and Elemental mapping analysis

A nondestructive method known as X-ray diffraction analysis (XRD) can give precise details on a material's crystallographic structure, chemical structure, and physical characteristics. It is based on the constructive interference of crystalline sample and monochromatic X-rays. X-rays are electromagnetic radiation with shorter wavelengths that are produced when electrically charged particles with enough energy are slowed down. In X-ray diffractogram analysis (XRD), the generated X-rays are collimated and directed at a sample of nanomaterials. A diffraction pattern is shown by plotting the intensity of the diffracted rays that are scattered over the material at various angles.

EDAX works on the fundamental premise that an electron beam passes through an object to produce X-rays. The X-rays are produced based on features and structure of the components present in the sample. As a result, this method can also be used to determine the X-rays energy. The spectrum of EDX microanalysis contains both semi-quantitative and semi-qualitative information. An element map is a visual representation of how the elements are distributed throughout a sample. Compared to a simple line traverse, element maps provide a more comprehensive 2D depiction of the internal chemical zonation within a mineral. Element maps are

particularly helpful in illustrating compositional zonation and element distributions in textural context. The XRD, EDX and Elemental mapping was carried to identify the elements present before and after functionalization.

4.3.3 FTIR spectra analysis

Using a Bruker Alpha II Fourier transform Infrared spectrometer (FTIR) with a wavenumber range of 4000 cm^{-1} to 400 cm^{-1} and a resolution of 2 cm^{-1}, the molecular architecture and functional groups present in the functionalized GNPs and MWCNTs. The functionalized GNPs and MWCNTs were blended with potassium bromide (Kbr). The FTIR spectra was observed in the transmittance mode.

4.3.4 TG-DTA analysis

Thermogravimetry Differential Thermal Analysis, often known as TG-DTA, is a thermal analyzer that can simultaneously measure a sample's various thermal properties in a single experiment. The TG component measures the temperatures at which oxidation, reduction, or decomposition takes place. It evaluates sample weight changes due to oxidation, decomposition, and any other physical or chemical processes that causes weight gain or loss. The DTA component measures decomposition processes are classified as exothermic or endothermic. The DTA also measures temperatures corresponding to phase transitions including melting, crystallisation, and glass transitions where no mass loss takes place on the surface of GNPs and MWCNTs.

4.4 Results and Discussions

This section deals with physical chemical architecture alteration of functionalized GNPs and MWCNTs before and after bismaleimide grafting, measures the temperatures and weight changes at which oxidation, reduction, or decomposition takes place, and any other physical or chemical processes that causes weight gain or loss.

4.4.1 Physical and chemical charactterization of malimide functionalized GNPs

The physical and chemical characterization of bismalemide functionalized GNPs are carried through FE-SEM, HR-TEM. XRD, EDX, mapping and TG-DTA to verify the effective grafting of bismaleimide moiety on the GNPs surface.

4.4.1.1 FE-SEM analysis functionalized GNPs

Using a high resolution FESEM, the morphological studies of GNPPr, GNPSi and GNPBm were performed. Each sample was keenly studied at lower and higher magnification to identify morphological variations with respect to silane-DPBMI functionalization on GNPs surface.

Figure.4.4 (b,d, and f) illustrates higher magnification images at 100 nms and Figure 4.4 (a,c and e) shows the lower magnification images at 1µm, and. Figure 4.4 (a and b) correspond to the pristine GNPs and the validation of the aggregation of the GNPs was clearly seen through the numerous layers of graphene. Tightly bonded layers of graphene nanosheets without any infinitesimal interlayer spacing were obtained near higher magnification at 100 nm and are shown in Figure 4.4 (b). This tendency of being in several packed layers of pristine GNPs can be explained as the agglomeration of weak Vander Waal attraction forces between them, which is indicated through arrow marks in Figure 4.4 (a).

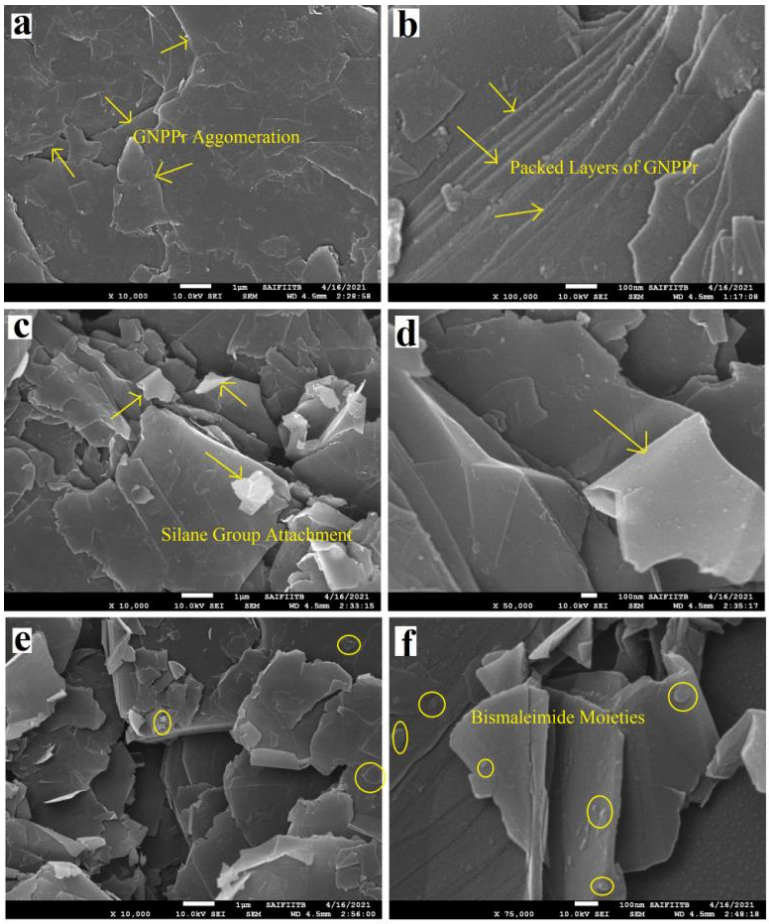

Figure 4.4 FE-SEM images of (a,b) are GNPPr, (c,d) are GNPSi and (e,f) are GNPBm

Silanization is performed on oxidized GNPs to further nullify the agglomeration between GNPs sheets. This is achieved by converting the obtained hydrophilic GNPs from oxidation to hydrophobic GNPs by the attachment of silane functional group during salinization. The coarse irregular surface along with white flake diffusion reveals the attachment of saline functional groups to GNPPr [117]. In addition, Malemide was infused on silanized GNPs surface to change from GNPSi to GNPBm, which act as a dienophile in DA and r-DA bonding. The covalent bond between GNPBm bismelamide and GNPSi amine functional groups is explained with the help of globular shaped moieties on GNPBm which were assumed to be bismalemide moieties, as demonstrated in Figure 4.4 (e and f).

4.4.1.2 HR-TEM analysis functionalized GNPs

HR-TEM studies were carried out on GNPSi and GNPBm samples in order to get high-resolution morphological alterations due to functionalization and to further confirm effective grafting of maleimide moieties with amine functional groups.

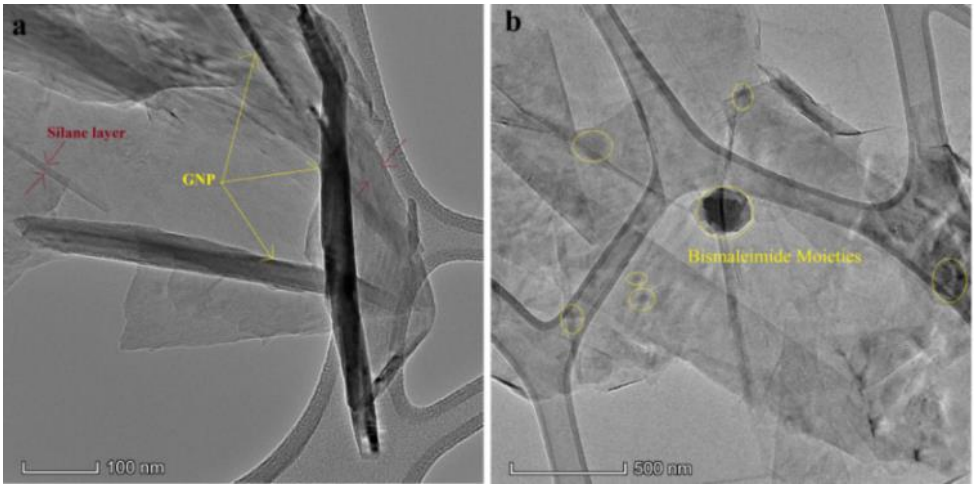

Figure 4.5: HR-TEM morphological investigation on (a) GNPSi and (b) GNPBm

HR-TEM images of GNPSi and GNPBm are shown in Figure 4.5. The uniform layer of silane functional groups is attached to GNP's surface with a tiny portion of layer exfoliation, as shown in Figure 4.5(a). The TEM graphs in Figure 4.5(b) show that the bismalemide functional group is deposited in globular structures on silanized GNPSi, which is also supported by FE-SEM graphs [118].

4.4.1.3 XRD analysis functionalized GNPs

X-Ray diffraction patterns of untreated (pristine), silane, and maleimide functionalized Graphene nanoplatelets (GNPs) were carried out and the results are shown in Figure 4.6.

The characteristic peaks detected at an angle 2θ = 26.51°, 44.73°, and 56.84° correspond to the diffraction planes of (002), (101), and (004), respectively, indicating that GNPs have a graphitic structure [119]. The diffraction peak intensity of GNPSi, GNPBm was much larger than that of pristine GNPs, results in bi-product elimination indicating more prominent graphite structure and leads to separated graphene layers with less aggregation. The diffraction peaks were well matched with standard data of JCPDS card No (75-2078). The absence of other peaks in the X-Ray diffraction results indicates that the samples are pure.

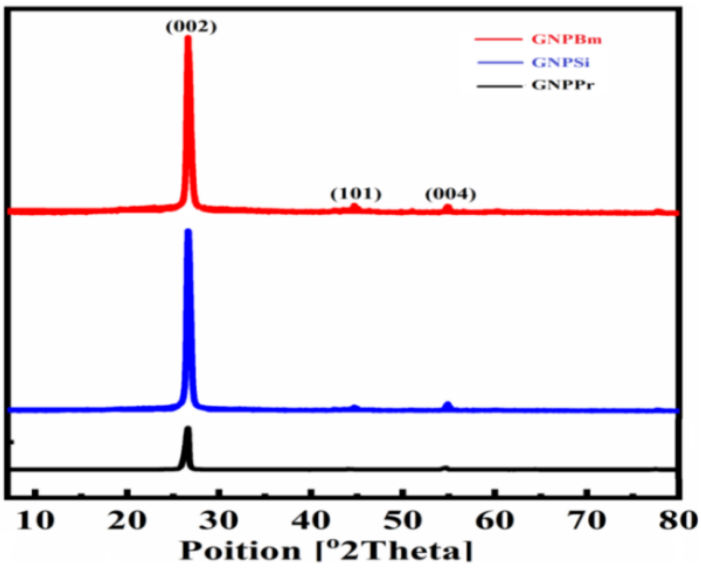

Figure 4.6: X-ray Diffraction pattern of GNPPr, GNPSi and GNPBm

GNPs mean crystalline size was calculated using Debye- Scherrer's formulae: Eq. (4.1) $D = \frac{0.9\,\lambda}{\beta \cos\theta}$ nm, where D – mean crystal domain size; β – Braggs peak (FWHM = 0.4517 radians) Full Width Half Maximum; λ - X-ray wavelength (0.154056 nm) for (Copper Kα tube); θ = 26.51 radians – diffraction reflection angle. The GNPs mean crystalline size D was revealed as 18.8 nm. Lattice strain is a proportion of the distribution of lattice parameters caused by crystal imperfections. The

lattice strain (ε) due crystal defects was revealed from Stokes-Wilson Eq. (4.2) $\varepsilon = \frac{\beta \cos\theta}{4}$. Using X-Ray line enlargement the dislocation densities (δ) was computed using Eq. (4.3) $\delta = \frac{1}{D^2}$.

Table 4.3: Crystalline domain size, Lattice strain and Dislocation densities of GNPs.

Sample	Crystalline domain size (nm)	Lattice strain	Dislocation density
GNPPr	18.88	0.101	0.0028
GNPSi	17.41	0.109	0.0032
GNPBm	16.82	0.113	0.0035

4.4.1.4 EDX and Elemental mapping functionalized GNPs

The molecular evidence of the globular-shaped BMI was confirmed through elemental analysis of GNPSi and GNPBm shown in Figure 4.7.

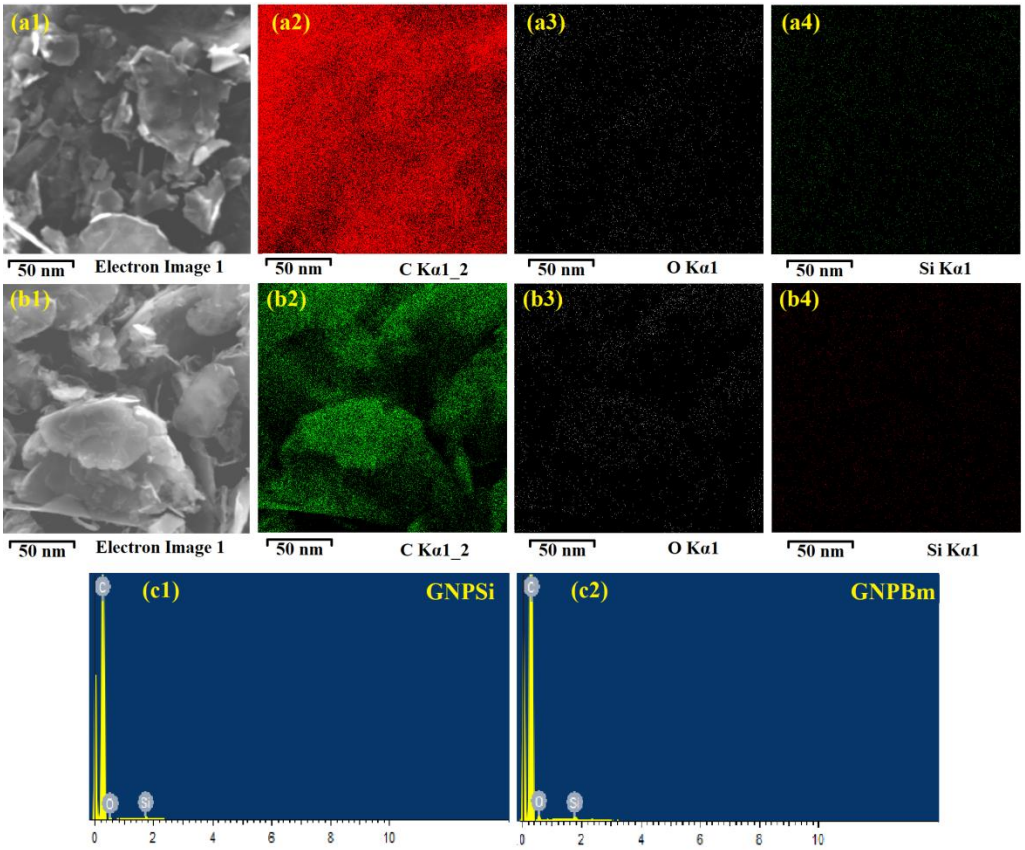

Figure 4.7: Elemental Mapping and EDX spectra images GNPSi and GNPBm

The mapping zones of GNPSi and GNPBm, as well as the elemental investigation of C, O, and Si, were studied. In the case of GNPSi, GNPBm, the oxygen molecule observed in Si-O-Si link fo APTS and the C=O bond of BMI respectively, and evenly distributed in the entire mapping region. The adsorption of bismaleimide to GNPSi is mainly because of covalent bonds creation between the bismaleimide and amine groups. Figure 4.7 (a4, b4) shows equally attached silane moieties constituting Si elements on GNPBm surface [120]. Thus, using EDX elemental mapping and FE-SEM morphology, the effective infusion of DPBMI on GNPSi surface was confirmed. These functionalized GNPBm can be used to strengthen a composite, forms DA adduct that promotes interfacial self-healing capability.

The EDX graphs of the images of GNPPr, GNPSi and GNPBm are shown in Figure 4.7. The purity of the samples was claimed with the chemical content in the sample and no other impurities were recorded. In all two samples, carbon was the principle element with almost 95 % presence. It is observed that the rise of oxygen content in GNPBm compared to GNPSi is ascribed to the evidence of grafting of besmelamide moieties on GNPs via covalent bond formation.

4.4.1.5 TG-DTA analysis of functionalized GNPs

The thermal stability of GNPPr, GNPSi and GNPBm was investigated by thermo-gravimetric analyzer to explore successful covalent functionalization of GNPs as shown in Figure 4.8

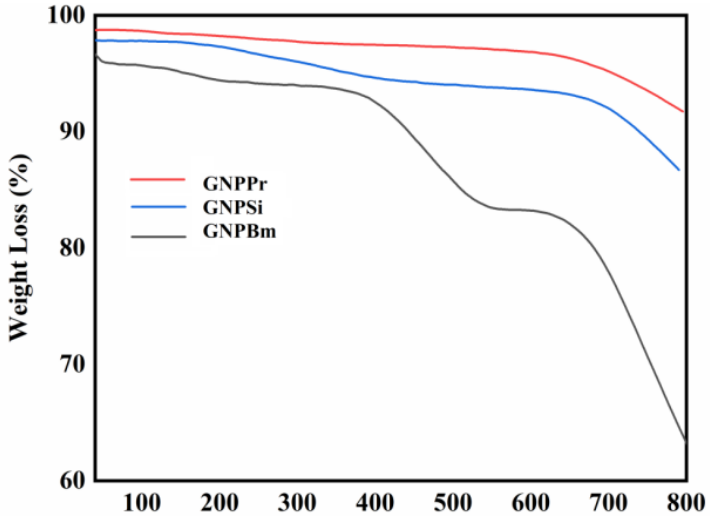

Figure 4.8: Weight loss curves of GNPPr, GNPSi, and GNPBm

The thermal trend of GNPPr shows initial mass degradation at 100 ^{o}C, which is mostly due to surface moisture elimination, followed by no significant degradation was observed. GNPSi thermal pattern indicates a progressive weight loss of 10% over the temperature range. The degradation of GNPSi at 350 ^{o}C is due to the removal of oxygenated functional groups such as carbonyl, hydroxylic acid, and carboxylic group, followed by the formation of a thrixosilane layer on the surface [121]. Furthermore, due to bismaleimide moiety grafting on the surface of GNP, the GNPBm thermal pattern showed major degradation compared to GNPPr and GNPSi. At 200 ^{o}C degradation of furan-maleimide functional moiety on the surface of GNPBm was observed [122]. Around 350 ^{o}C, there was a significant degradation due to oxygenated and thrixosilane group removal, leaving an 83% residual mass. The graphene pyrolysis thermo-chemical treatment of carbon skeleton further destroyed GNPBm at a temperature range of 600 ^{o} – 700 ^{o}C. The bismaleimide functional group was successfully deposited on the surface of graphene nanoplatelets and confirmed through TGA studies.

4.4.2 Characterization of oxidized and silanized MWCNTs

Various characterization techniques like, FE-SEM, HR-TEM, TG-DTA and XRD was carried to estimate the optimum HNO_3 oxidation time to exfoliate MWCNTs as single tube thick followed by silane layer attachment on the MWCNTs surface.

4.4.2.1 FE-SEM analysis of oxidized MWCNTs

A bifunctional molecule that reacts with the fillers and the polymer is needed to connect inorganic nanofillers and the CFRP matrix. To study the influence of different oxidation durations (48/60/72 h) and APTES silanization on pristine MWCNTs, we initially concentrated on morphological analysis using FE-SEM, as shown in Figure 4.9. In line with expectations, the FESEM image of the MWCNT-Pr (Figure 4.9a) showed an aggregation between several hundred nanotubes connected by a weak van der waals attraction. As MWCNT-Pr oxidization with nitric acid (HNO_3), a nanotube exfoliation is intended, resulting in the bonding of oxygenated chemical compounds such as O-H (hydroxylic), C=O (carbonyl) and COOH (carbocylic) on the surface. The oxidizing effect allows the MWCNT-Pr to benefit from de-aggregation by reducing the interfacial attraction forces [123].

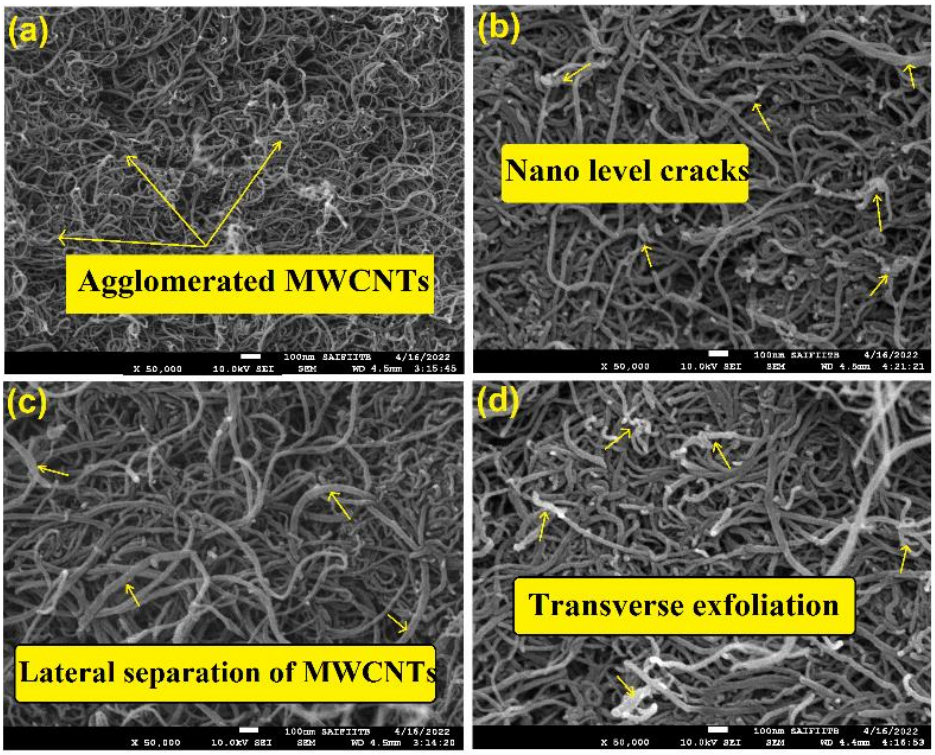

Figure 4.9. FE-SEM image of (a) Pristine MWCNT (agglomeration of nanotubes), (b) OAC-60 showing nano-level ruptures (shown by arrow marks) (c) OAC-60 showing sufficient lateral and transverse exfoliation (d) OAC-72 showing tiny transverse agglomeration

Although the MWCNTs remained aggregated after 48 hours of oxidation (OAC-48), attractively, nano-scale fissures are produced on the nanotube surface (Figure 4.9b shown by arrows). As shown in Figure. 4.9 (c, d), these nano-level fissures continue to accelerate the lateral exfoliation of MWCNT after 60 h (OAC-60) as well as 72 h (OAC-72). Additionally, transverse separation is seen for OAC-60 under FESEM along with the lateral exfoliation of the MWCNTs, and the combination of these exfoliations creates a 3D networked nanotube structure with tiny openings. This 3D networking structure is anticipated to have two benefits: first, it will allow for the homogeneous silane oligomer grafting onto the nanotube edges and surfaces through silanization, and second, it provides greater access for epoxy resin crosslink to build a robust interface [124]. Significant transverse agglomeration is observed in the case of OAC-72, probably as a result of additional lateral dispersion of MWCNTs, which may have enhanced the surface energy of MWCNTs (Figure 4.9d). The sieving function of the fibers is expected to prevent infusion of CFRP intra-laminar zones that exhibit either or both transverse and lateral aggregation. In the

hybrid CFRPs, the network of distinctive OAC-60s is predicted to be a more favorable interaction with the epoxy structure. It may show a greater ability to lay close to the carbon fibers effectively.

4.4.2.2 HR-TEM analysis oxidized MWCNTs

To determine the efficiency of silane moiety infusion on the surface of MWCNTs, HR-TEM micrograph analysis of O.A.C. (48/60/72 h) was performed, and the results were reported in Figure. 4.10.

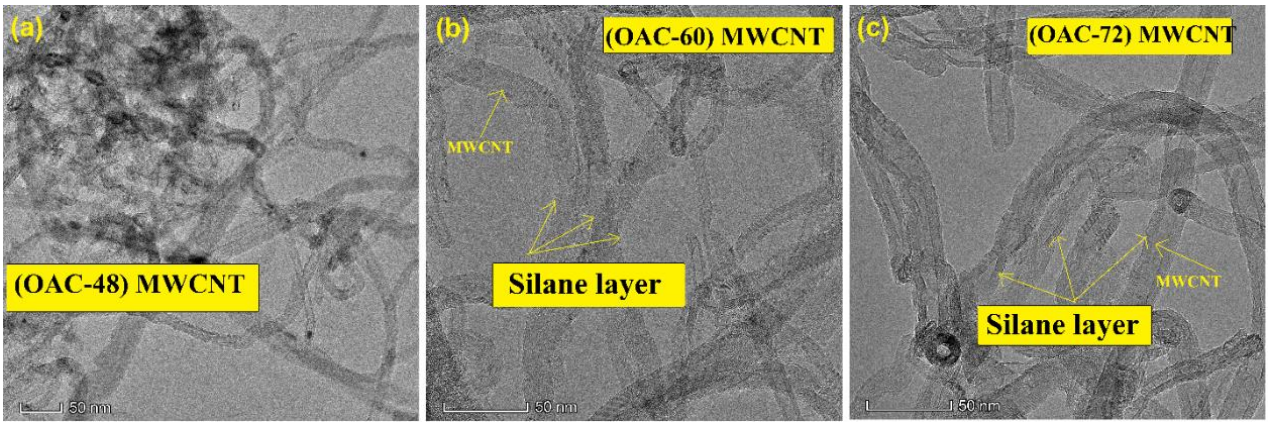

Figure 4.10. **HR-TEM micrographs of (a) O.A.C. 48h (b) O.A.C. 60h (c) O.A.C. 72h**

With a minimal amount of layer exfoliation, the homogeneous layer of silane functional moieties adhering to the surface of MWCNT was observed for OAC-48, as depicted in Figure 4.10(a). However, transverse direction exfoliation and the lateral separation of the carbon nanotube occur after oxidation for a period of more than 48 h. These phenomena are distinguishable in the OAC-60 and OAC-72 samples Figure (4.10 (b, c)). For OAC-60, there may be a noticeable amount of exfoliation of the silane layer-infused nanotube was observed. Furthermore, the OAC-60 surface roughness is more prominent than that of OAC-48 (shown by arrows). Therefore, the roughness can be ascribed to uniform silane functional moiety presence [125]. The MWCNTs multilayer structure was mainly preserved during the oxidation and silanization process. However, in the case of OAC-72, the lateral splitting of the MWCNT and the exfoliation of nanotubes have formed a step-like pattern discovered as aggregation after washing and drying. It may be concluded that effective adsorption of several oxygenated groups to the surface of MWCNTs during oxidation with HNO_3 for at least 60 h, followed by silanization, can lead to successful exfoliation of nanotubes.

4.4.2.3 XRD analysis of oxidized MWCNTs

X-Ray diffraction of unprocessed (pristine), silane functionalized MWCNTs with different oxidation times were carried, and the results are represented in Figure 4.11. MWCNT exhibited an intense sharp diffraction peak at 2θ = 26.29º attributed to diffraction plane (002). This peak demonstrates that the MWCNTs graphite structure underwent acid oxidation followed by salinization without considerable damage.

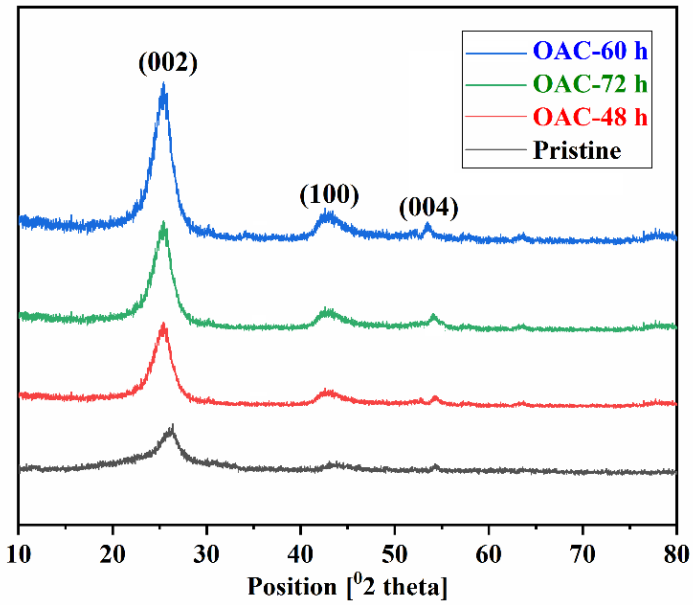

Figure 4.11. XRD analysis of pristine and functionalized MWCNTs

When the MWCNTs are treated with an acids/silane group, their crystallinity order weakens, and the diffraction pattern moves to lower angles [126]. The other distinctive diffraction patterns of MWCNT were observed at 2θ = 44.38º and 54.48º, which correspond to the diffraction planes (101) and (004), respectively. The functionalized MWCNT (OAC-60) diffraction peak intensity was significantly higher than other MWCNTs, showing that bi-product removal resulted in pronounced graphitic structure and distinctive MWCNTs along with precise exfoliation. According to the standard spectral data, the MWCNT's characteristic peaks are successfully confined (JCPDS/41–1487). MWCNTs mean crystal size was estimated using Debye-Scherrer's formulae: Eq. (4.1) $D = \frac{0.9\,\lambda}{\beta \cos\theta}$ nm, where β – Braggs peak/FWHM = 2.24; D – mean crystal domain size; θ = diffraction reflection angle (radians); λ - wavelength of X-ray (0.154056 nm) for (Cu/Kα

tube). Lattice strain results from crystal flaws and is a fraction of disseminated lattice constants. The ε-lattice Strain was exposed from Stokes-Wilson Eq. (4.2) $\varepsilon = \frac{\beta \cos\theta}{4}$. Dislocation densities (δ) were calculated using X-Ray line enlargement, Eq. (4.3) $\delta = \frac{1}{D^2}$. The mean crystal size and lattice strain of MWCNT-Si(60) were found to be 4.05 nm, and 0.0522, respectively and the values are listed in Table 4.4.

Table 4.4. Mean crystal size (nm), Dislocation density (δ) and Lattice strain (ε)

Sample Code	Crystal domain size (nm)	Dislocation density(δ)	Lattice strain(ε)
MWCNT-Pr	3.08	0.1054	0.0173
MWCNT-Si(48)	3.47	0.0711	0.0259
MWCNT-Si(60)	4.05	0.0407	0.0522
MWCNT-Si(72)	3.89	0.0643	0.0396

4.4.2.4 TG-DTA analysis oxidized MWCNTs

TG/DTA was used to evaluate the thermal stability of pristine and silanized MWCNT (OAC-48/60 h) under an N_2 environment. The results are displayed in Figure 4.12. Pristine MWCNTs hardly degrade at below 600 °C temperature, leaving a residue of about 96.8 wt. % due to moisture elimination at 100 ^{o}C.

The silanized MWCNT (OAC-48/60 h) exhibits a progressive weight loss of around 12-14 wt. % throughout the temperature range [93]. At 330 ^{o}C, significant mass degradation was observed due to the evaporation of hydroxylic acid/carbonyl/carboxylic functional groups, followed by thrixosilane layer decomposition on the Si-MWCNT surface. At temperatures between 600 and 700 °C, the carbon skeleton underwent pyrolysis, a thermo-chemical process that further degrades Si-MWCNT. The increasing mass decomposition of the functionalized MWCNT provides evidence that the silane functional group was successfully infused onto the MWCNT surface. Furthermore, the DTA curves demonstrate that, particularly for O.A.C. (48/60 h), the temperature associated with the maximal degradation rate is higher due to the stronger covalent connections generated between the silane moiety molecules and the surface of the MWCNTs.

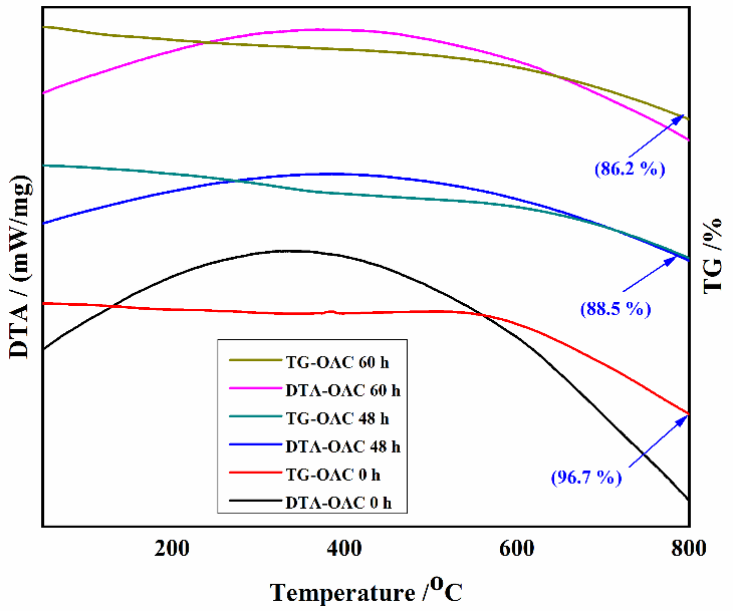

Figure 4.12 Weight loss percentages of functionalized MWCNTs through TG-DTA analysis

4.4.3 Characterization of bismaleimide grafted functionalized MWCNTs

The morphological changes of silanized and bismaleimide functionalized MWCNTs were examined through FE-SEM, HR-TEM and elemental mapping. The thickness changes of functionalized MWCNTs are calculated through XRD analysis and Halder-Wagner plots.

4.4.3.1 FE-SEM analysis bismaleimide grafted functionalized MWCNTs

The morphological studies of Pr-MWCNT, Si-MWCNT, and Bm-MWCNT are carried out using a high resolution FESEM. Every sample was keenly examined under high and low magnification to detect morphological alterations associated with maleimide functionalization of MWCNTs. The functional group degradation over temperature were studied using TG-DTA analysis.

The Figure. 4.13 (a,c and e) demonstrates the lower magnification at 1µm and Figure. 4.13 (b,d, and f) demonstrates the higher magnification at 100nms. The validation of the aggregation was readily apparent by the multiple layers of MWCNTs shown Figure. 4.13 (a). forces by the weak Vander Waal forces.

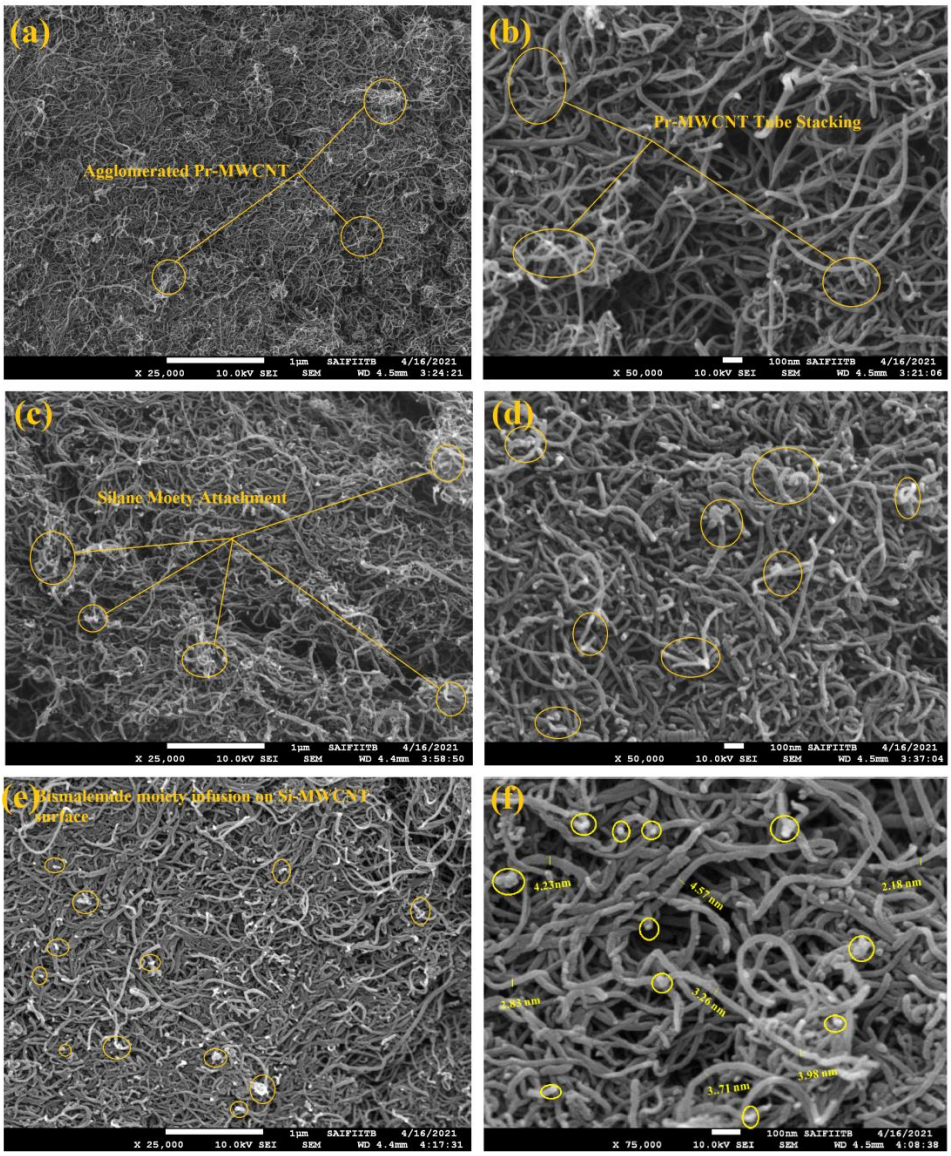

Figure 4.13: FESEM images of (a,b) are Pr-MWCNT, (c,d) are Si-MWCNT and (e,f) are Bm-MWCNT

This aggregation due to weak Vander Waals attraction forces between MWCNT layers, as indicated by circles, in Figure (a,b). The effect of oxidation and silanization on pristine MWCNTs was investigated shown in Figure 4.13 (c,d), which shows significant changes in surface morphology when compared to Figure 4.13 (a,b). As MWCNT is oxidized with HNO_3, an exfoliation is anticipated resulted in the attraction of the oxygenated functional group such as carbonyl (C=O), hydroxylic acid (O-H), carboxylic group (COOH) [123] at the edges on the MWCNTs. The oxidation effect offers the pristine MWCNT to gain advantage of de-

agglomeration by weakening the inter-sheet attraction. The oxidized MWCNTs are salinized to reduce aggregation between the MWCNT tubes. This is accomplished by attaching a saline functional group to the generated hydrophilic MWCNTs after oxidation, resulting in hydrophobic MWCNTs. The attachment of silane functional groups to Ox-MWCNT is shown by the coarse uneven surface with white flake dispersion [127]. Bismalemide was grafted on the surface of Si-MWCNT to convert it into a dienophile. The globular shaped moieties on the Bm-MWCNT tubes are predicted to be the bismalemide moieties, which associates the covalent link between maleimide and amine functional groups as shown in Figure 4.13 (e and f). It was discovered that particle size estimated from Halder-Wagner and Scherrer's approach, which fall within the range of 2-4 nm, has a strong resemblance with the average particle size estimated based on morphological research of FE-SEM, HR-TEM. As a result, the average particle size of functionalized MWCNTs lies in between 2-4 nm with high aspect ratio around 2400.

4.4.3.2 HR-TEM analysis and elemental mapping of functionalized MWCNTs

HR-TEM micrograph analysis of Si-MWCNT, Bm-MWCNT was carried to identify effective silane and maleimide moeity infusion on the surface of MWCNTs.

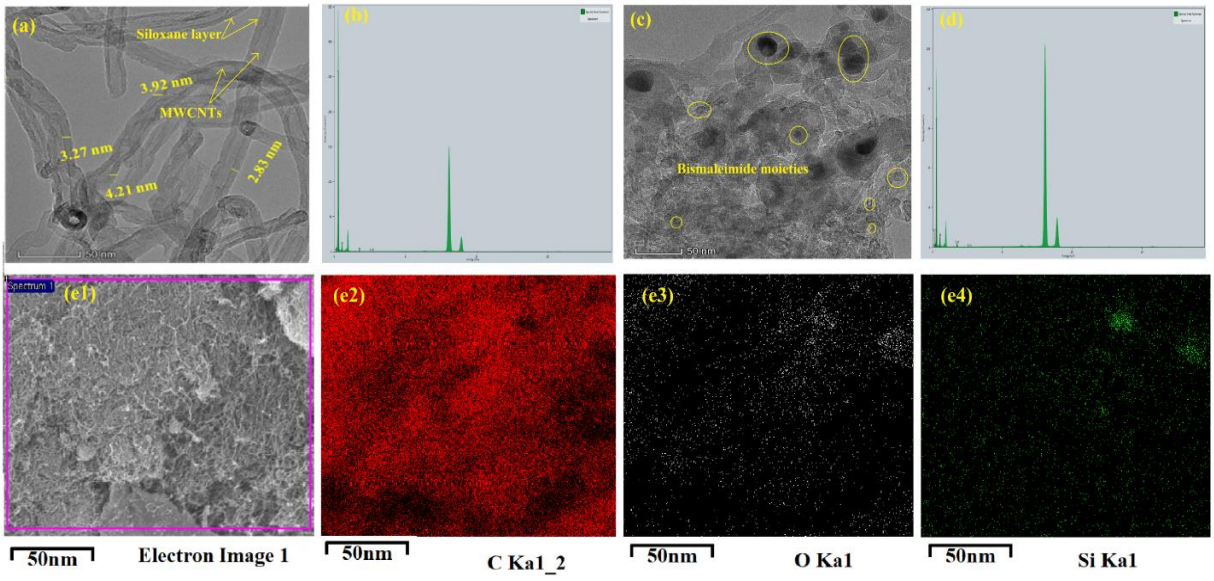

Figure 4.14 TEM investigation on (a,b) Si-MWCNT with EDX (c,d) Bm-MWCNT with EDX (e) Elemental mapping images of C, O, Si respectively.

The successful functionalization is projected to be the infusion of the maleimide moiety as a globular structure on the surface of Si-MWCNT [128]. The EDX mapping (Figure 4.14 c,d) of Si-MWCNT and Bm-MWCNT, an oxygen atom was discovered in the Si-O-Si group of APTS and (-C=O) group of bismaleimide respectively. Another finding from EDX was that Bm-MWCNT had greater oxygen weight content than Si-MWCNT, which could be due to malimide infusion via covalent bond formation.

Elemental analysis of Bm-MWCNTs was performed to confirm the globular-shaped BMIs molecular evidence. The elemental examination of C, O, and Si, as well as the mapping zone of Bm-MWCNT, were studied under HR-TEM. In the case of Bm-MWCNT Figure 4.14 (e3), the oxygen atoms located in and C=O bond of BMI are uniformly dispersed throughout the mapping area. The attachment of maleimide moieties on Si-MWCNT is mostly due to the creation of covalent bonds between the maleimide and amine groups. Figure 4.14 (e4) displays evenly coupled silane moieties comprising Si moieties on Bm-MWCNTs surface [120]. Thus, using FE-SEM and HR-TEM morphological analysis, we have proven the efficient infusion of DPBMI on Bm-MWCNT surface. These functionalized Bm-MWCNTs can be reinforced in self-healing composites, forming a DA adduct and capable in interfacial healing composite and filler.

4.4.3.3 XRD analysis and Halder-Wagner plots of functionalized MWCNTs

The diffraction peaks identified at $2\theta = 26.29^{o}$, 44.38^{o}, and 54.48^{o} corresponds to (002), (101) and (004) diffraction planes respectively, demonstrating MWCNT have a graphitic structure shown in Figure 4.15. The (002) diffraction peak intensity shows broaden due to finite number of MWCNT tubes and curvature [126]. The morphology and crystalline of MWCNTs are substantially conserved during silane and malemide functionalization, according to the XRD patterns of pure and functionalized MWCNTs. The diffraction peak intensity of functionalized MWCNTs was much higher than that of untreated MWCNTs, indicating that bi-product elimination results in more prominent graphitic structure, attributes distinct MWCNTs with minimal aggregation [129]. Individual MWCNT layer exfoliation was caused by functionalization, which rendered the oxide diffraction peak at ($2\theta = 11.01^{o}$) utterly obsolete in X-Ray diffraction pattern properties. The MWCNTs diffraction peaks are well confined with standard diffraction data of JCPDS file No (41-1487).

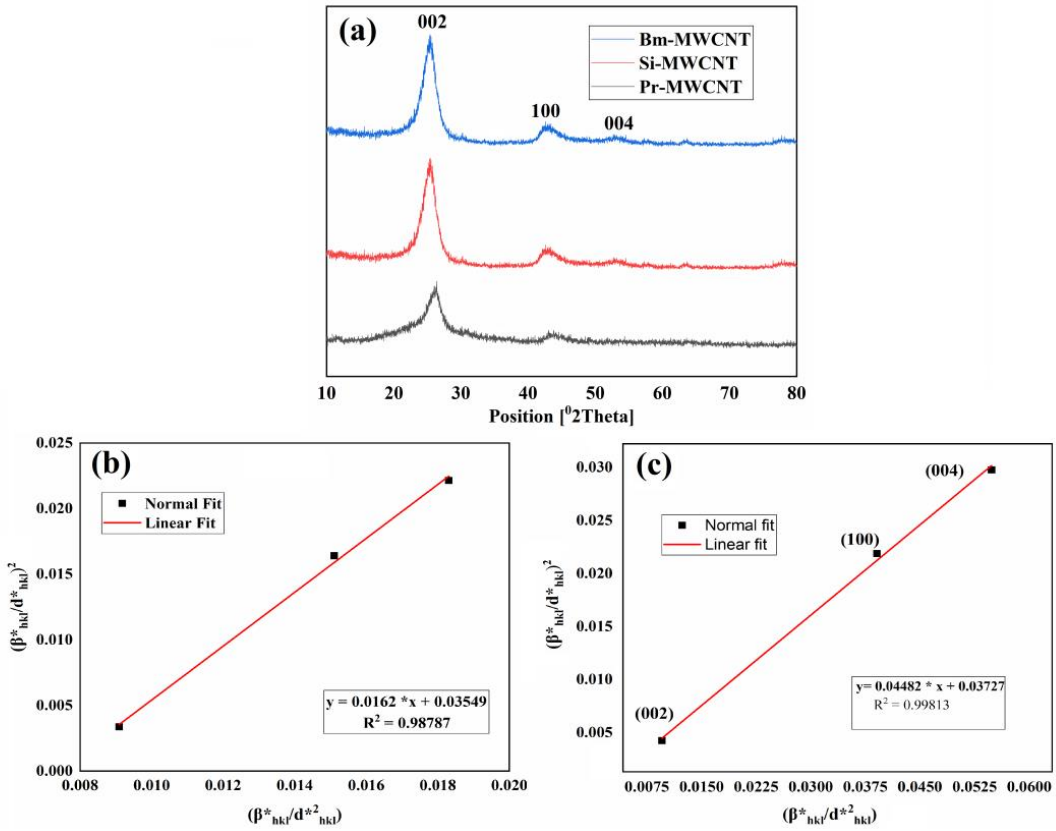

Figure 4.15 (a) XRD analysis of MWCNT, Halder-Wagner plots of (b) Si-MWCNT and (c) Bm-MWCNT

The Debye-Scherrer's formulae [123] were used to calculate the average crystal domain size of the MWCNTs, as follows: D = $\frac{0.9\,\lambda}{\beta\cos\theta}$ nm, where D – average crystal domain size; λ–(X-Ray wavelength-0.154056 nm) for (Copper Kα tube); β – Braggs peak (FWHM = 2.24) Full Width Half Maximum in radians; (θ=26.29°) – diffraction reflection angle. The average crystal domain size D was discovered to be 3.08 nm of MWCNTs based on the diffraction plane peaks. Crystal defects cause lattice strain, which is a proportion of the dispersion of lattice constants. The crystal defect caused the lattice strain (ε), and dislocation was computed using Stokes-Wilson $\varepsilon = \frac{\beta\cos\theta}{4}$. The following $\delta = \frac{1}{D^2}$ where D is the average crystal domain size was used to evaluate dislocation densities (δ) in the sample using X-Ray line broadening. The Halder-Wagner approach assumes a symmetrical Voigt function for peak broadening [127]. According to the Halder-Wagner technique, the crystal domain size and lattice strain are related by $\left(\frac{\beta^*_{hkl}}{d^*_{hkl}}\right)^2 = \frac{1}{D}\left(\frac{\beta^*_{hkl}}{d^{*2}_{hkl}}\right) + \left(\frac{\epsilon}{2}\right)^2$ where $d^*_{hkl} = 2d_{hkl}\,Sin\theta/\lambda$ and $\beta^*_{hkl} = \beta_{hkl}\,Cos\theta/\lambda$ and Plot $(\beta^*_{hkl}/d^{*2}_{hkl})$ $(\beta^*_{hkl}/d^*_{hkl})^2$ along X and Y-

axis respectively for each diffraction XRD peak [130]. The functionalized MWCNTs average crystal size is determined by the slope of the depicted straight line, whereas the lattice strain is determined by the intercept. The average particle size and strain has been calculated as 3.97 nm and 0.448 respectively from Halder-Wagner plot.

Table 4.5: Crystal domain size, Lattice strain of functionalized MWCNTs.

Sample	Scherrer Method		Halder-Wagner Method	
	Crystal size D (nm)	Lattice strain (ε)	Crystal size D (nm)	Lattice strain (ε)
Si-MWCNT	3.45	0.01090	3.72	0.0162
Bm-MWCNT	3.76	0.03110	3.97	0.0448

4.4.3.4 TG-DTA analysis of functionalized MWCNTs

TG-DTA was performed on MWCNTs to monitor weight loss under steady rate heating and to evaluate samples thermal stability. TG-DTA weight loss patterns of Pr-MWCNT, Si-MWCNT, Bm-MWCNT were displayed in Figure 4.16.

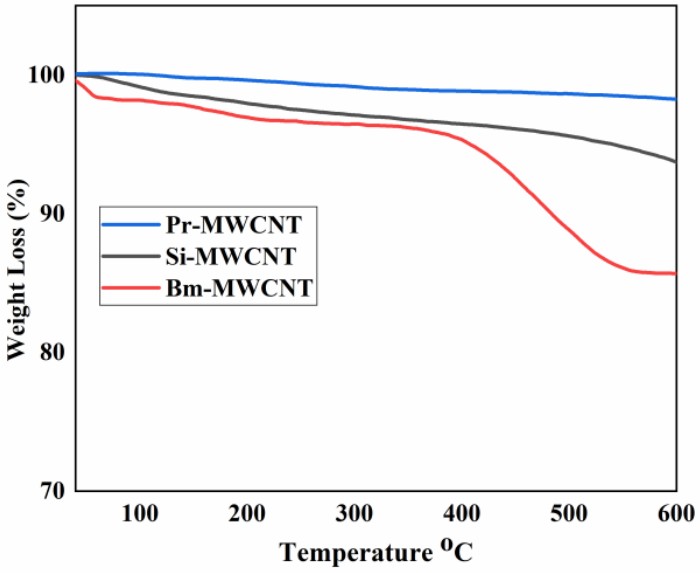

Figure 4.16: Weight loss curve of Pr-MWCNT, Si-MWCNT, and Bm-MWCNT

The Pr-MWCNT demonstrating excellent thermal stability throughout temperature range and small mass degradation was observed at 100 °C attributes to moisture elimination. The thermal

trend of Si-MWCNT shows a gradual weight loss of about 8 percent over the temperature range and mass degradation at 340 ^{o}C due to elimination of carbonyl, hydroxylic acid, and carboxylic group [131]. Furthermore, Bm-MWCNT exhibits 14% weight loss compared to Pr-MWCNT results in furan-maleimide functional group elimination observed between (210-270 ^{o}C). There was a considerable degradation around 370 ^{o}C due to the elimination of thrixosilane and oxygenated groups, leaving an 86 percent residual mass. The Bm-MWCNT further degraded due to pyrolysis treatment of carbon Skelton. The progressive mass degradation of functionalized MWCNT confirms the successful infusion of bismalimde group on the MWCNT surface.

4.4.3.5 FTIR spectra analysis of functionalized MWCNTs

FTIR spectra for functionalized MWCNT samples are reported in Figure 4.17. The characteristic peak 3787 cm^{-1} is attributes to free (-OH) hydroxyl group, whereas 1410 cm^{-1} and 3440 cm^{-1} bands are associated to the stretching frequencies (–OH) in (C–OH) and (OC-OH) respectively. The vibration modes of both symmetric and asymmetric (C–H) groups of MWCNT are related with the infrared absorptions at 2937, 2849, and 848 cm^{-1}. The (-C=C) conjugate stretching is attributed to the band peaks ranging from 1639-1565 cm^{-1}. The band peaks ranging from 1120-980 cm^{-1} attributes to (-C-O) stretching vibration in alcohols. The existence of these band peaks in the pristine MWCNT sample is due to either oxidation or ambient moisture.

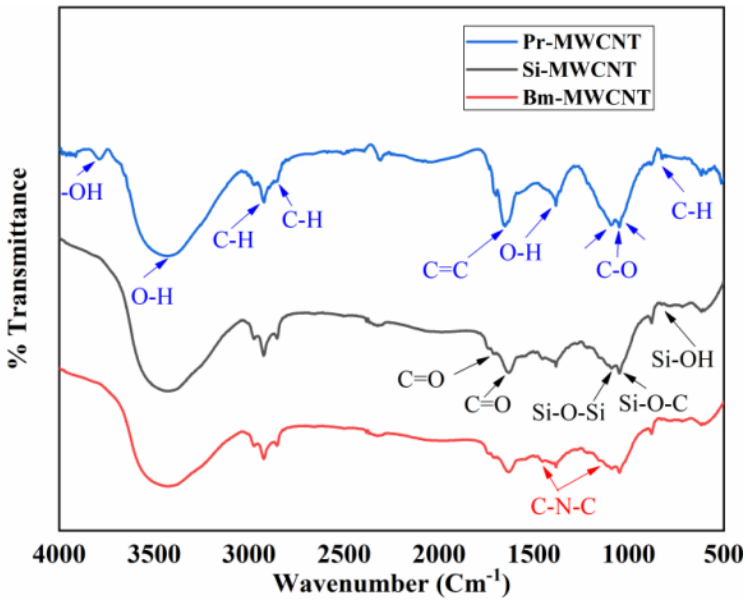

Figure 4.17: FTIR Spectra Analysis of functionalized MWCNTs

After HNO_3 acid wash two new peaks were observed, at 1643 cm^{-1} (C-O) and 1719 cm^{-1} (C=O) attributed to carboxyl and carboxylic group stretching respectively, which are bonded to MWCNT surface after oxidation [132]. Danny Vennerberg et at. [133] reported functionalization of MWCNT. We also noticed similar characteristic peak positions of MWCNTs in our report. Three new characteristic peaks were observed at 1047, 1019, 805 cm^{-1} attributes to asymmetric stretching of (Si-O-Si), deformation stretching of (Si-O-C) and (Si-OH) respectively. This spectrum evidence suggested that acidic groups reacting with amine groups on the surface of oxidised MWCNT results in successful APTS functionalization [134]. After BMI grafting on the silinazed MWCNT, two new bonds observed at 1455, 1147 cm^{-1} associated to C-N-C band of bismalemide moiety justify effective maleimide functionalization on MWCNT surface.

4.5 Conclusions

The Graphene Nano Platelets (GNPs) and Multiwalled Carbon Nanotubes (MWCNTs) agglomeration was addressed through functionalization. First the GNPs and MWCNTs are oxidized with HNO_3 followed by silane layer attachment and bimalemide moiety grafting is known to be functionalization process. Different oxidization times was followed to maximize exfoliation level of GNPs and MWCNTs. Various characterizations like FE-SEM, HR-TEM, XRD, FTIR, TG-DTA, W-G plots was performed to reveal the effective silane and bismaleimide grafting on the surface of GNPs and MWCNTs. The following conclusions are drawn from the current study.

- Amine functionalization is used to address GNPs and MWCNTs aggregation, precise interface management between composite and filler.
- Transverse separation is seen for 60 h oxidation under FESEM along with the lateral exfoliation and the combination of these exfoliations, creates a 3D networked nanofiller structure of GNPs and MWCNTs.
- From HR-TEM data, effective adsorption of several oxygenated groups to the surface of GNPs and MWCNTs during oxidation with nitric acid for at least 60 h was confirmed followed by silanization can lead to successful exfoliation.

- From the XRD data the mean crystalline size of the functionalized GNPs and MWCNTs was found to be 18.8 and 4.17 nm respectively. The EDX data supports the uniform adhesion of silane oligomers (O-H, C=O and COOH) to GNPs and MWCNTs surfaces.
- The DTA curves demonstrate that, for 60 h oxidation, the temperature associated with the maximal degradation rate is higher as a result of the stronger covalent connections between the silane moiety and GNP/MWCNT surface.
- Bismaleimide moiety was used to modify the surface of the silanized GNPs and MWCNTs which acts as both a "dienophile" and a reinforcer in the DA adduct.
- Three new characteristic peaks were observed at 1047, 1019, 805 cm^{-1} attributes to asymmetric stretching of (Si-O-Si), deformation stretching of (Si-O-C) and (Si-OH) respectively confirms the effective silanization.
- The existence of two distinct FTIR peaks with wave numbers of 1140 cm^{-1} and 1450 cm^{-1} confirms the effective C-N-C group of bismaleimide functionalization according to FTIR spectra.
- The X-Ray Diffraction peaks of functionalized GNPs and MWCNTs were well confined with data in JCPDS file No (75-2078) and JCPDS file No (41-1487) respectively indicating a prominent graphitic structure.
- The covalent bond between bismelamide and silane amine functional groups is explained with the help of globular shaped moieties on the surface of functionalized GNPs and MWCNTs which were assumed to be bismalemide moieties.
- It is observed that the rise of oxygen content in bismaleimide nanoparticles is greater than that of silanized, is ascribed to the evidence of grafting of bismeleimide moieties on the surface via covalent bond formation.
- The residual weight loss of bismaleimide grafted nanoparticles is greater than that of silanized and unprocessed, indicating that bismaleimide functionalization was successful, according to TG-DTA.

- The spherically shaped moiety attachment on the surface of silanized GNPs and MWCNTs further confirmed successful bismalemide functional group infusion by FE-SEM and HR-TEM.
- The average particle size and strain of functionalized MWCNTs has been calculated as 3.97 nm and 0.448 respectively from Halder-Wagner plot.
- It was discovered that particle size estimated from Halder-Wagner and Scherrer's approach, which fall within the range of 2-4 nm, has a strong resemblance with the average particle size estimated based on morphological research of FE-SEM, HR-TEM.
- The silane-maleimide functionalized GNP and MWCNT is not only thermally stable and mechanically strong, but it also exhibits self-healing properties due to its dienophile nature.

Chapter 5

Mechanical and fractography analysis of functionalized GNP/MWCNT reinforced polymer and CFRP composites

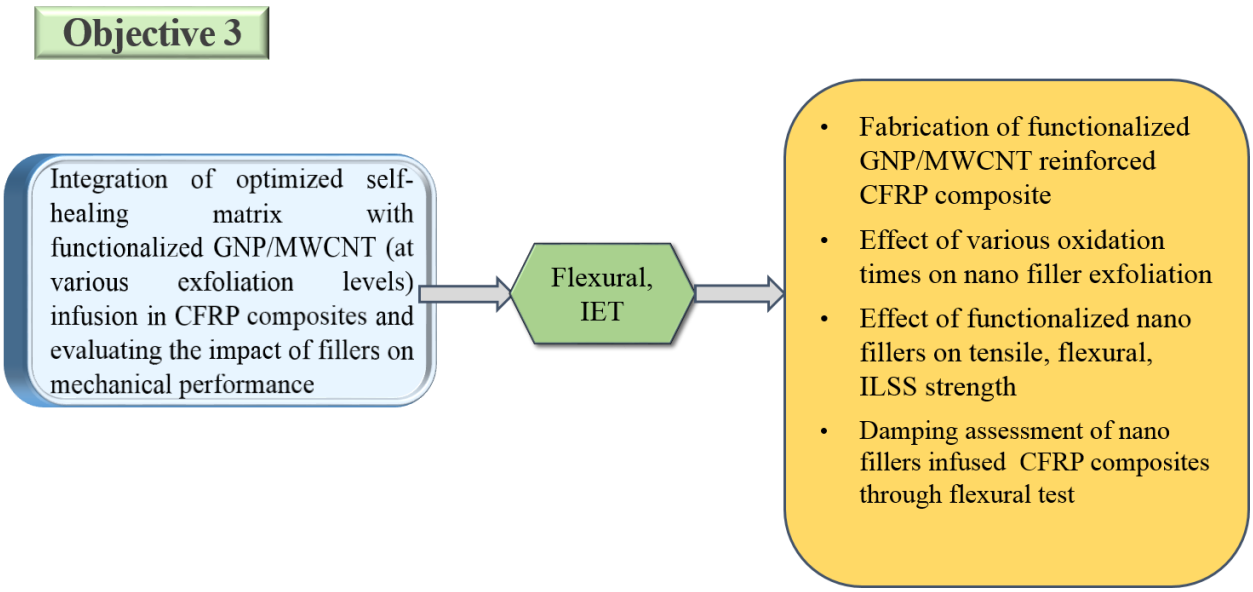

This chapter discusses the effect of functionalized GNP and MWCNT concentration on the mechanical properties (Tensile, Flexural, Inter-laminar shear strength) of carbon fibre reinforced epoxy composite. The fractographic examinations through FE-SEM carried and briefly discussed various failure criterions. Brief discussion on the damping characterization of functionalized GNP and MWCNT reinforced CFRP have been presented.

5.1 Introduction

The interfacial and matrix healing capability have been studied in this for thermally reversible self-healing furan maleimide Diels Alder (FMDA) based hybrid polymer composite. FMDA composite with various weight ratios (0.5, 1.0, and 1.5 wt %.) of bismaleimide infused Graphene Nano Platelets (GNPBm) and Multiwalled Carbon NanoTubes (Bm-MWCNT) was fabricated and characterized. FMDA with varying epoxy, GNPBm/Bm-MWCNT wt.% were considered for mechanical and morphological features. Amine functionalization was used to address GNPs/MWCNTs aggregation, precise interface management.

In evaluating high-performance multiwall carbon nanotube (MWCNT) based carbon fiber composite, effective chemical functionalization of fillers for sufficient exfoliation and precise interface interactions with resin matrix are challenging to attain due to significant interlayer cohesive energy and inactive surfaces of composite. Herein, we demonstrate an effective way to produce CFRP composite with amended interfacial characteristics via the incorporation of MWCNT through oxidation followed by silane functionalization with their various exfoliation levels. These oxidized MWCNTs later underwent amine-based silane moiety functionalization through an APTES silane agent. Topographical examination and spectroscopic studies were conducted to determine the exfoliation degree and functional group adhesion of the resulting functionalized MWCNTs. To assess the impact of functionalization on laminated hybrid CFRP, the amine-modified MWCNTs were initially diffused in a hardener/epoxy matrix using an ultrasonic-mechanical dual stirring process and then hybrid CFRP composite was prepared using a vacuum bagging technique and further assisted in autoclave curing.

5.2 Materials and Methods

Different types of materials used in preparation of bismaleimide grafted functionalized GNPs/MWCNTs infused CFRP composite are discussed in this section along with method of preparation.

5.2.1 Materials

As discussed in chapter 4, 3-Aminopropyl Triethoxysilane-APTES, 4,4-bismaleimide diphenylmethane (BMI/DPMBMI) were used as silane coupling agent and maleimide moiety respectively. Analytical quality solvents like, acetone, toluene, ethanol and Dimethylformamide-DMF were used for extraction. Graphene Nano Platelets and Multiwall Carbon Nanotubes with diameter varying from 2 to 8 nm and length varying from 10 to 20 μm which were used reinforcement in composite preparation. Plain weave unidirectional carbon fiber with 200 GSM and 1.82 g/cc density was used as reinforcing fibers, supplied by Composites Tomorrow India. Table 4.1 specifies the list of materials used in the current study and Table 4.2 specifies the materials key data specifications obtained from standard data sheets. Figure 4.1 shows the chemical architecture of the materials used in the current study.

Table 5.1 List of materials used in the present study

Material	Purpose	Purchased from	Remarks
GNPs	Reinforcement	Nanoshell intelligence Materials Ltd	t- (8-20nm)
MWCNTs	Reinforcement	Nanoshell intelligence Materials Ltd	d- (2-8 nm)
CFRP	Fiber	Composites Tomorrow	----

Material	Image
CFRP	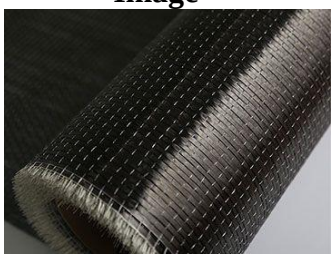

Vacuum pump

Probe Sonicator

GNPs

MWCNTs

Figure 5.1 Representative images of materials used in the study

5.2.2 Fabrication of functionalized GNPs infused self-healing polymer composite

Self-healing polymer composite was developed by compounding irreversible and reversible resins at their stoichiometric proportions, with DGEBA as irreversible and (BMI +FGE + GNPBm) mixture as reversible. Under magnetic stimulation, 12 g BMI (0.027 mol) was diffused in 10.3 g FGE (0.054 mol) at 90 ^{o}C about 5 minutes. With mechanical agitator, 10.01 g DGEBA (35 wt. % in BMI, FGE and DGEBA compound) was added to the resultant solution and cured using MHHPA. The resultant compound was degassed about 45 minutes to pull out trapped air using vacuumed desiccator. The cured polymer composite was coded as 35FMDA.

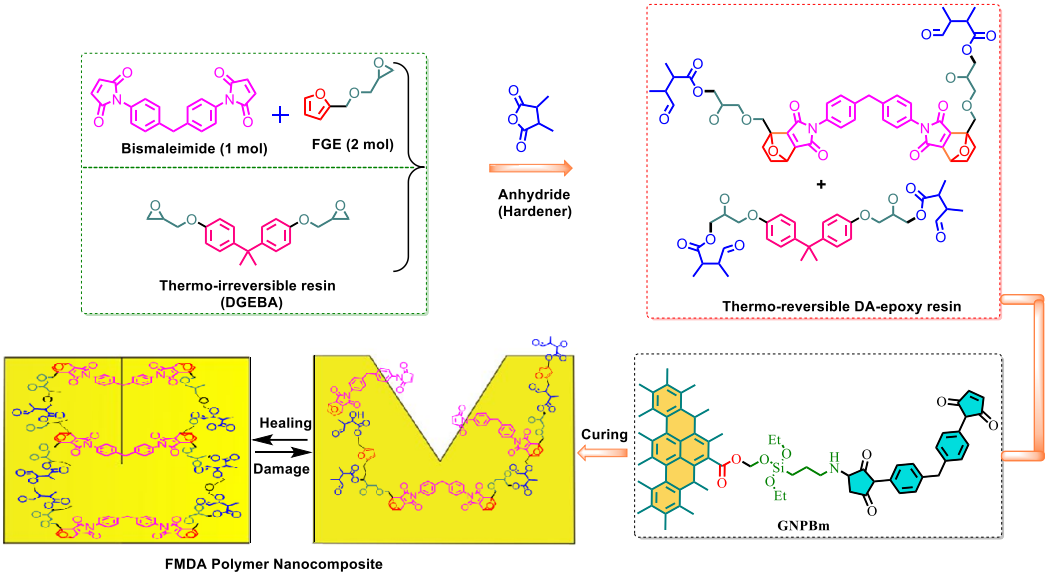

Figure. 5.2. GNPBm infused self-healing sample preparation

Using a similar approach, by fixing FGE and BMI quantities, and varying DGEBA wt %. 45FMDA and 55FMDA were prepared. After selecting the optimum FMDA code as a self-healing matrix, using probe sonicator bismaleimide graphene (GNPBm) in a different weight ranges as 0.5, 1.0, and 1.5 wt. % were reinforced and the interfacial healing capability in polymer composites was evaluated. The developed compound was surged into a silicon mould and cured using autoclave at 85 ^{o}C / 8 h, 130 ^{o}C / 8 h, and 85 ^{o}C / 8 h.

5.2.3 Fabrication of functionalized MWCNTs infused self-healing polymer composite

The self-healing epoxy resin matrix was created by compounding reversible and irreversible matrix at their stoichiometric ratios, with DGEBA resin as the irreversible system and (FGE + DPBMI) compound as the reversible system. Under magnetic stirring, 12g (0.027 mol) of DPBMI was dissolved in 10.3 g of (0.054 mol) of FGE in an oil bath at 90 ^{o}C for 5 minutes at 2:1 molar ratio. Using mechanical agitator, the resultant was mixed with 10.01 g of DGEBA epoxy resin (35 wt. % DGEBA in the combined weight of DGEBA, FGE, and DPBMI) and cured with MHHPA anhydride hardener. The molar ratios of FGE: MHHPA and DGEBA: MHHPA are maintained as 1:0.8 and 1:2 respectively. The Bm-MWCNT/DA-epoxy mixture was subjected to probe sonicator with 30 s intervals for 5 min. The resultant was degassed for 40-50 minutes in a vacuumed desiccator to remove any trapped air.

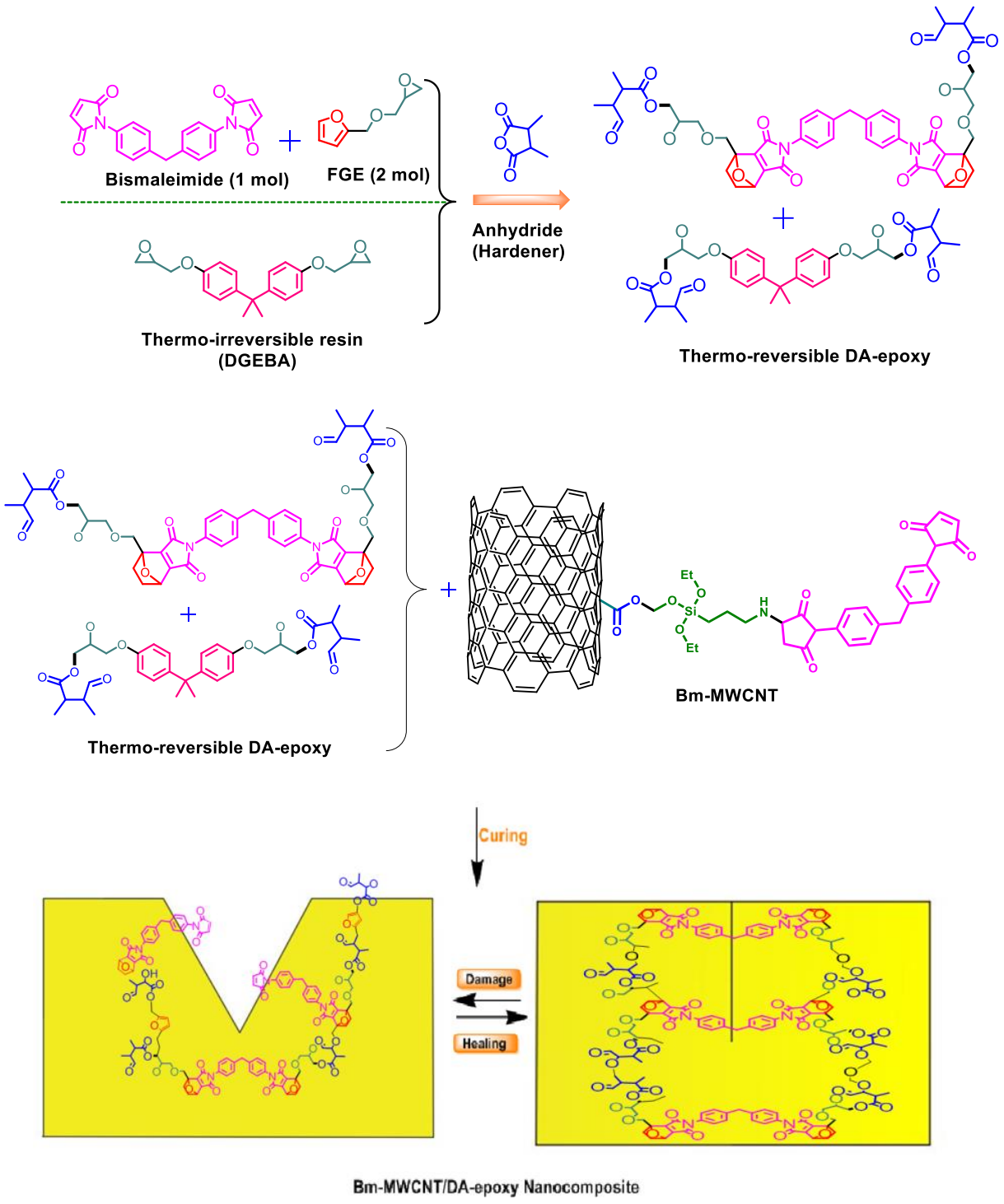

Figure. 5.3. Bm-MWCNT infused self-healing sample preparation

The produced resin was poured into a silicon rubber mould and autoclaved at 85 ^{o}C for 8 hours, followed by 130 ^{o}C for 8 hours, and 85 ^{o}C for 8 hours. The resulting polymer composite as graded as 35DA. Using similar procedure, keep the quantities of BPDMI and FGE as constant and

altering DGEBA wt. % the 45DA and 55DA were made. After choosing the optimum grade as a matrix, the interfacial healing effect in polymer composites was investigated using bismaleimide infused multiwalled carbon nanotubes (Bm-MWCNTs). The DSC experiment has been carried to determine the optimum vol. % composite grade to balance both mechanical properties and self-healing efficiency. According to exo-endothermic peak areas of DSC data, 45DA was chosen as the optimum grade, and Bm-MWCNT nano filler was added in various weight ratios as 0.5, 1.0, and 1.5 wt. % to investigate the interfacial healing capability of Bm-MWCNT/epoxy nano composite.

5.2.4 Fabrication of functionalized MWCNTs infused CFRP composite

Initially, 0.5 wt.% of Pristine MWCNTs about the DGEBA was disseminated in the HY906 (anhydride hardener) via ultrasonic-mechanical dual mixing. The double mixing process was carried out using an ultrasonic probe sonicator with subsequent mechanical stimulation at 600 rpm. The ultra-sonication (with titanium alloy probe) was carried at 69% amplitude for 10 s pulse on and 10 s pulse off time for 30 min. A flowing water chiller bath was used to keep the temperature during the dual mixing process below 50 ^{o}C. After double mixing, DGEBA resin and DY070 accelerator were infused by ensuring a weight mixing ratio of 100:95:2 among DGEBA/HY906/DY070, followed by mixing at 1200 rpm using a high-speed mechanical stirrer. The resultant solution was then degassed to release the trapped air that had been trapped during mixing under a vacuum desiccator for 40 minutes. The mixture was infused into the 8-layer stack of unidirectional carbon fiber mats using the vacuum bagging process. The pristine MWCNT-infused hybrid CFRP composite underwent pre-curing at 110 ^{o}C/2 hr and 150 ^{o}C/8h post-curing using autoclave vacuum pressure at 2 bar and graded as CFRP-Pr(0.5). The preparation of neat CFRP and functionalized MWCNT-infused CFRP with MWCNTs (different oxidation times 0/48/60/72 h) variations used the same procedure mentioned above. Table 5.2 describes the CFRP composite codes and their respective volume fractions.

Table 5.2. Pure and oxidized-silanized MWCNT reinforced CFRP composite with various oxidation times and their respective volume fraction

Composite Type	Oxidation Duration	Nano Filler Oxidation	Nano filler wt.%	Volume Fraction (%)		
				Fiber	Matrix	Nano Filler Content
Pure-CFRP	-	-	-	38.80	61.2	0
CFRP-Pr(0.5)	0	OAC-0	0.5	38.42	61.19	0.384
CFRP-Pr(1.0)	0	OAC-0	1.0	38.27	60.94	0.779
CFRP-Pr(1.5)	0	OAC-0	1.5	38.0	60.76	1.17
CFRP-Si48(0.5)	48/APTS	OAC-48	0.5	38.42	61.19	0.384
CFRP-Si48(1.0)	48/APTS	OAC-48	1.0	38.27	60.94	0.779
CFRP-Si48(1.5)	48/APTS	OAC-48	1.5	38.0	60.76	1.17
CFRP-Si60(0.5)	60/APTS	OAC-60	0.5	38.42	61.19	0.384
CFRP-Si60(1.0)	60/APTS	OAC-60	1.0	38.27	60.94	0.779
CFRP-Si60(1.5)	60/APTS	OAC-60	1.5	38.0	60.76	1.17
CFRP-Si72(0.5)	72/APTS	OAC-72	0.5	38.42	61.19	0.384
CFRP-Si72(1.0)	72/APTS	OAC-72	1.0	38.27	60.94	0.779
CFRP-Si72(1.5)	72/APTS	OAC-72	1.5	38.0	60.76	1.17

5.2.5 Volume fraction of fiber and matrix calculation

The rule of mixture of composites can be used to determine the necessary number of layers to build a laminate with the appropriate thickness. This rule states that the volume of the laminate is the sum of the volumes of each of its component parts.

$$Volume\ fraction\ of\ \ fibre\ (V_f) = \frac{Volume\ of\ \ fibre}{Total\ volume} = \frac{\frac{W_f}{\rho_f}}{\frac{W_f}{\rho_f} + \frac{W_m}{\rho_m}} \qquad \text{Equation 5.1}$$

$$Volume\ fraction\ of\ \ matrix\ (V_m) = \frac{Volume\ of\ \ matrix}{Total\ volume} = \frac{\frac{W_m}{\rho_m}}{\frac{W_f}{\rho_f} + \frac{W_m}{\rho_m}} \qquad \text{Equation 5.2}$$

$$Density\ of\ composite\ (\rho_C) = \rho_f V_f + \rho_m V_m \qquad \text{Equation 5.3}$$

W_f - weight fraction of fiber; W_m - weight fraction of matrix; ρ_f - density of fiber; ρ_m - density of matrix

Mould Dimensions:180×150×3.5 mm^3

Nano fillers wt.%: 0.5, 1.0, 1.5

Weight fraction of fibre (W_f): 0.5

Weight fraction of matrix (W_m): 0.5

Density of fiber (ρ_f): 1.8 g/cc

Density of matrix (ρ_m): 1.16 g/cc

Tensile sample dimensions: 160×15×2.8 mm^3

Short beam shear sample: 15×5×2.8 mm^3

Flexural sample dimensions: 60×12×2.8 mm^3

Weight of composite = $\rho_C \times V_c$=133.07 gm

Weight of matrix = 0.5×133.07= 66.53 gm

Weight of fibre = 66.35 gm

Mass of each carbon layer = 8.3 gm

No of layers required = 66.35/8.3 = 7.99~8

By substituting in above equations, V_f = 0.3842, V_m = 0.61199, V_{filler} ρ_C = 1.4082 g/cc

W_m = 0.5, W_f = 0.5 were considered such that more number of functionalized MWCNTs can be incorporated in the matrix and thus can get better strength and healing efficiencies. According to Hoa S V et al. [135], the highest volume percentage of fibre that may be used in the hand layup technique to obtain the best characteristics is around 40%. The chosen values W_m = 0.5 and W_f = 0.5 are justified because the calculated values were within the range.

5.3 Mechanical performance and damping behavior analysis of functionalized GNPs and MWCNTs infused composite

Various characterization techniques used to investigate the effect of functionalized bismaleimide grafting GNPs/MWCNTs reinforced polymer and CFRP self-healing composite were discussed in this section.

5.3.1 Mechanical Performance evaluation

The mechanical characteristics like tensile (ASTM D 3039, l× w – 160 × 150 mm), flexural (ASTM D 790, l × w – 60 × 12 mm) and short beam shear (S.B.S) (ASTM D2344, l × w – 15 × 5 mm) specimens of plain and functionalized MWCNTs (different oxidation durations along with silanization, bismaleimide) grafted composite materials were investigated using advanced equipment UTM a rate of speed 1 mm/min, 50 kN load cell. Three identical samples were examined for each result, and the average was considered for reporting.

In order to study the mechanical behavior of functionalized MWCNTs reinforced self-healing CFRP composite and neat CFRP composite, three-point bending test was conducted by using advanced equipments AE50kN UTM. The flexural dimensions used were ASTM D 790 and 40 mm span, 50 kN load cell and 1 mm/min speed rate were applied during testing. The impact of the initial damage, the concentration of functionalized MWCNTs, and the healing behavior were assessed based on the flexural strength of the composite. According to Equation 5.4 and 5.5, the flexural strength and strain were determined.

$$Flexural Strength = \frac{3PL}{2bd^2} \text{ MPa} \qquad \text{Equation (5.4)}$$

$$Flexural Strain = \frac{6\delta d}{L^2} \text{ MPa} \qquad \text{Equation (5.5)}$$

P-applied Load in N; L- Span distance in mm; b- width of the specimen; d- thickness of specimen; δ- displacement in mm

The following was used to determine CFRP composite w.o.f. (work of fracture) from a flexural testing. $\text{w.o.f.} = \frac{A}{bh} \text{ kJ/m}^2$ Equation (5.6)

Where b - sample width, h - thickness, and A - expressed in Joules to indicate the work required to deform/rupture the flexural specimen. The w.o.f. is measured in kJ/m^2.

The following Equation (5.7) was used to determine the interlinear shear strength of the resulting hybrid CFRP composites. Where b - the width, h is - the thickness of the S.B.S. sample, and P - is the maximum breaking load.

Short beam shear sample: 15 X 5 X 2.8 mm^3 (ASTM D2344)

$$ILSS = \frac{3P}{4bh} \text{ MPa} \qquad \text{Equation (5.7)}$$

Where, b - width, h - thickness of the SBS sample, and P - the maximum breaking load.

5.3.2 Damping characterization

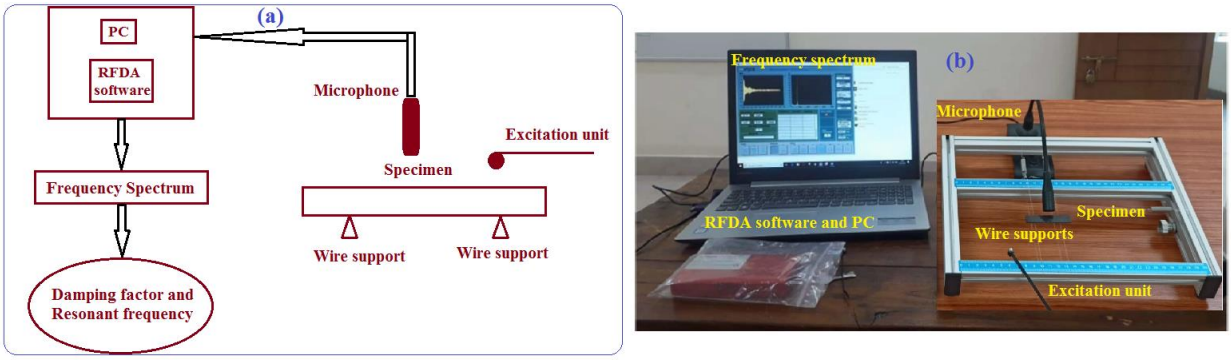

Figure 5.4. Impulse excitation technique (I.E.T.) setup (a) schematic diagram (b) experimental setup

The I.E.T. technique and flexural vibration mode were considered to explore the CFRP composite's damping performance. According to ASTM E 1876, I.E.T. is a nondestructive impulse-based method for determining material dynamic elastic characteristics. The elastic modulus of the specimen is determined using I.E.T. resonant frequency, which also makes it possible to evaluate the specimen damping behavior. Figure 5.4 shows the experimental setup and schematics used in the current study. The following equations can calculate the specimen's dynamic elastic properties and damping factor.

$$\text{Dynamic elastic modulus (E)} = 0.9465 \frac{m f_f^2}{b} \left(\frac{L^3}{t^3}\right) T_1 \qquad \text{Equation (5.8).}$$

For samples with L/t > 20, T_1 can be figured out using Equation (5.9)

$T_1 = \left[1.000 + 6.585\ \left(\frac{t}{L}\right)\right]$ damping factor $(Q^{-1}) = \frac{K}{\pi f_f}$ Equation (5.10).

The relationship between the damping ratio and the damping factor (ζ) can be given by

$(Q^{-1}) = 2\zeta$ Equation (5.11).

5.4 Results and Discussions

5.4.1 Tensile Characteristics

Tensile properties and specimen fracture morphology of bismaleimide functionalized GNPs and MWCNTs infused polymer composite and oxidized and silane functionalized MWCNTs infused CFRP composite laminate were presented.

5.4.1.1 Tensile properties and fracture morphology of functionalized GNP infused self-healing polymer composite

The strength and modulus of 45FMDA (Gr-0.5) were reported as 6.2 MPa and 1675 MPa respectively, which improved to 9.7 MPa and 2771 MPa, respectively, for 45FMDA (Gr-1.0) and further tensile properties decreased to 7.1 MPa and 1820 MPa, respectively, for 45FMDA (Gr-1.5). The uniform dispersion of bismalemide infused GNP nanofillers in polymer epoxy resin under sonication results in improved interaction between polymer matrix and nanofiller attributes to low aggregation, which can transfer load more effectively and is responsible for the improvement of tensile properties of 45FMDA (Gr-1.0).

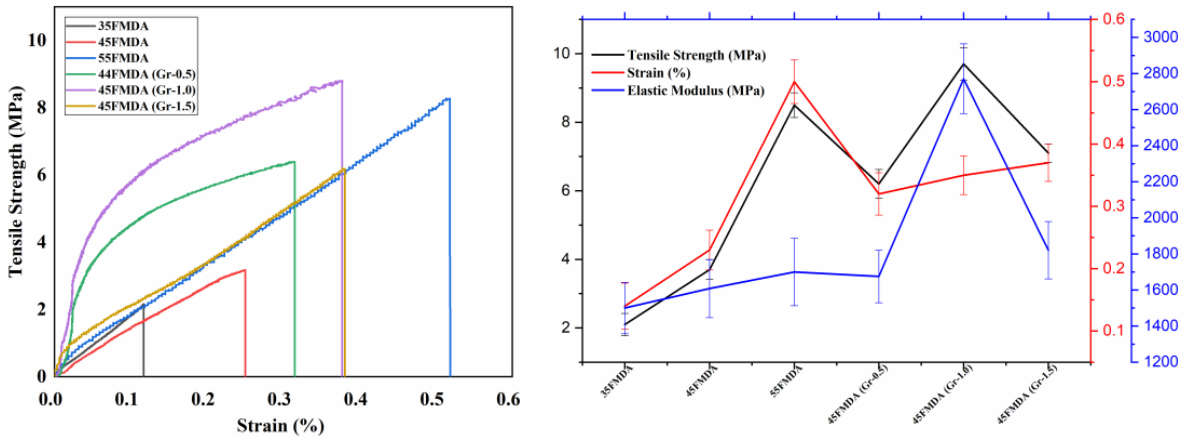

Figure 5.5. Variation of (a) Tensile Strength (a) Tensile Strain (c) Elastic Modulus GNPs in fused self-healing polymer composite

Furthermore, the amine groups treated GNP reacted with BMI resin carbon bonds on the graphene sheet's edge, increasing the bonding strength between nanofillers and polymer epoxy resin. The addition of 1.5 wt.% GNPBm, on the other hand, degraded the polymer composite's tensile characteristics. This problem occurs when a large number of GNPBm nanoparticles are not evenly dispersed in the polymer matrix, causing agglomeration, [136] which reduces the strength and toughness of the material and has a negative impact on mechanical properties.

Table 5.3: Tensile properties and self-healing efficiencies of GNPs infused self-healing polymer composites

Sample Code	Tensile strength (MPa)	% of Strain	Elastic modulus (MPa)
35FMDA	2.1 ± 0.32	0.14 ± 0.037	1500 ± 142
45FMDA	3.7 ± 0.29	0.23 ± 0.032	1608 ± 161
55FMDA	8.5 ± 0.36	0.50 ± 0.035	1700 ± 187
45FMDA (Gr~0.5)	6.2 ± 0.42	0.37 ± 0.034	1675 ± 146
45FMDA (Gr~1.0)	9.7 ± 0.48	0.35 ± 0.031	2771 ± 193
45FMDA (Gr~1.5)	7.1 ± 0.27	0.37 ± 0.030	1820 ± 159

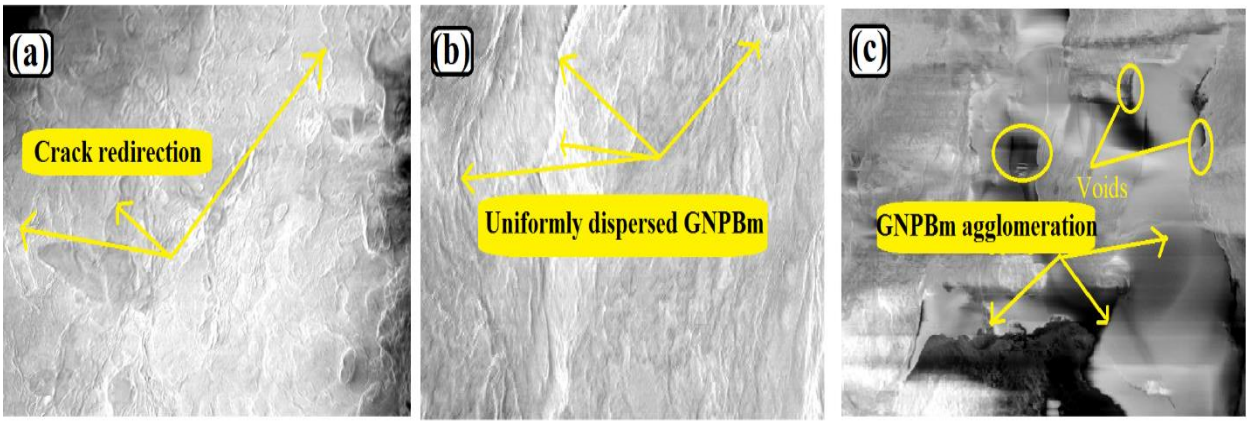

Figure 5.6: Fracture morphology of GNPBm infused Tensile polymer composites

The homogenous distribution pattern of functionalized GNPs on the surface of the composite is shown in Figure 5.6 (a-c). The infused GNPBm nanoparticle inhibited the proliferation of micro-cracks and caused them to by-pass to other routes, as clearly seen from Figure 5.6 (a,b). The path

of the micro-crack changes as it collides with GNPBm nanoparticle, resulting in energy consumption [137]. The increase in roughness caused by severe interfacial interaction of GNPBm and epoxy in Figure 5.6 (b) clearly demonstrates the crack deviation process. Figure 5.6 (c) shows that the GNPBm content of 55FMDA (Gr-1.5) increases aggregation and the creation of pores, resulting in poor mechanical characteristics of the composite. Crack behavior and deviation mechanisms of a furan maleimide based self-healing composite with GNPBm infusion were revealed by fracture surface micrographs.

5.4.1.2 Tensile properties and fracture morphology of functionalized MWCNT infused self-healing polymer composite

Figure 5.7 depicts the influence of filler content on tensile strength in Bm-MWCNT/DA-epoxy composites. The infused Bm-MWCNT significantly increased the tensile strength and elongation for 0.5 wt.% and 1 wt.% filler content as 49.3%, 39.5% and 70%, 33.3% respectively. This is referring to effective interfacial polymer/nano-filler interaction related to the unique hybrid structure between polymer chains and Bm-MWCNT [138]. The reduced tensile strength values for 1.5 wt% Bm-MWCNT/DA-epoxy composites can be explained by the increased carbon nanotube content, which makes the composite brittle and leads to poor mechanical properties. A considerable effect on nanocomposite elasticity has been found by infusing Bm-MWCNT into a DA-epoxy matrix. The increased elasticity seen in the 0.5 wt.% and 1 wt.% Bm-MWCNT/DA-epoxy nanocomposites is most likely due to superior filler dispersion.

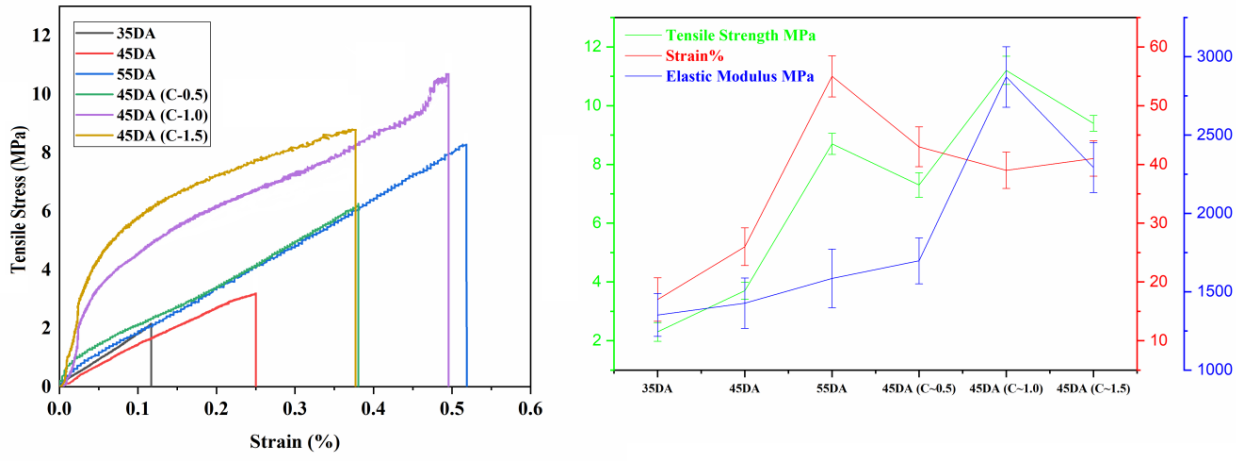

Figure 5.7 Tensile properties of neat and Bm-MWCNT/DA-epoxy infused polymer self-healing composite

Table 5.4: Tensile characteristics of self-healing Bm-MWCNT/ DA-epoxy nanocomposite

Sample Grade	Tensile Strength (MPa)	% Strain	Elastic Modulus (MPa)
35DA	2.3 ± 0.32	0.14 ± 0.037	1352 ± 136
45DA	3.7 ± 0.29	0.25 ± 0.032	1427 ± 161
55DA	8.5 ± 0.36	0.52± 0.035	1585 ± 187
45DA (C~0.5)	7.1 ± 0.42	0.38 ± 0.034	1697 ± 146
45DA (C~1.0)	11.2 ± 0.48	0.49 ± 0.031	2871 ± 193
45DA (C~1.5)	9.4 ± 0.27	0.37 ± 0.030	2292 ± 159

The fracture surfaces of composites containing Bm-MWCNT as shown in Figure 5.8, displayed a considerable rise in the number of river marks and the related surface roughness with increasing MWCNT content. With 0.5 wt.% of Bm-MWCNT, long and straight river stripes were observed parallel to the direction of crack growth shown in Figure 5.8 (a). At 1.0 wt.% these river stripes grew round-ended and shorter [139]. The rising number of river stripes approximately corresponds to the number of isolated, uniformly separated MWCNTs, forcing the cracks to by-pass to other routes. As a result, more energy dissipation through crack bridging and fracture tip bifurcation phenomena. Therefore, Bm-MWCNT reinforced composites attributes to the greater energy requirement to open cracks. However, at about 1.5 wt.% Bm-MWCNT, results in aggregation and the creation of pores occurred. These aggregates can operate as stress raiser, causing internal cracks to propagate in these materials and obstructing load transfer.

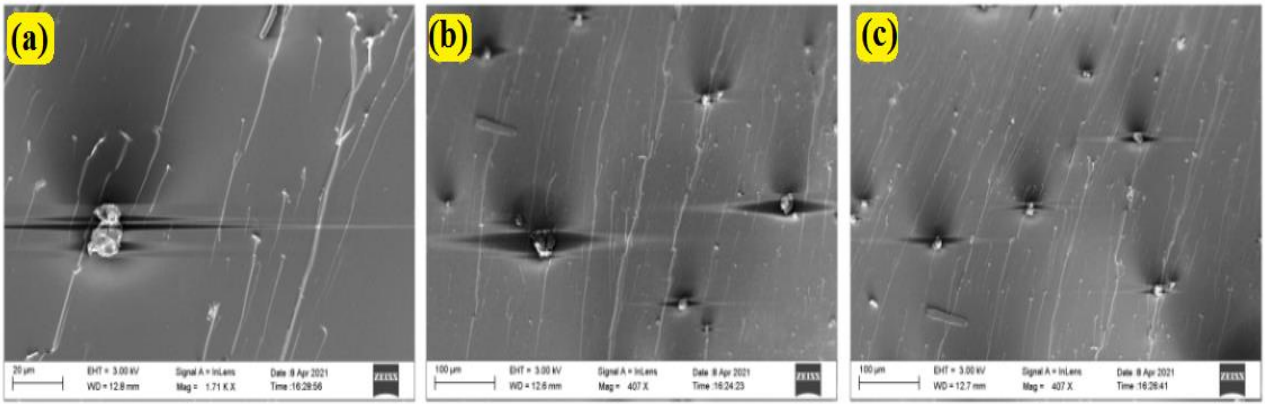

Figure 5.8: Fracture morphology of Bm-MWCNT infused Tensile polymer composites

5.4.1.3 Tensile properties of oxidized-silanized MWCNTs infused CFRP composite

The tensile characteristics of the hybrid CFRP laminates have been assessed, and characteristic change as a factor of oxidization duration, amine surface modification and nanofiller reinforcement quantity are related to pure CFRP. The obtained tensile responses are illustrated in Figure 5.9. The variation in stiffness among matrix, carbon fiber/epoxy matrix interphase, filler/matrix interface, and individual fiber stiffness are the factors responsible for the non-linear response of the stress/strain curve. A large portion of the applied load is initially handled by the matrix with excellent stiffness and minimal distortion, increasing the slope of the curve. Once the micro-nano crack initiation and propagation begin via the fiber/matrix interphase, the composite total stiffness will be reduced due to stiffness variation in the filler/matrix/fiber interphase [140].

The tensile strength (σ_s), Elastic modulus (E) of the pure CFRP were 790 MPa and 15.30 GPa, respectively, after reinforcing with MWCNT-Pr (1.0 wt.%), they were improved to σ_s -1020 MPa and E -25.80 GPa respectively. Fractographic examinations with FE-SEM show extensive Intra/inter-laminar deformation; this was caused by the defect propagation and nucleation at the matrix/fiber junction, which enabled matrix/fiber de-bonding and ultimately resulted in fiber pullout [141]. By reinforcing MWCNT-Pr (1.0 wt.%) into the CFRP, reduced matrix/fiber de-bonding and fiber pullout were observed in Figure 5.9 (d) (due to failure energy absorption at the interlaminar zone) from fractographic investigation compared to pure-CFRP. Still, it is insufficient to prevent the matrix/fiber de-bonding. This is attributed to the matrix cracking with micro crack development caused by the aggregated MWCNT-Pr that ultimately results in matrix/fiber de-bonding, as seen in the FE-SEM micrograph in Figure 5.9 (f). However, the tensile strength and modulus were further increased to 1090 MPa and 26.20 GPa, respectively, for CFRP-Si48(1.0) due to the effective hybridization of matrix/fiber with silanized MWCNT, which can transfer the load uniformly throughout the composite.

For CFRP-Si60(1.0), the tensile properties (σ_s, E) were improved to 1250 MPa and 30.60 GPa, respectively, concerning pure CFRP. This can be attributed to the delamination resistance offered by the matrix/fiber interlaminar junction by forming a significant amount of resin debris both on the sides and surfaces of fibers, shown by the fractographic image Figure 5.9 (e). Furthermore, threads are typically seen hidden by the epoxy resin matrix, emphasizing the limiting of defect

propagation and nucleation at the matrix/fiber junction. This is due to improved grafting of the special OAC-60s among sieves of CFRP interlayer laminates, which led to an effective interfacial connection between matrix/fibers/nano-fillers and improved the bonding strength of the CFRP laminate.

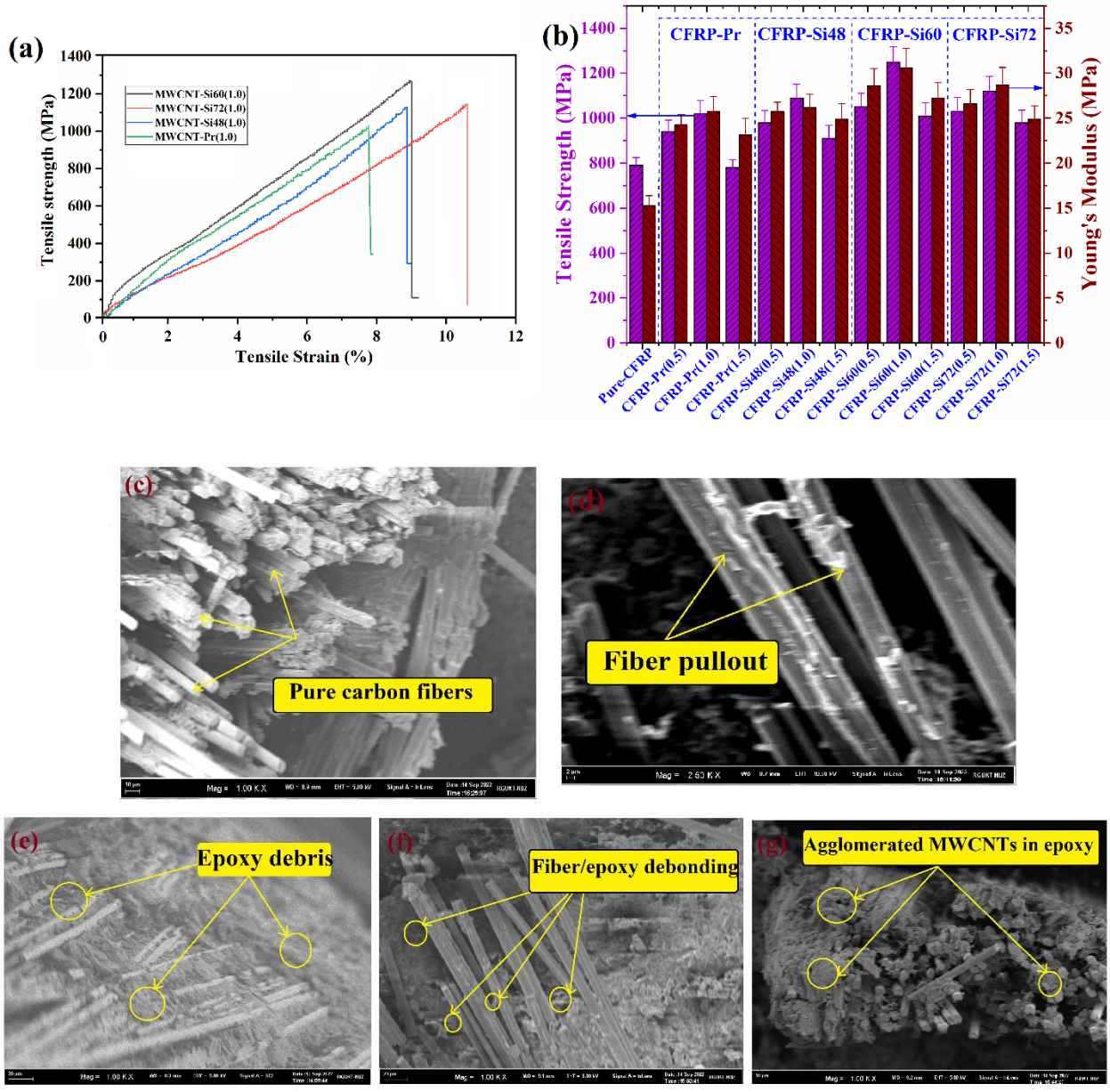

Figure 5.9. (a)Tensile strength variation in CFRP composites (b) Bar graph with tensile strength vs. modulus with oxidizing time and filler content variation. FE-SEM micrographs of tensile fracture surface (c) pure carbon fiber surface (d) Fiber pullout (e) epoxy debris on the surface of composite (f) fiber/epoxy de-bonding (g) agglomerated MWCNT in epoxy

H Sharma et al. [142] prepared carbon fiber reinforced composite with Graphene oxide (GO) nanosheet reinforcement and reported 750 MPa tensile strength, but our work demonstrated much improvement in tensile strength due to MWCNTs functionalization. Furthermore, for CFRP-Si72(1.0), the tensile strength (σ_s) and Elastic modulus (E) was decreased to 1120 MPa and 28.70 GPa concerning CFRP-Si60(1.0). From the CFRP-Si72(1.0) FE-SEM micrographs, fiber pullout and matrix cracking were observed due to transverse agglomeration of MWCNTs and inadequate interfacial contact between the matrix/fibers Figure 5.9 (g). In addition to the preceding, when the filler percentage was increased beyond 1.5 wt.%, all the hybridized CFRP versions had decreased tensile characteristics due to agglomerated MWCNT. The surface morphology of CFRP-Si72 with excessive filler content exhibits bare fiber surfaces, minimal debris, weakly integrated bulk resin matrix/fibers, and aggregated MWCNTs. Even after silanization and probe sonication, the viscosity increase in epoxy increases the stress-raising impact in the interlaminar zone, resulting in diminished tensile characteristics. From the data, CFRP-Si60(1.0) exhibited superlative tensile properties than other composites.

5.4.2 Flexural analysis of functionalized MWCNTs infused CFRP composite

A three-point bend test has been carried out to examine the out-of-plane characteristics of the hybrid CFRP relative to pure bending conditions. The covalent bonds that form between the polymer and MWCNT provide more significant interfacial interaction and total exfoliation, significantly amplifying their impact on the characteristics of the composite. It is generally known that the interface between polymer matrix/fiber, depth stress gradient, and intrinsic stiffness significantly influences flexural characteristics. The variance in flexural graphs is shown in Figure 5.10 (a-d). The flexural strength, flexural modulus, and work of rupture for the neat and CFRP-Pr(1.0) are 720 MPa, 48.10 GPa, 34.23 KJ/m^2 and 903 MPa, 59.45 GPa, 44.62 KJ/m^2 respectively.

These values have increased greatly by 41.1 %, 37.6 % and 37.7 %, respectively, for CFRP-Si48 and 73.8 %, 54.4 % and 53.8 %, respectively, for CFRP-Si60 about pure-CFRP. Sanchez et al. [143] demonstrated the impact of CNT on CFRP flexural strength, and instead, our work highlights how OAC-60 has a distinctive advantage in improving flexural properties.

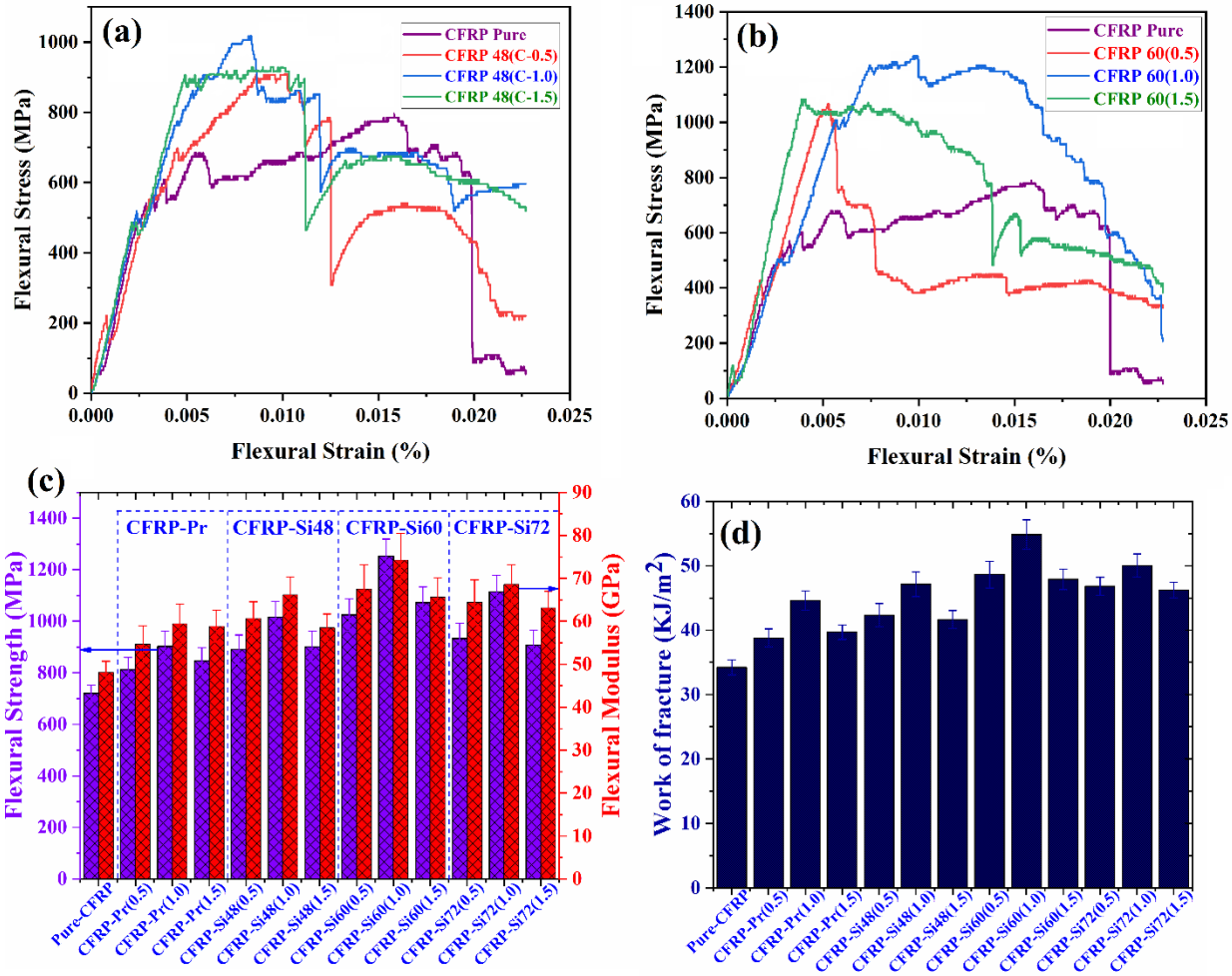

Figure 5.10. (a-b) MWCNT reinforced CFRP composite, variation in flexural strength. Bar graphs (c) Flexural strength and flexural modulus (d) Work of fracture (K.J./m^2)

Furthermore, a small decrease in properties was observed for CFRP-Si72 when compared to CFRP-Si60. From the above, it was evident that the difficulty of distributing nanofillers into polymeric matrix often poses a significant barrier to using high concentrations. Due to their inherent propensity to aggregate, MWCNTs. have a viable mixing weight percent of less than 1.5 wt. %. According to the flexural graph, the matrix containing OAC-60 can enhance the composite load-bearing capacity and minimize deformation at the matrix/fiber interface. As a result, the biggest improvement in flexural characteristics for CFRP-Si60 provides validation that the 60 h oxidation time followed by silanization enhances the uniform dispersion throughout carbon fibers and improves CFRP stiffness due to the hydrophobic nature of silane moieties.

5.4.3 ILSS of functionalized MWCNTs infused CFRP composite

Interlaminar shear strength (ILSS) of the hybrid CFRP was further evaluated using the three-point short beam strength (S.B.S.) test to understand the impact of silanized MWCNTs on the delamination criteria. Shear stress in the S.B.S. test causes interlaminar shearing cracks when it reaches the threshold at mid-thickness. The abrupt decrease in peak load can be used to estimate this maximal shear stress. However, because of the unidirectional FRP's inadequate load-bearing capacity in the transverse direction, intense compressive stress concentration at the loading point might cause fiber breakage and resin micro-cracking.

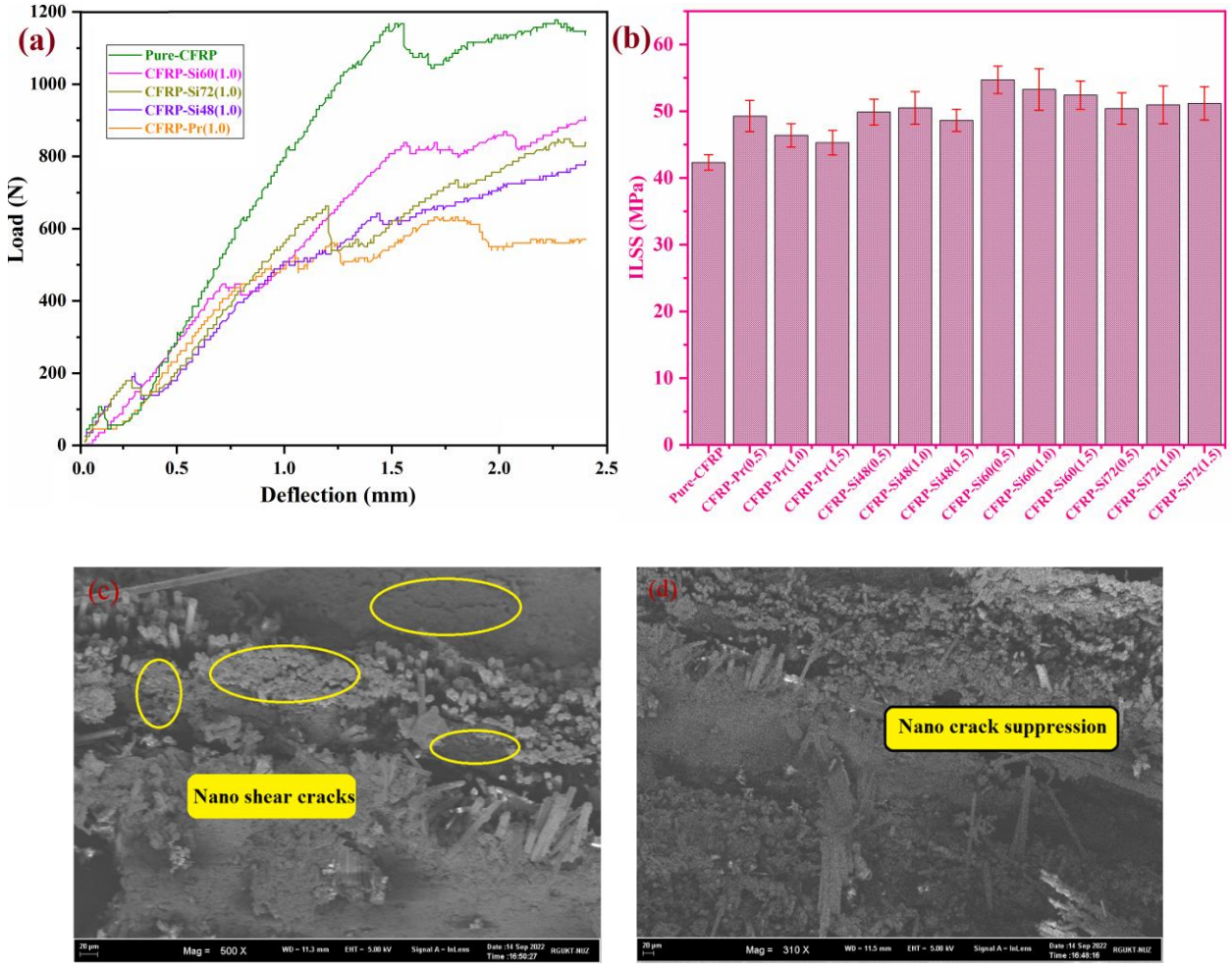

Figure 5.11. (a) S.B.S. sample load vs. displacement curves of pure and functionalized MWCNTs (1 wt.%) (b) Bar graph of interlaminar shear stress with varied filler content (c,d) Fracture morphology of S.B.S sample

We examined the load-deformation curves better to comprehend the ILSS failure behavior of hybrid CFRP. Figure 5.11 depicts the difference in the load-deformation angle of the combination CFRP; at least three test samples were used for each. The ILSS graph exhibits a mixed mode of fracture due to repetitive rise and fall in load, predominantly caused by matrix/fiber cracking due to weak transverse load capacity [144]. On the other hand, all the hybrid CFRP curves exhibit a rapid load reduction, followed by a slow decline, which is a sign of the interlaminar mode of shear failure. This behavior demonstrates the benefit of every MWCNT type on crack inhibition in a transverse orientation [145]. The ILSS is therefore calculated based on the maximum load of the graphs and illustrated in Figure 5.11 (a, b); the values are reported in Table 5.5.

The ILSS of the pure CFRP was 42.32 MPa, which is enhanced by 14.29% (48.37 MPa) for CFRP-Pr(1.0). The CFRP-Pr may have been unable to infuse due to large-scale aggregation since they remained clustered at the lamina interlayers. Furthermore, the ILSS of CFRP-Si48(1.0) and Si60(1.0) was shown a significant improvement by 19.30% (50.49 MPa) and 28.18% (54.29 MPa), respectively. The ILSS strength, however, exhibits a decreasing trend due to a high silanization time of 72 hours and a high filler content (1.5 wt.%). The minor or lack of ILSS deterioration for the CFRP with OAC-60 and OAC-72 at a larger reinforcement ratio is due to the lower stress-raising impact produced by silanization in the intra-laminar region. Pathak et al. [146] revealed that 0.3 weight percent of G.O. mixed with epoxy matrix increased the CFRP ILSS by about 23%. Our result thus exhibits a significantly better enhancement in ILSS strength than previously reviewed literature, which justifies a stronger interlaminar shear resistance. It is evident from the fractographic images of the cracked pure ILSS sample that there are numerous interlaminar shear cracks near the intense load and at the mid span. It is interesting to note that the macrographs of CFRP-Si60(1.0) show only interlaminar shear fissures towards the mid span, confirming the suppression of transverse damage Figure 5.11 (c, d). At the matrix/fibers intersection, we anticipate networks of distinct OAC-60 that responsibly increase the shear resilience by stiffness modification caused by the amine-based silane oligomers. The reinforced MWCNTSi (silane oligomers) positively impact the epoxy surface energy via H-bonding and improve wetting by strengthening their chemical functional group interaction with the fiber surface.

Table 5.5. Mechanical properties of oxidation followed by silane functionalized MWCNT reinforced CFRP composites

Sample Grade	Tensile Strength (MPa)	Tensile Strain (%)	Tensile Modulus (GPa)	Flexural Strength (MPa)	Flexural Modulus (GPa)	Work of Fracture (K.J./m^2)	ILSS (MPa)
Pure-CFRP	790 ± 35	10.15 ± 0.67	15.30 ± 1.07	720 ± 32	48.10 ± 2.60	34.23 ± 1.20	42.32 ± 1.15
CFRP-Pr(0.5)	940 ± 51	8.31 ± 0.69	24.27 ± 1.14	812 ± 47	54.66 ± 4.30	38.79 ± 1.40	46.27 ± 2.33
CFRP-Pr(1.0)	1020 ± 59	9.21 ± 0.85	25.80 ± 1.63	903 ± 58	59.45 ± 4.60	44.62 ± 1.50	48.37 ± 1.76
CFRP-Pr(1.5)	780 ± 49	8.05 ± 0.74	23.15 ± 1.82	846 ± 52	58.86 ± 3.70	39.69 ± 1.10	45.29 ± 1.85
CFRP-Si48(0.5)	980 ± 55	7.25 ± 0.52	25.74 ± 1.02	891 ± 56	60.66 ± 3.90	42.35 ± 1.80	49.87 ± 1.93
CFRP-Si48(1.0)	1090 ± 60	7.98 ± 0.67	26.20 ± 1.48	1016 ± 61	66.19 ± 4.10	47.14 ± 1.90	50.49 ± 2.45
CFRP-Si48(1.5)	910 ± 57	9.95 ± 0.89	24.89 ± 1.72	902 ± 59	58.48 ± 3.20	41.66 ± 1.40	48.62 ± 1.66
CFRP-Si60(0.5)	1050 ± 61	9.82 ± 0.91	28.63 ± 1.89	1025 ± 62	67.55 ± 5.60	48.64 ± 2.10	53.70 ± 2.05
CFRP-Si60(1.0)	1250 ± 68	11.16 ± 1.03	30.60 ± 2.15	1252 ± 67	74.27 ± 6.20	54.85 ± 2.30	54.25 ± 3.11
CFRP-Si60(1.5)	1010 ± 59	8.04 ± 0.75	27.24 ± 1.73	1072 ± 61	65.65 ± 4.50	47.91 ± 1.60	52.40 ± 2.10
CFRP-Si72(0.5)	1030 ± 63	7.68 ± 0.58	26.61 ± 1.57	933 ± 60	64.45 ± 5.20	46.82 ± 1.40	50.41 ± 2.35
CFRP-Si72(1.0)	1120 ± 65	9.34 ± 0.80	28.70 ± 1.95	1114 ± 64	68.61 ± 4.60	50.05 ± 1.80	51.94 ± 2.84
CFRP-Si72(1.5)	980 ± 56	6.82 ± 0.63	24.90 ± 1.48	908 ± 58	63.10 ± 3.90	46.24 ± 1.20	50.15 ± 2.50

5.4.4 Damping behavior of functionalized MWCNTs infused CFRP composite

Figure 5.12 shows the vibration signals and corresponding frequency spectra of CFRP-Si60-(0.5, 1.0, 1.5) samples. The findings reveal that the resonance frequency of CFRP was increased with silanized MWCNT reinforcement. This can be associated with reducing the specimen's vibrational response by an increase in the dissipation of vibration energy throughout the structure [147]. The resonant frequency of pure CFRP was lower than silanized MWCNT-infused CFRP can be attributed to a reduction in vibrational energy absorption. Equations (5.3) and (5.5) were used to calculate the CFRP's elastic modulus and damping factor using their respective frequency domain data. The damping factor of CFRP-Si is illustrated in Figure 5.12 (b-d). The findings demonstrate that the inclusion of silanized MWCNTs increases the damping factor of CFRP composite. A noticeable improvement in the damping factor was observed for CFRP-Si60(1.0) because of adequate crack energy, which improves the composite's energy absorption capability. In addition to MWCNT-Si wt.%, the viscoelastic properties of the epoxy resin and the interfacial connection between the matrix and the MWCNT-Si also affect the damping factor. In general, flaws such as micro voids, dislocations, and different interfaces spread during vibrations or are vulnerable to slippage, which promotes to dissipation of vibration energy. The lower damping factor of pure

CFRP, compared to MWCNT reinforced, can be attributed to CFRPs natural frequency because it is more significant than pure CFRPs natural frequency.

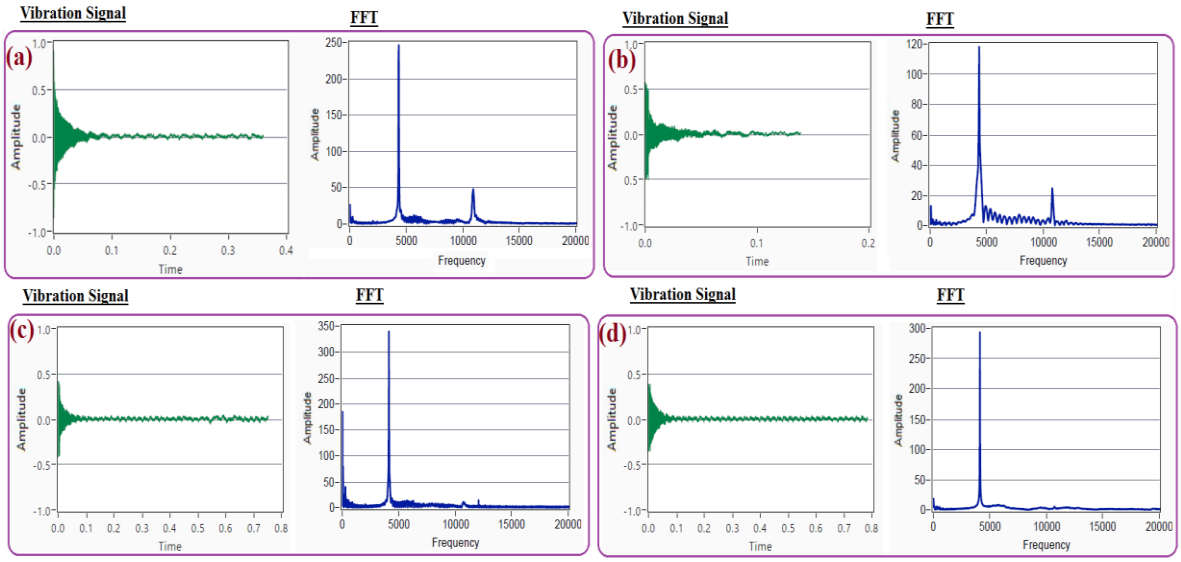

Figure 5.12. Frequency domain and time domain spectrums of (a) pure and (b-d) functionalized MWCNT (1 wt.%) reinforced CFRP composites

Table 5.6. Damping factor and elastic modulus of pure and functionalized MWCNT infused CFRP composite through flexural and I.E.T. test.

Composite type	Resonant frequency (Hz)	Damping factor	Elastic modulus (GPa)	
			Through I.E.T.	Through Flexural
Pure-CFRP	4348.15	0.0029	47.52 ± 2.15	48.10 ± 2.60
CFRP-Si48(1.0)	4252.17	0.01324	64.82 ± 3.74	66.19 ± 4.10
CFRP-Si60(1.0)	4150.98	0.0614	72.55 ± 5.01	74.27 ± 6.20
CFRP-Si72(1.0)	4128.79	0.01532	64.59 ± 3.95	68.61 ± 4.60

5.5 Conclusions

The bismaliemide functionalized GNPs and MWCNTs were reinforced with various ratios as 0.5, 1.0 and 1.5 wt.% in the self-healing polymer nanocomposite. The tensile properties and fracture morphology of self-healing polymer nanocomposite were evaluated and the optimum wt.% of reinforcement was determined. Herein, we demonstrate an effective way to produce CFRP

composite with amended interfacial characteristics via the incorporation of MWCNT through oxidation followed by silane functionalization with their exfoliation levels (0/48/60/72h). The surface functional elements, morphological changes, elemental groups, quantitative information, and thermal degradation of silane functionalized MWCNTs were characterized by FTIR, FESEM/HR-TEM, XRD, and TG-DTA analysis, respectively. The following conclusions are drawn from the current study.

- The homogeneous dispersion pattern of GNPBm was discovered with 0.5 and 1.0 wt. % reinforcement in FMDA polymer composite. With 1.5 wt % GNPBm, there was little aggregation and porosity development was observed, leading to poor mechanical properties.
- FESEM morphological images of 45FMDA (Gr-1.0) demonstrate superior dispersion quality and toughing mechanisms, as GNPBm arrests crack propagation and provides crack diversion.
- The roughness caused by the GNPBm and epoxy's interfacial contact, which clearly suggests a crack deviation mechanism, leads to energy consumption. 45FMDA (Gr1.0) had the highest tensile strength and optimum healing percentage of 9.7 MPa and 90 % respectively.
- 45DA (C-1.0) nanocomposite exhibits maximum tensile strength, elastic modulus and optimal healing percentage of 11.2 MPa, 2871 MPa and 89% respectively.
- The bismaleimide grafted GNP and MWCNT reinforced nanocomposite is both thermally stable and mechanically strong.
- We have fabricated and characterized a hybrid CFRP composite with exfoliated MWCNTs through various oxidation times followed by amine functionalization as reinforcement.
- The influence of oxidation level followed by amine-based silane functionalized MWCNTs (various wt.%) on the mechanical properties (tensile, flexural and ILSS) and damping behavior through I.E.T. was evaluated.
- It was observed that the oxidation level significantly affected the de-aggregation of MWCNTs. The FE-SEM and HR-TEM analysis showed that the aggregated MWCNTs experienced sufficient transverse and lateral exfoliation over 60 hours of oxidation (OAC-60) and created a 2D networked nanotube structure.

- The FTIR, and XRD confirm that the hydroxylic, carbocylic and carbonyl functional elements in OAC-60 justify the effective silane moiety grafting on the MWCNTs surface, which promotes uniform dispersion.
- With the incorporation of 1 wt.% OAC-60 in CFRP laminates, using sonication and vacuum bagging, significant improvement in tensile strength (1250 MPa) and modulus (30.60 GPa) about pure-CFRP was observed.
- The improved flexural strength (1252 MPa), modulus (74.27 GPa) and w.o.f. (54.85 GPa) with regard to pure CFRP was observed for CFRP-Si60(1.0) because of the high stiffness, load bearing capability of the composite, which resulted in less deformation at the fiber/matrix/filer interface.
- The interlaminar shear response of CFRP-Si60(1.0) composite exhibited transverse damage inhibition because of high shear resistance induced by the hydrophobic nature of silane moieties.
- The resonant frequency of CFRP-Si60(1.0) improved resulted in high damping factor because of increased vibrational energy absorption throughout the composite.
- Thus, this study provides a comprehensive analysis of the OAC-60 exfoliation and potential usage by industries as a nanofiller reinforcement to regulate the stiffness at the fiber/matrix interface of CFRPs in high-performance applications.

Chapter 6

Self-healing performance and damping behavior of functionalized GNP and MWCNT reinforced CFRP composite

Objective 4

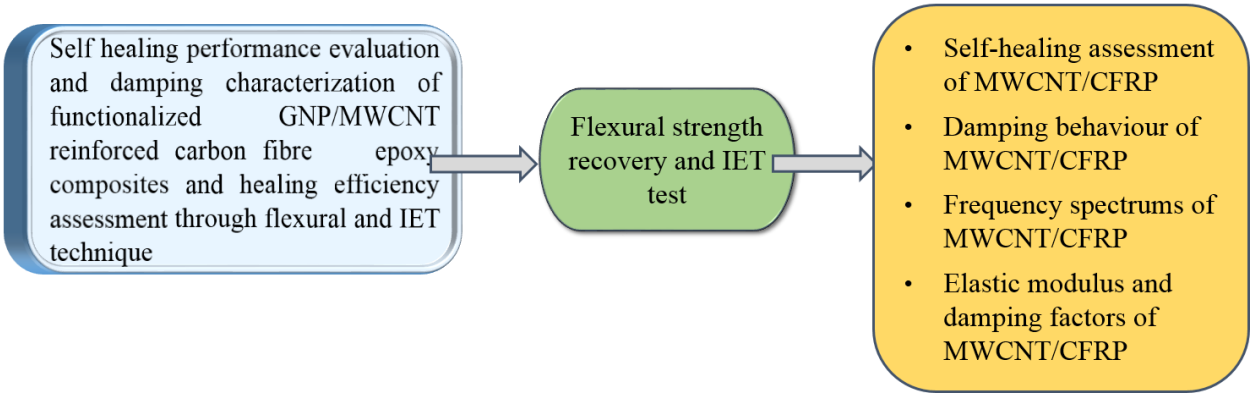

This chapter discusses the effect of functionalized GNP and MWCNT concentration on the flexural strength recovery and self-healing efficiency of carbon fibre reinforced epoxy composite. Brief discussion on the damping characterization of self-healing CFRP composite have been presented and CFRP composite healing efficiency was compared through flexural and IET technique.

6.1 Introduction

Thermally reversible Diels-Alder based self-healing resin along with nano-filler infusion, has to be integrated with the CFRP composite to gain the advantage of high mechanical properties as well as high healing efficiency. At the CFRP interface, strong bonds between both the matrix and carbon fibers are required for an effective shearing mechanism that transfers under loading, which usually depends on adhesion among matrix/fiber/filler [148]. As a result, one of the most significant issues for researchers has been to improve the interface behavior of CFRPs. Due to their exceptional thermal, mechanical, and electrical qualities, graphene nanoplatelets (GNPs) and multiwalled carbon nanotubes (MWCNTs), grafting is the most significant and ideal option for innovation on the next creation of high-performance self-healing CFRP composites [149]. MWCNTs play a mostly dominant role in modern structural applications due to their distinctive mechanical characteristics, which include stiffness, strength, and toughness as well as a high chemical affinity towards chemical functional groups, which further modifies the MWCNT's surface. Additionally, even a slight change in the surroundings and the aggregation of the nanoparticles on the fiber surface might negatively impact the outcomes. In light of this, it has been demonstrated that chemical functionalization of nanofillers (via covalent attachment of compatibilizing functional groups) can enhance the filler uniformity and mechanical performance of nanocomposites, even when filler loadings are quite high [150].

In this research, the interfacial behavior of a self-healing CFRP composite with silane-maleimide functionalized MWCNTs grafting on carbon fiber surfaces was examined. In schemes 5.1 and 5.2, the self-healing composite preparation is illustrated. DPBMI 4,4′-methylenebis (N-phenylmaleimide), DGEBA (epoxy resin), curing agent HY 906 (hardener), FGE-furfuryl glycidyl ether were utilized to synthesize self-healing (thermo-reversible) resin. In order to enhance the interfacial bonding between matrix and fiber in CFRPs, the carbon fiber surface has been grafted using silane coupling fallowed by maleimide grafted functionalized MWCNTs. As previously said, numerous studies have been done on the improvement of the mechanical characteristics of CFRPs

using techniques like grafting, sizing, and thermal treatment however, very few studies on the subject of modifying the matrix of CFRPs in order to strengthen the mechanical properties of the composite and improve the interface. By adding maleimide grafted MWCNT to the composite matrix, this research intends to enhance the mechanical characteristics of CFRPs, such as flexural, tensile, as well as their TGA thermal properties, and further promote interfacial healing abilities. Therefore, the current study focuses on creating MWCNTBm-reinforced carbon fiber CFRP composites and evaluating their capacity for self-healing (by varied wt.% of reinforcement). The impact of initial damage and nanoparticle content on composite flexural strength is also examined. The main objective of this paper is to investigate matrix/fiber/nanofillers interface junction healing properties of the CFRP composite before and after damage. Furthermore, it is intended to re-form structural stability over the CFRP interface junction of the damaged area and also examine the mean healing efficiency.

6.2 Materials and Methods

This chapter discusses functionalized MWCNTs nanofiller impact on tensile strength, flexural strength before and after healing, self-healing efficiency damping behavior of self-healing CFRP composite.

6.2.1 Materials

As discussed in chapter 4 and 5, functionalized MWCNTs were used as reinforcement and healing agent in self-healing CFRP composite. 3-Aminopropyl Triethoxysilane-APTES, 4,4-bismaleimide diphenylmethane (BMI/DPMBMI) were used to functionalize MWCNTs. Multiwall Carbon Nanotubes with diameter varying from 2 to 8 nm and length varying from 10 to 20 μm which were used as nanofillers in epoxy. All of the compounds were analytical grade and did not require any further refining. Plain weave unidirectional carbon fiber with 200 GSM and 1.82 g/cc density was used as reinforcing fibers, supplied by Composites Tomorrow India.

6.2.2 Fabrication of functionalized MWCNTs infused self-healing CFRP composite

Thermally reversible DA based self-healing resin must have balance reversible bonds (promotes healing) and irreversible bonds (retains strength). In order to balance both, stoichiometric ratio of

synthesize FGE, hardener and DGEBA epoxy resin is important. We have prepared three different stoichiometric self-healing resin ratios and based on the number of reversible and irreversible bonds generated (through differential scanning calorimetry analysis), the optimum ratio was selected and reinforced various wt.% of functionalized MWCNTs and finally integrated with the carbon fibers. Initially, 0.5 wt.% of MWCNTBm in relation to the epoxy resin was disseminated in the HY906 hardener by using an ultrasonic-mechanical dual mixing process.

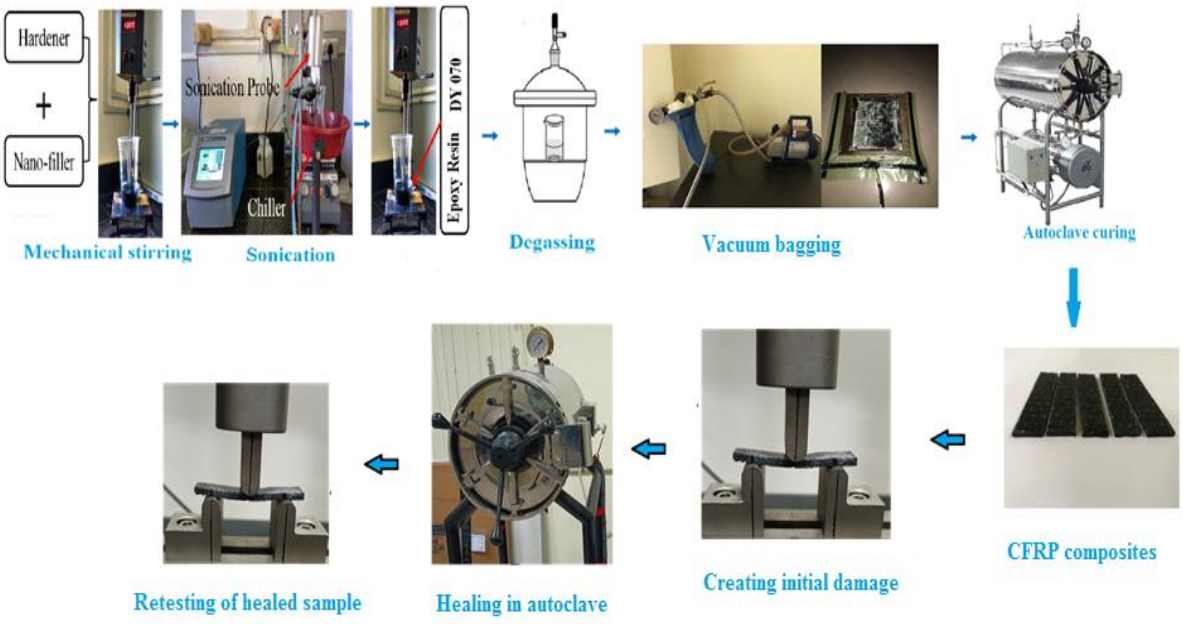

Figure 6.1. Experimental procedure of self-healing hybrid CFRP composite preparation

The dual mixing process was carried out using an ultrasonic probe sonicator with simultaneous mechanical stimulation at 600 rpm. The ultrasonication fitted with a titanium alloy probe was carried at 69% amplitude for 10 s pulse on and 10 s pulse off time for 30 min. A flowing water chiller bath was used to keep the temperature during the dual mixing process below 50 ^{o}C. After dual mixing processing, 10.3 g of FGE (0.054 mol) and 12 g of DPBMI (0.027 mol) were added through stirring at 90 ^{o}C for 5 min. Using a high-speed mechanical stirrer, epoxy-LY556 resin was added by ensuring 35, 45 and 55 wt.% in the compound of FGE+DPBMI+LY556 at 1250 rpm. The resultant solution was then degassed under a vacuum for 40 minutes. Using the vacuum bagging process, the mixture was infused into the 8-layer stack of unidirectional carbon fiber mats. The MWCNTBm infused hybrid CFRP composite underwent a curing cycle of 8 h/85

^{o}C, 8 h/130 ^{o}C, 8 h/85 ^{o}C at a 2 bar vacuum pressure condition using autoclave and graded as CFRP-45 wt.% (C-0.5). The preparation of neat and MWCNTBm infused self-healing CFRP used the same procedure as mentioned above. Table 6.1 includes a description of the self-healing CFRP composite sample codes.

Table 6.1. Description of composite types with their respective volume fraction

Composite type	wt.% of DGEBA	Volume fraction (%)			Weight Fraction of matrix in each sample (gms)
		Fiber	Matrix	Nano filler	
CFRP-35	35	48.30	51.1	0	(11g BMI + 9.4g FGE + 10.9g Epoxy + 19.8g MHHPA)
CFRP-45	45	38.30	61.2	0	(11g BMI + 9.4g FGE + 16.7g Epoxy + 24.1g MHHPA)
CFRP-55	55	22.60	77.5	0	(11g BMI + 9.4g FGE + 24.9g Epoxy + 32.2g MHHPA)
CFRP-45 (C-0.5)	45	38.42	61.19	0.384	(11g BMI + 9.4g FGE + 16.7g Epoxy + 24.1g MHHPA)
CFRP-45 (C-1.0)	45	38.27	60.94	0.779	(11g BMI + 9.4g FGE + 16.7g Epoxy + 24.1g MHHPA)
CFRP-45 (C-1.5)	45	38.07	60.76	1.17	(11g BMI + 9.4g FGE + 16.7g Epoxy + 24.1g MHHPA)

6.3 Mechanical, self-healing performance and damping behavior analysis of self-healing CFRP composite

This section deals with the mechanical test used to assess the effect of functionalized MWCNTs concentration on the flexural strength recovery after fracture and self-healing performance of CFRP composite. The techniques used to evaluate the damping behavior self-healing CFRP composites are discussed.

6.3.1 Mechanical performance evaluation

Three-point bending tests using an AE50kN UTM were conducted in order to compare the mechanical performance of neat CFRP composite with functionalized MWCNT reinforced CFRP composite. During testing, flexural dimensions of 60 X 12 X 2.8 mm^3 and 40 mm span were used. A 50 kN load cell and a 1 mm/min speed rate were also used. On the flexural strength of the composite, the impact of the original damages, the concentration of functionalized MWCNTs, and

the healing circumstances were assessed. Three identical samples were examined for each outcome, and the average was taken into account for reporting.

6.3.2 Assessment of self-healing performance

This section discusses the qualitative and quantitative techniques used to examine the epoxy system's self-healing capability.

6.3.2.1 Qualitative self-healing performance assessment

Utilizing a Huvitz 3D optical microscope, a qualitative investigation of the composite specimen with functionalized MWCNTs incorporated was made. By tapping with a sterile surgical blade, an artificial pre crack was generated in order to analyse the specimen's self-healing behavior. In this condition, the broken surfaces were kept at 85^{o}C/2h and 130^{o}C/2h in autoclave to perform Diels-A and retro Diels-Alder respectively.

6.3.2.2 Quantitative self-healing performance assessment

TDCB specimens reinforced with functionalized MWCNTs were manufactured and tested for fracture toughness in accordance with the method described by White et al. [1] in order to evaluate the self-healing capabilities of functionalized MWCNTs impregnated epoxy composite. To assure crack growth along the specimen's center line, the TDCB specimen was constructed with 45^{o} side grooves and a rectangular central groove.

Pre cracks were made at the end of the central groove and then tested for failure using an AE 50kN UTM at a load cell of 1 kN and a crosshead speed of 0.5 mm/min in order to determine the fracture toughness of the virgin sample (i.e., a sample without any prior damage). The MWCNT reinforced TDCB specimens were loaded and evaluated until the crack propagated to 20–40 mm in order to determine the fracture toughness of healed samples. After reaching that crack length range, cracked samples were unloaded and left in the TDCB silicon moulds and exposed to heat in autoclave as per the curing cycle temperatures (85^{o}C/2h and 130^{o}C/2h) self-heal because critical load and fracture toughness are independent of crack length within 20 - 40 mm of crack length [151,152].

6.3.3 Self-healing studies of CFRP composite

A common damage event, such as delamination was created in the CFRP composite to test the self-healing capacity of the pure and MWCNTBm reinforced CFRP composite. First, pure and MWCNTBm grafted CFRP composite flexural samples (ASTM-D790) were tested, and the corresponding delamination was noted. Later on, the fractured specimen was cured at 2 h/130 ^{o}C, 2 h/85 ^{o}C to cleave and reform the damaged area, known as healed sample. The self-healing efficiency (η) CFRP composite was assessed through flexural strength recovery and obtained by Eq. (6.1); $\eta = \frac{\sigma healed - \sigma damaged}{\sigma virgin - \sigma damaged}$.

6.3.4 Damping assessment of self-healing CFRP composite

The damping characterization of self-healing composites is essential to understand since composite structures vibrate under service circumstances. Impulse excitation technique (IET) and flexural vibration mode are taken into consideration in order to analyze the damping behavior of self-healing composites.

IET, which is an ASTM E 1876-compliant non-destructive technique based on impulses, essentially measures the material's dynamic elastic characteristics. IET uses resonant frequency to determine the specimen's elastic modulus and can thus be used to describe the specimen's damping characteristics. The test specimen was excited and given vibrations in this test setting using an impulse tool (excitation unit). These vibrating signals are picked up by a microphone and sent to a data gathering device before being sent on to RFDA software. The software delivers the resonant frequency and amplitude decay constant of the observed vibrations after meeting a predetermined convergence condition.

Figure 6.2 shows the experimental setup and schematics used in the current study. Equations (6.2) and (6.4) can be used to calculate the specimen dynamic elastic properties and damping factor.

Dynamic elastic modulus (E) = $0.9465 \frac{m f_f^2}{b} \left(\frac{L^3}{t^3}\right) T_1$ Eq.(6.2).

For samples with L/t > 20, T_1 can be figured out using

Eq.(6.3) $T_1 = \left[1.000 + 6.585\ \left(\frac{t}{L}\right)\right]$, damping factor $(Q^{-1}) = \frac{K}{\pi f_f}$ Eq.(6.4).

The relationship between the damping ratio and the damping factor (ζ) can be given by Eq.(6.5) $(Q^{-1}) = 2\zeta$.

Where m - mass of the specimen in g; b - width of the specimen in mm; t - thickness of the specimen in mm; L - Length of the specimen in mm; f_f - resonant frequency in Hz; T_1 - correction factor for flexural mode; Q^{-1} - damping factor; k - exponential decay parameter

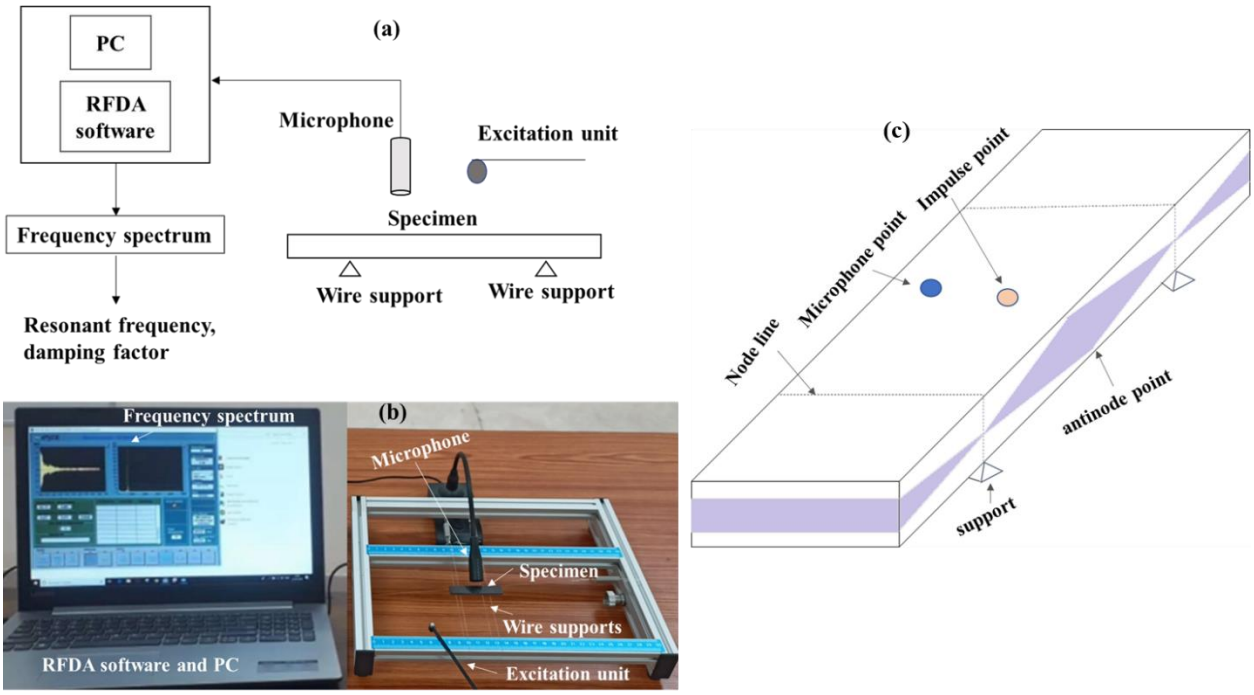

Figure 6.2. Impulse excitation technique setup (a) schematic view (b) Experimental setup (c) Flexural vibration mode

6.4 Results and Discussions

This section demonstrates the fabrication of amine-functionalized bismaleimide-grafted MWCNTs (with different weight ratios 0.5, 1.0, 1.5 wt.%) reinforced thermally reversible furan-maleimide self-healing CFRP composite. The tensile behavior, fracture morphology and self-healing assessment of polymer and CFRP composite was evaluated.

6.4.1 Tensile properties and fracture morphology of functionalized MWCNTs reinforced self-healing CFRP composite

The self-healing CFRP with MWCNTBm reinforced composite delamination and matrix cracking damage assessment before and after healing was carried through flexural loading, and mechanical properties like tensile strength, modulus, and strain % were evaluated.

A higher possibility of their silane/maleimide grafted MWCNT functionalization to improve mechanical strength, delamination resilience, and self-healing characteristics in hybrid CFRP composite has been theorized as a result of the large number of morphological alterations that were seen under high definition microscope. To verify the aforementioned, the tensile characteristics of the hybrid self-healing CFRP laminates have been assessed, and the change characteristics as a factor of maleimide functionalization preceded by filler reinforcement quantity are compared. The obtained tensile responses are illustrated in Figure 6.3 and the values are listed in Table 6.2. The variation in stiffness among matrix, carbon fiber/epoxy matrix interphase, filler/matrix interface, and individual fiber stiffness are the factors responsible for the non-linear response the of stress/strain curve, attributed to different self-healing resin fiber/volume fractions [144]. A large portion of the applied load is initially handled by a matrix with high stiffness and minimal deformation, increasing the slope of the curve. Once the micro-nano crack initiation and propagation begin via the fiber/matrix interphase, the composite total stiffness will be reduced due to stiffness variation in the filler/matrix/fiber interphase [141].

The tensile strength (σ_s), Elastic modulus (E) of the CFRP-35 were 501 MPa and 8.96 GPa, respectively. Fractographic examinations with FE-SEM show extensive Intra/inter-laminar deformation; this was caused by the defect propagation and nucleation at the matrix/fiber junction, which enabled matrix/fiber de-bonding and ultimately resulted in fiber pullout Figure 6.3 (c). For CFRP-45 they were increased to 15.16% (σ_s -577 MPa) and 48.77% (E -13.33 GPa) respectively, and further improvement was observed for 55 wt.% CFRP. The increase in tensile properties is due to an increase in the fiber/volume fraction, which further improves the hybridization and improved crosslinking between the low modulus polymer thermo-reversible DA bonds and high modulus stable epoxy-anhydride bonds, but it is inadequate to prevent fiber de-bonding shown by fractographic image Figure 6.3 (d). The CFRP-45 composite grade was selected as optimum (based

on the DA bonds generation and moderate strength), and MWCNTBm with different wt.% was infused into CFRP to further improve the tensile, elastic properties and self-healing characteristics.

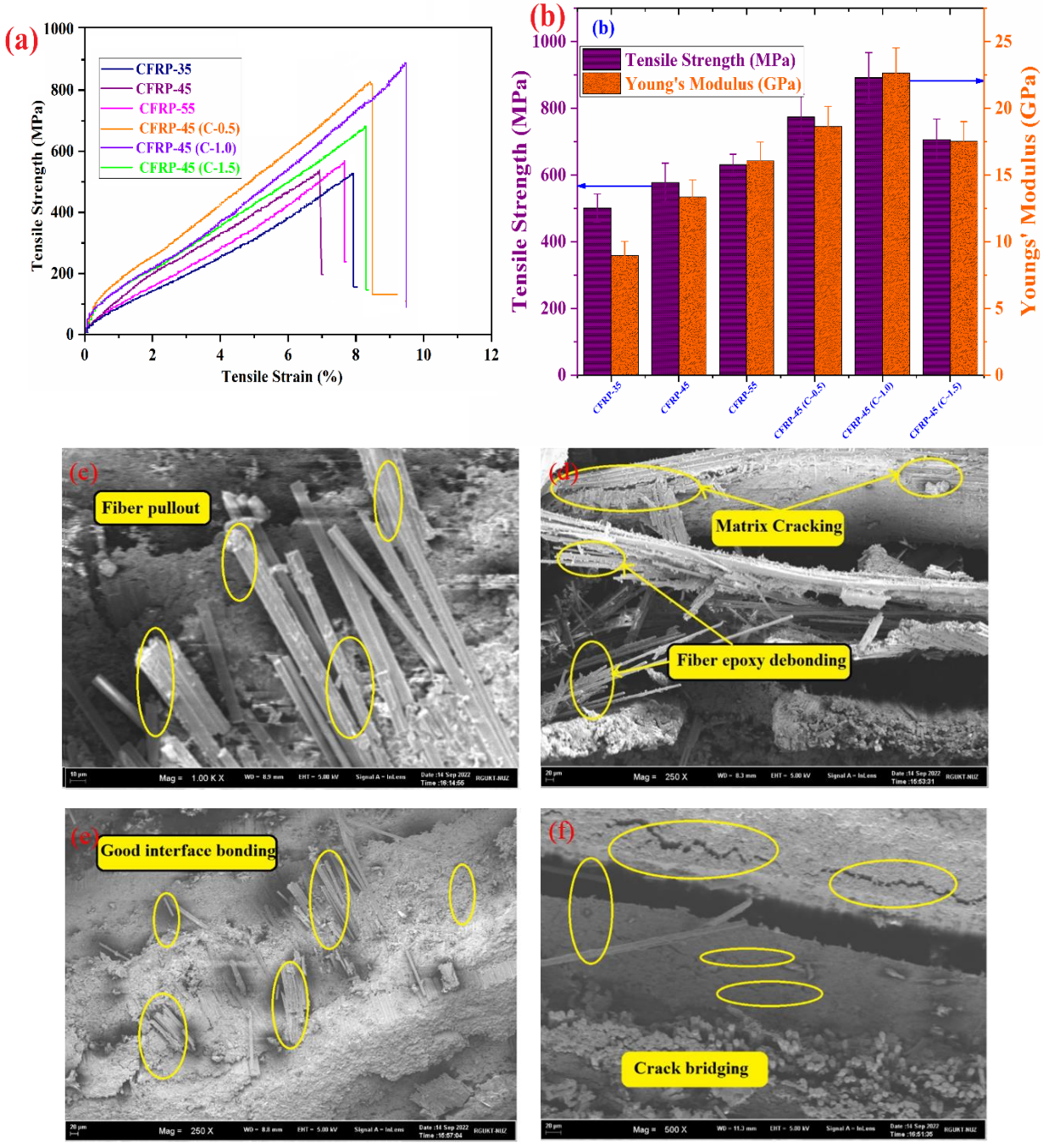

Figure 6.3. (a,b) Tensile strength and modulus of self-healing hybrid CFRP composite with varied MWCNTBm wt.%. Fracture morphology of (c) CFRP-35 (d) CFRP-45 (e) CFRP 45 (C-1.0) (f) CFRP 45 (C-1.5) (g)

The tensile strength and modulus for CFRP-45 (C-0.5) were further increased to 773 MPa and 18.54 GPa, respectively, and for CFRP-45 (C-1.0), the tensile properties (σ_s, E) were improved to 891 MPa and 22.63 GPa, respectively. This phenomenon can be ascribed due to sufficient transverse and lateral exfoliation of MWCNTBm, and also, fibers are typically found hidden by the epoxy matrix, emphasizing the limiting of defect propagation and nucleation at the matrix/fiber junction Figure 6.3 (e). Furthermore, delamination resistance was offered by the matrix/fiber interlaminar junction by forming a significant amount of resin debris both on the sides and surfaces of fibers, shown by the fractographic image Figure 6.3 (e). H Sharma et al. [142] prepared carbon fiber reinforced composite with Graphene oxide (GO) nanosheet reinforcement and reported 750 MPa tensile strength, but our work demonstrated much improvement in tensile strength due to MWCNTs functionalization. Furthermore, CFRP-45 (C-1.5), the tensile strength (σ_s), and elastic modulus (E) were decreased to 705 MPa and 17.52 GPa. This attributes to the matrix cracking with micro crack development caused by the aggregated MWCNTBm in CFRP that ultimately results in matrix/fiber de-bonding Figure 6.3 (f). In addition to the preceding, when the filler percentage was increased beyond 1.5 wt.%, decreased tensile characteristics were observed due to filler agglomeration. From the data, CFRP-45 (C-1.0) exhibited superlative tensile characteristics than other composites.

6.4.2 Self-healing assessment of polymer composite and CFRP composite

In this section bismaleimide grafted functionalized GNPs/MWCNTs are reinforced in self-healing polymer composite are fabricated and characterized to know the strength before and after fracture and also finds the healing efficiency. After consecutive fracture on the same damaged spot how much the sample regaining the strength was also tested.

6.4.2.1 Self-heling assessment of functionalized GNPs infused polymer composite

A double tapered cantilever beam (TDCB) [136] sample was used to test the fracture properties of polymer nanocomposites. The side groove of the TDCB shape indicates the path of fracture propagation across the sample's center line. Figure 6.4 shows geometry and TDCB specimen loading in UTM.

The specimen was tested to its fracture, and the uppermost strength of TDCB was measured. The damaged specimen was placed in a formerly made silicon mould and temperature curing according to TG-DSC data to test its self-healing capability. Silicone rubber flexibility allows it hold the fractured sample tightly in the mould while slight pressure is applied through the edges.

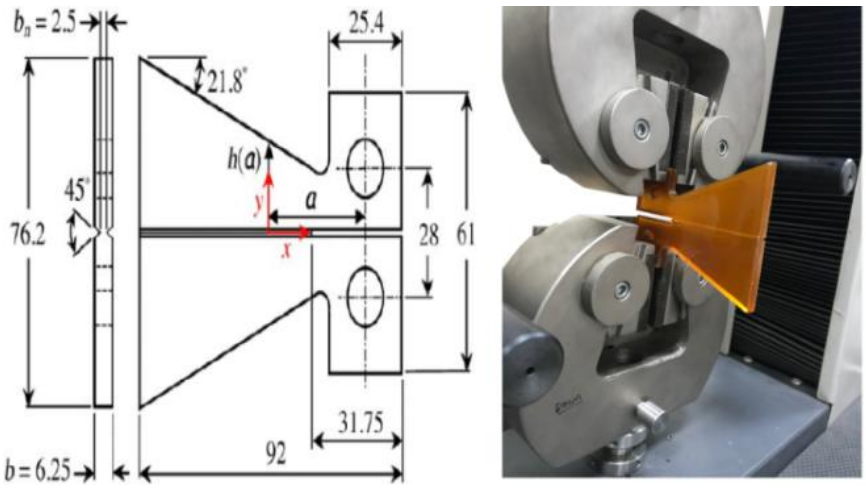

Figure 6.4. TDCB sample loading in UTM

The sample was exposed to a constant temperature of 130 ^{o}C for 2 h to generate r-DA bond reaction by separating the cross-linking chains through the composite, then cured at 80 ^{o}C for another 2 h to reconstitute the DA adduct by reuniting the disconnected cross-linked chains. The self-healing efficiency computed as follows: Eq. (6.6) Healing Efficiency = Break Load $_{(Healed)}$ / Break Load $_{(Virgin)}$.

Figure 6.5(a) shows the variation of break load before, after fracture and respective healing efficiency of polymer nanocomposites with GNPBm reinforcement. The maximum loading values for virgin TDCB samples 35FMDA, 45FMDA, and 55FMDA were 105, 162, and 245 N, respectively, whereas it was 76, 102, and 75 N for healed TDCB samples, implying 72, 61, and 30% healing efficiency, respectively.

The healing efficiency decreased as the load increased due to more resin irreversibility, as shown in the graph. The load capacity was enhanced by 21% with 0.5 wt % (GNPBm) reinforcement in the epoxy matrix, and it enhanced by 30% with 1.0 wt % GNPBm. Furthermore, at 1.5 wt% GNPBm, aggregation was seen in the polymer nanocomposite, resulting in load capacity reduction. The creation of a covalent bond can promote crosslinking and make stress

transfer from the terminal amine/maleimide nanoparticles with the matrix (resin/hardener), resulting in improved healing efficiencies of 45FMDA (Gr-0.5), 45FMDA (Gr-1.0), and 45FMDA (Gr-1.5) which were 86, 90, and 91 percent respectively. As a result, GNPBm not only improves the mechanical properties but also exhibits self-healing characteristics due to its dienophile nature, which repairs cracks in the composite.

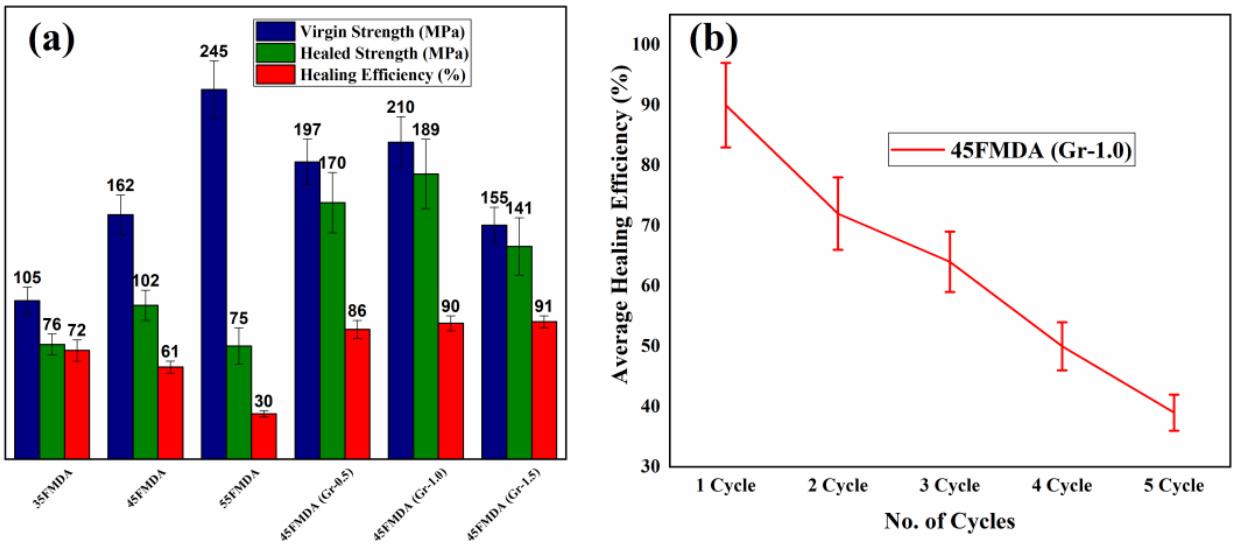

Figure 6.5. Variation of (a) Breaking load for virgin, healed sample and Healing Efficiency (c) Healing Efficiency over the number of cycles on the same damaged spot

Figure 6.5(b) shows fluctuation in healing efficiency during numerous cycles to evaluate multiple healing. 45FMDA (Gr-1.0) healed sample was loaded and tested up to fracture with the same testing conditions. This process was repeated to measure multiple times healing behavior. The findings reveal that a significant degree of polymer composite strength was restored even after three consecutive injuries, and after the fourth and fifth healing cycles, the healing efficiency dropped significantly. The healed samples had lower stress-at-break and lower strain-at-break than the original samples after the healing cycles. As a result, FMDA polymer nanocomposite therefore exhibits excellent mechanical and self-healing characteristics.

6.4.2.2 Self-heling assessment of functionalized MWCNTs infused polymer composite

The specimen was tested until it broke, and the highest TDCB strength was recorded. The fractured sample was inserted into a previously created silicon rubber mould and exposed to 130 ^{o}C for 2 hours then cured at 85 ^{o}C for another 2 hr according TG-DSC data. At 130 ^{o}C, the cross

linking network structure across the composite was detached, and the DA adduct was reconstructed at 85 ^{o}C by reconnecting the detached cross linking chain. The healing efficiency was calculated using the following equation Break Load $_{(Healed)}$ / Break Load $_{(Virgin)}$ = Healing Efficiency. The highest load values for virgin TDCB samples 35DA, 45DA, and 55DA are 108, 165, and 249 N, respectively, whereas for healed TDCB samples are 76, 105, and 74 N, indicating 70, 63, and 29% healing efficiency. The results clearly show that as the strength increased, the healing efficiency reduced due to an increase in epoxy resin irreversibility, which leads to a reduction in the number of DA bonds formed. The Bm-MWCNT was reinforced in epoxy with varied wt % to balance both strength and healing efficiency. The load capacity of 45DA with 0.5wt % (Bm-MWCNT) was enhanced by 18% and it was improved by 32% with 1.0 wt. % reinforcement. Furthermore, 1.5 wt.% Bm-MWCNT, aggregation in the polymer epoxy matrix was observed results in decrease in load capacity. Bm-MWCNT reinforced DA epoxy matrix, a higher number of DA and r-DA bond associations at the interface was observed and the healing efficiencies of 45DA (C-0.5), 45DA (C-1.0), and 45DA (C-1.5) were reported as 84, 89, and 91 percent respectively.

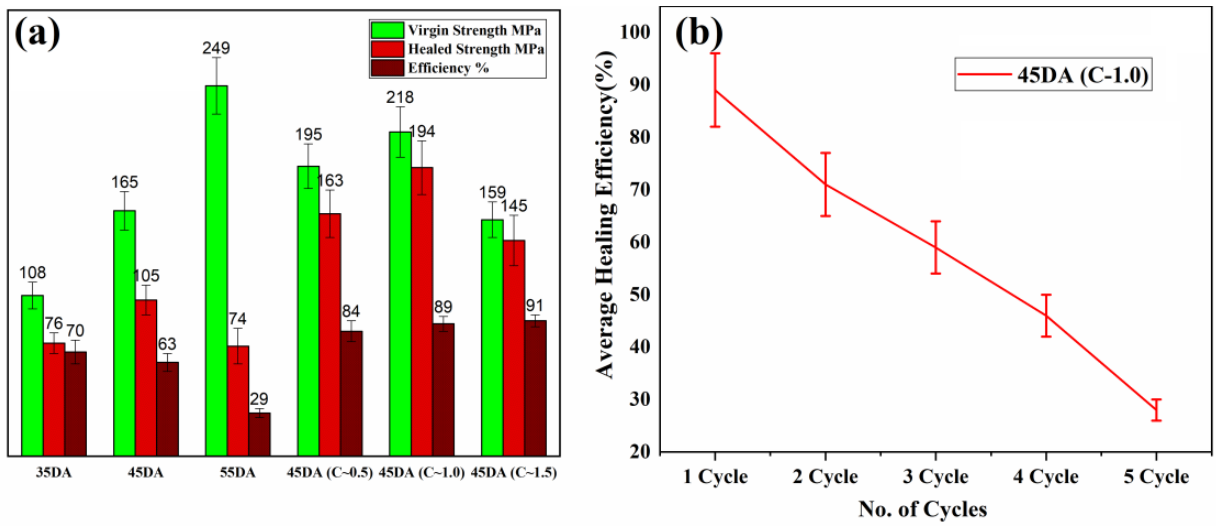

Figure 6.6 TDCB strength, healing efficiency of MWCNT infused self-healing polymer composite

Due to the reversibility of the DA reaction, subsequent cyclic DA/rDA reactions would reconfigure the network structure. Figure 6.6 depicts the strength variation of the healed composites over five healing cycles. To assess the recovered TDCB strength of the composite, the healed sample was tested at the same spot and the strength was recorded. The results show that

even after three consecutive injuries, a reasonable amount of composite strength was regained, with healing efficiency of 88.9 percent, 71.1 percent, and 59.1 percent for the first, second, and third healing cycles respectively. After fourth and fifth healing cycle, the healing efficiency drops significantly, reaching 45.4 and 27.9 percent respectively. As a result, the Bm-MWCNT/DA-epoxy composites benefit from self-healing without compromising integrity or load carrying ability, which makes them stand out among self-healing epoxy composites with a high self-healing efficiency and repeatable healing characteristic.

6.4.2.3 Self-heling assessment of functionalized MWCNTs infused CFRP self-healing composite

Since composite structures are subject to the flexural type of loads under service conditions, it is essential to understand how the addition of MWCNTBm impacts their flexural strength, modulus and the healing efficiency was estimated based on the recovery in flexural strength after damage. The variation in flexural strength before and after healing with various weight percentages of MWCNTBm reinforcement was depicted in Figure 6.7 (a, b) and the values are listed in Table 6.2.

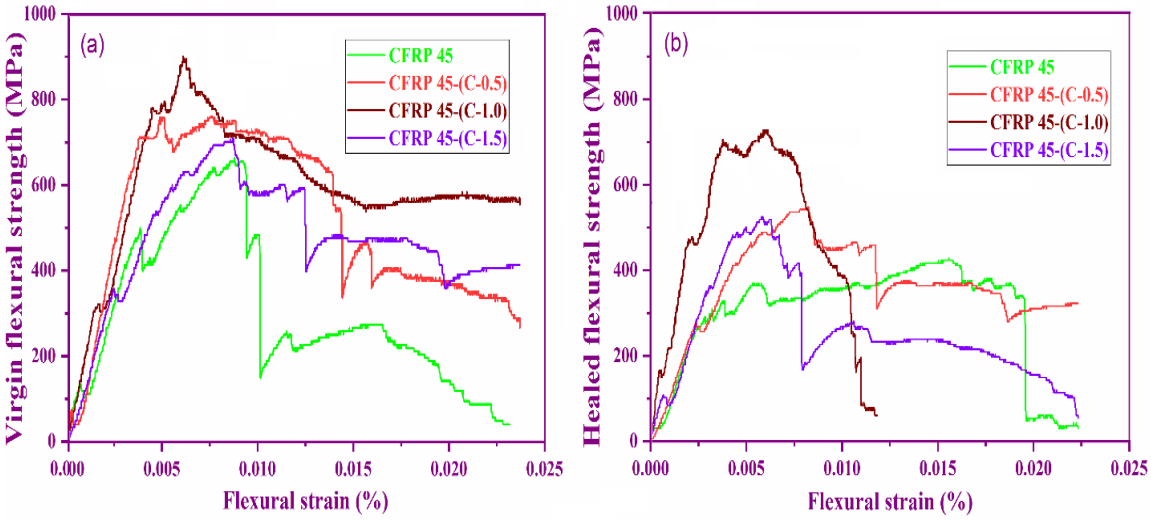

Figure 6.7. Variation in flexural strength of self-healing hybrid CFRP composite

The pure CFRP-45 (C-0) composite reported a flexural strength of 641 MPa and a flexural modulus of 34.57 GPa, and with the addition of MWCNTBm reinforcement, both flexural strength and modulus of the CFRP were increased. With the addition of 0.5 and 1.0 wt.% MWCNTBm to the

pure CFRP-45, the flexural strength and modulus was improved by 18% (751 MPa) and 38% (885 MPa), respectively. According to the flexural graph, the matrix containing MWCNTBm (0.5, 1.0 wt.%) has the ability to enhance the composite load-bearing capacity and minimize deformation at the matrix/fiber interface. Therefore, the highest improvement in flexural properties for CFRP-45 (C-1.0) attributed to effective silane/maleimide functionalization of MWCNT, promotes the homogenous distribution throughout matrix/fibers and better stiffness for CFRP due to the hydrophobic structure of silane moieties. Pathak et al. [146] reported the impact of graphene oxide (GO) reinforced CFRP composite flexural properties and achieved 710 MPa flexural strength by reinforcing 0.3 wt.% of GO. Instead, our research highlights the uniqueness of maleimide grafted MWCNTs has a distinctive ability to improve flexural properties. Further, with 1.5 wt.% addition, the flexural strength was decreased to 684 MPa. Two key reasons, the rise in matrix viscosity and the aggregation of MWCNTBm, can be attributed to the decrease in flexural strength. Improved epoxy matrix viscosity also reduces the probability of the fibers being completely wet, which can lower the composite strength [153]. Modulus reduction can be attributed to poor interface between MWCNTBm/matrix/fiber as well as less integration of low modulus self-healing FGE resin into high modulus matrix.

The healing efficiency of MWCNTBm reinforced CFRP hybrid composite obtained through recovery in flexural strength after damage through three-point bending test [136] are shown in Figure 6.8 (a,b). Matrix-micro cracking and delamination damages were developed in the CFRP composite after fracture, and the fractured specimens were cured according to TG-DSC data. The damaged specimens were cured at 130 ^{o}C for 2 h to separate crosslinking structure of the composite (r-DA reaction), followed by 85 ^{o}C for another 2 h to re-form the cross-linking structure (DA reaction), the outcome known as a healed specimen. During the healing mechanism, un-reacted furan moieties generated from r-DA (retro DA reaction) could interact with the maleimide moieties to reconstruct DA reversible bonds in the matrix/fiber/filler interfacial area. As a result, a new interphase among the epoxy-filler network and carbon fiber is produced in response to the creation of new DA adducts. The healed specimen re-tested to measure the healed strength under the same testing conditions. This criterion suggests that the fractured incidents were repaired, which resulted in the restoration of fracture resistance after healing.

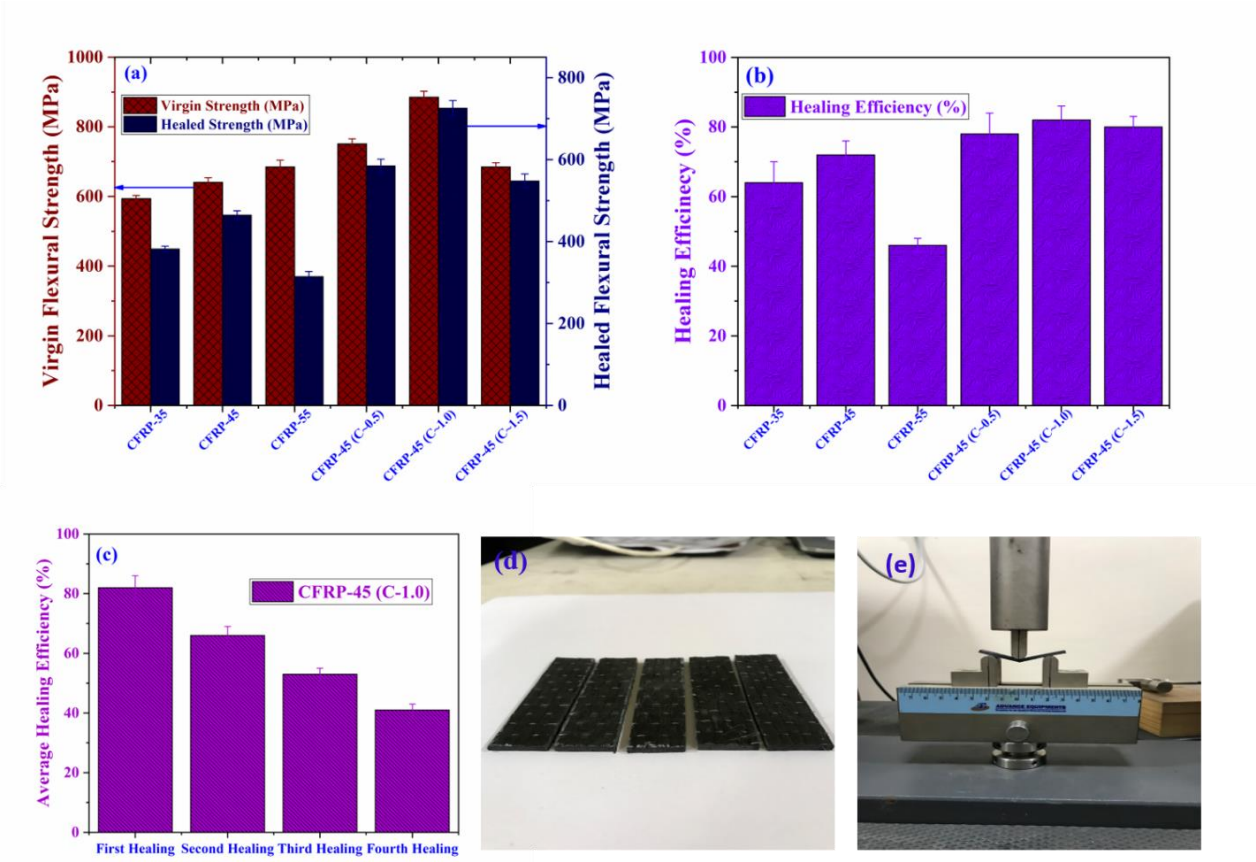

Figure 6.8. (a) Flexural strength variation between virgin and healed sample (b) Healing efficiency of hybrid CFRP composite (c) Average Healing efficiency (d) Flexural sample prepared (e) Flexural Testing

The healed CFRP-45 sample exhibited a 37.84 % reduction in flexural strength (465 MPa) compared to virgin CFRP-35 and showed a healing efficiency of 72.30 %. This is attributed due to effective hybridization maleimide, FGE, epoxy with CFRP. The CFRP-45 (C-0.5) sample showed a 21.53 % reduction in flexural strength than the virgin sample and exhibited 78.47 % healing efficiency. It was noticed that the healed samples of MWCNTBm reinforced CFRP showed greater flexural strength recovery compared to pure CFRP, which confirms the effective healing interface between fiber/epoxy/filler and the dienophile nature of MWCNTBm which in turn increases the healing efficiency. The CFRP-45 (C-1.0) showed much recovery in flexural strength than all other grades and exhibited 82% healing efficiency. Thus, along with improved flexural strength, more number of DA bonds formation with MWCNTBm in the CFRP laminate resulted in increment in healing efficiency. This improvement in healing efficiency is due to, the formation of a covalent bond, which can encourage crosslinking and stress transfer between the

self-healing matrix and the maleimide grafted MWCNTBm. W. Zhang et al. [100] generated an interface between epoxy matrix and surface of carbon fibers to inhibit the self-healing characteristics by grafting the maleimide functional groups on the carbon fiber surface. They reported 80 % healing efficiency, but our work little improvement in self-healing efficiency by reinforcing maleimide grafted MWCNTs into CFRP. The CFRP-45 (C-1.5) sample showed a decreased flexural strength recovery ascribed to fiber pull-out and matrix cracking due to transverse accumulation of MWCNTBm and inadequate fibers/matrix interfacial contact. Flexural testing was repeated numerous times on the same damaged spot, the self-healing CFRP composite exhibited significant amount of flexural strength restoration even after three consecutive fractures, with a considerable healing efficiency Figure 6.8(c). After the first healing cycle the sample was again tested to measure the difference in flexural strength recovery for the estimation of healing efficiency in the second healing cycle and so on. Even after 4 consecutive healing cycles, a significant efficiency around 43 % was observed. Further decrease in healing efficiency attributed to moisture absorption at broken surface, foreign particle contamination from atmosphere, and degradation of DA adduct formation during curing.

Table 6.2. Description of tensile strength, modulus and flexural strength variation before and after healing, along with respective healing efficiency

Composite type	Tensile Strength (MPa)	% Strain	Elastic Modulus (GPa)	Flexural Strength (MPa)		Healing Efficiency (%)
				Virgin	Healed	
CFRP-35	501 ± 42	8.32 ± 0.69	8.96 ± 1.06	594 ± 09	382 ± 07	64 ± 6
CFRP-45	577 ± 58	8.67± 0.71	13.33 ± 1.31	641 ± 13	465 ± 10	72 ± 4
CFRP-55	630 ± 32	7.98± 0.53	16.05 ± 1.42	685 ± 19	315 ± 12	46 ± 2
CFRP-45 (C~0.5)	773 ± 69	9.32 ± 0.91	18.54 ± 1.50	751 ± 15	585 ± 16	78 ± 6
CFRP-45 (C~1.0)	891 ± 76	10.45 ± 1.01	22.63 ± 1.88	885 ± 17	726 ± 18	82 ± 4
CFRP-45 (C~1.5)	705 ± 69	8.87 ± 0.84	17.52 ± 1.47	684 ± 12	548 ± 17	80 ± 3

6.4.3 Fracture morphology analysis of self-healing CFRP composites (Flexural sample)

Figure 6.9 presents the FE-SEM fractographic images of CFRP/MWCNT hybrid composite fractured tensile specimens. The morphology of the broken surface of hybrid CFRP is

shown in Figure 6.9 (a). According to researchers [154], fracture can occur in various forms in CFRP composites, such as damaged fibers, fiber/matrix interface separation, delamination, and matrix cracks.

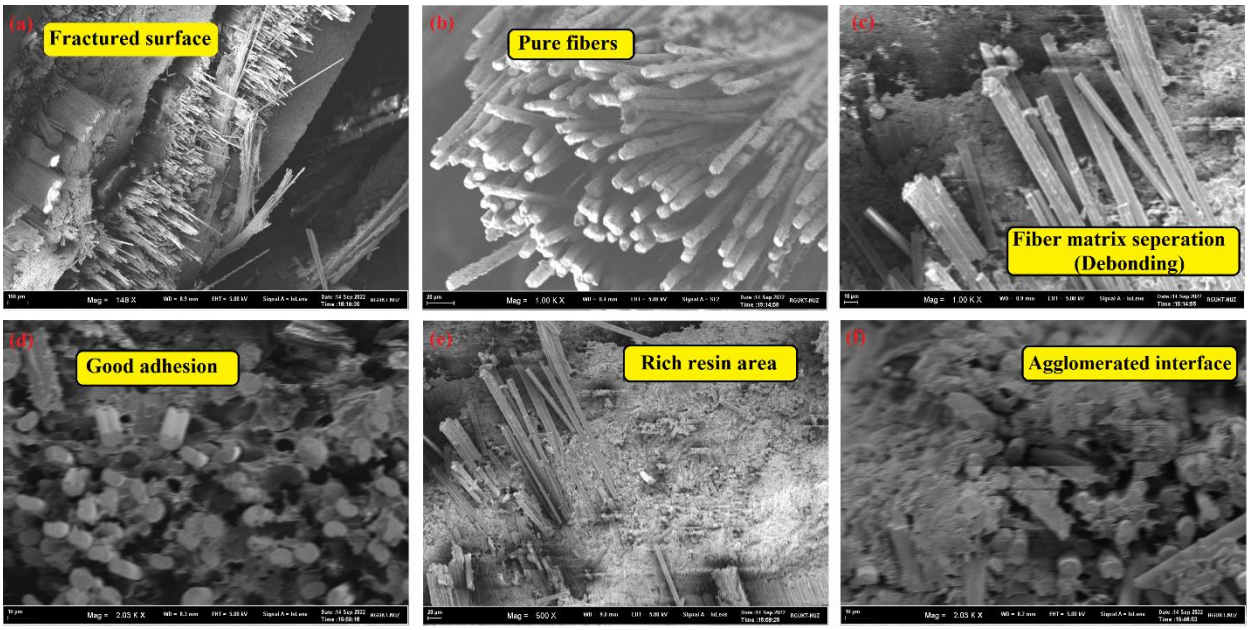

Figure 6.9. FE-SEM fractographic images of self-healing hybrid CFRP composite flexural fractured samples (a-c) Pure CFRP (C-0) (d-e) CFRP-45 (C-1.0) (f) CFRP-45 (C-1.5)

For CFRP-45 sample, as fractured surface, pure fibers Figure 6.9 (a-b) matrix/fiber de-bonding, and fiber pull-out were observed in Figure 6.9 (c) due to failure energy absorption at the interlaminar zone. By reinforcing MWCNTBm in CFRP, reduced de-bonding was observed in Figure 6.9 (d). Further extensive intra/inter-laminar deformation was observed, this was caused by the defect propagation and nucleation at the matrix/fiber junction, which enabled matrix/fiber de-bonding and ultimately resulted in fiber pullout. For CFRP-45 (C-1.0), delamination resistance offered by the matrix/fiber interlaminar junction by forming a significant amount of resin debris both on the sides as well as surfaces of fibers was observed, as shown by Figure 6.9 (e). Furthermore, fibers are typically seen hidden by the epoxy resin matrix, emphasizing the limiting of defect propagation and nucleation at the matrix/fiber junction. This is due to improved grafting of the silane/MWCNTBm among sieves of CFRP interlayer laminates, which led to an effective interfacial connection between matrix/fibers/nano-fillers and improved the bonding strength of the CFRP laminate. From the CFRP-45 (C-1.5) micrographs, fiber matrix separation and matrix cracking were observed due to agglomeration of MWCNTBm and inadequate interfacial contact

between the matrix/fibers/filler Figure 6.9 (f). The surface morphology with greater filler content exhibits bare fiber surfaces with minimal epoxy debris and weakly integrated bulk epoxy matrix/fibers with aggregated MWCNTBms.

6.4.4 CFRP composite healing efficiency comparison through IET and Flexural testing

Figure 6.10 shows the sample's vibration signals and corresponding frequency spectra of CFRP-45 wt.% (C-0.5, 1.0, 1.5). The findings reveal that the resonance frequency of CFRP was increased with silane/maleimide grafted MWCNT reinforcement. This can be associated with reducing the specimen vibrational response by an increase in the dissipation of vibration energy throughout the structure [155]. The resonant frequency of pure CFRP was lower than MWCNTBm-infused CFRP can be attributed to a reduction in vibrational energy absorption. Equations (6.2) and (6.5) were used to calculate the CFRP elastic modulus and damping factor using their respective frequency domain data.

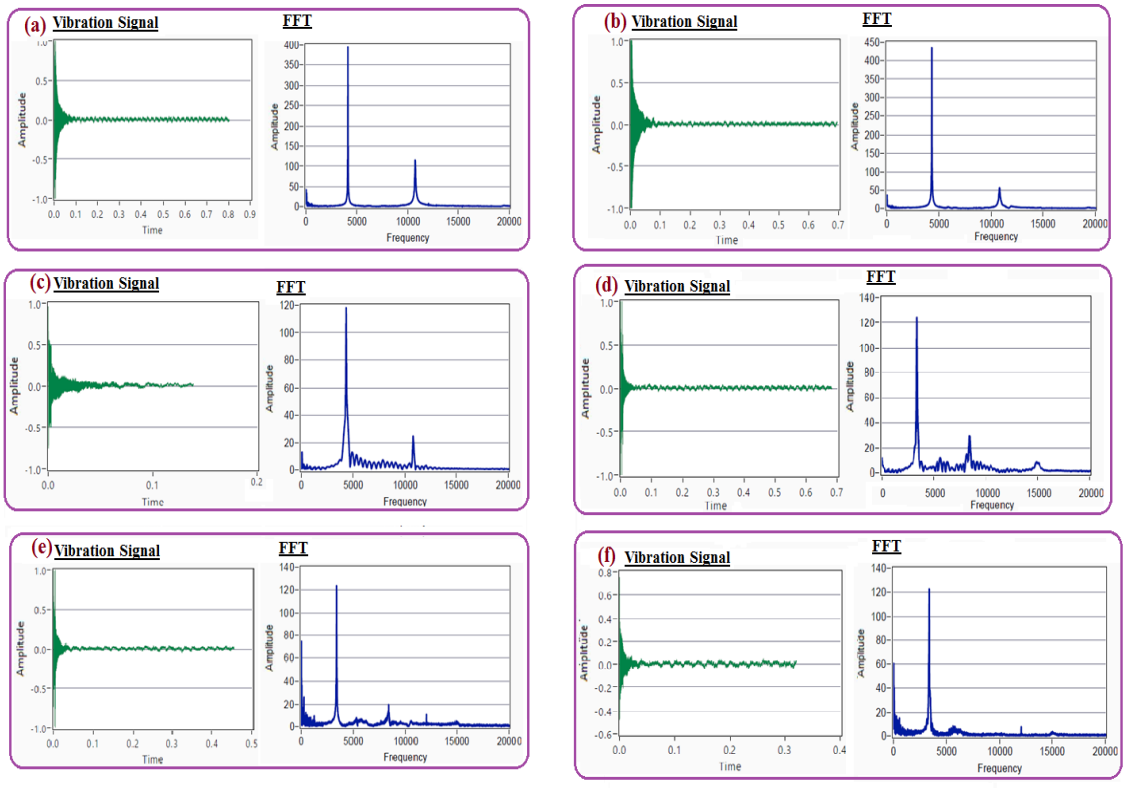

Figure 6.10. Frequency and time domain spectra of MWCNTBm reinforced self-healing CFRP composite of (a,c,e) virgin and (b,d,f) healed samples of MWCNTBm (0.5, 1.0, and 1.5 wt.%) CFRP composites respectively

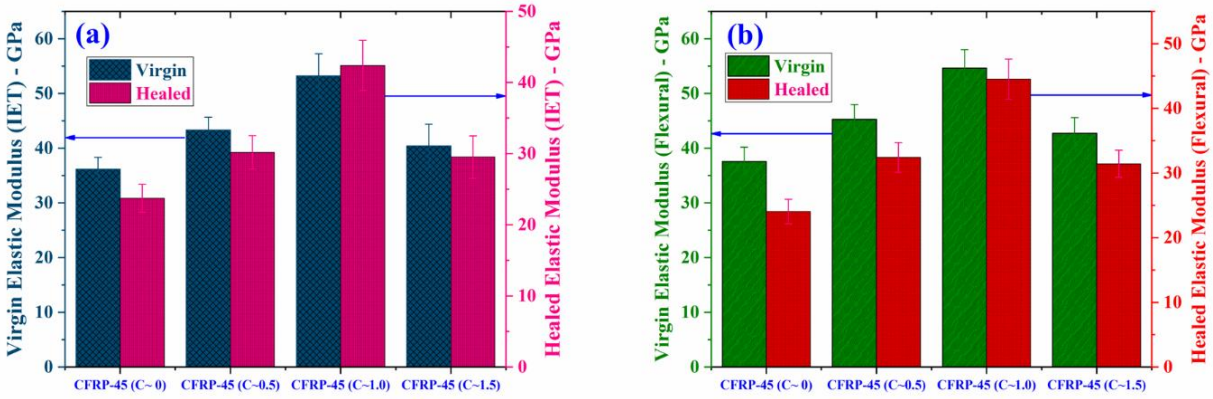

Figure 6.11. Elastic modulus recovery of virgin and healed samples through (a) IET technique and (b) flexural test

The vibration signal, corresponding resonant frequency and elastic modulus recovery are illustrated in Table 6.3. The findings demonstrate a noticeable improvement in the damping factor with the infusion of MWCNTBm, improving the composite energy absorption capability. In addition to MWCNTBm wt.%, the viscoelastic properties of the epoxy resin and the interfacial connection between the matrix/MWCNTBm also affect the damping factor. In general, flaws such as micro voids, and different interfaces spread during vibrations or are vulnerable to slippage, which promotes dissipating vibration energy. The lower damping factor of pure CFRP in comparison to MWCNTBm can be attributed to CFRPs natural frequency because it is greater than pure CFRPs natural frequency.

Table 6.3. Description of composite resonant frequency, damping factor and elastic modulus (through IET and flexural test) before and after healing

Composite type	Resonant frequency (Hz)		Damping factor		Elastic modulus (GPa)			
					Through IET		Through Flexural	
	(B.H)	(A.H)	(B.H)	(A. H)	(B.H)	(A.H)	(B.H)	(A.H)
CFRP-45 (C~ 0)	4348.15	4043.64	0.0029	0.00335	36.14±2.15	23.73±1.95	37.57±2.6	24.04 ± 1.9
CFRP-45 (C~0.5)	4230.98	3942.32	0.01324	0.01128	43.31±3.74	30.18±2.34	45.27 ± 2.7	32.41± 2.3
CFRP-45 (C~1.0)	4086.17	3918.83	0.06148	0.01326	53.21 ±4.01	42.40±3.51	54.61 ± 3.4	44.52±3.1
CFRP-45 (C~1.5)	4118.9	4105.8	0.01534	0.01326	40.41±3.95	29.52±2.98	42.70 ± 2.9	31.42± 2.1

6.5 Conclusions

In this chapter, we have fabricated and characterized thermally remendable self-healing CFRP laminate composite through Diels-Alder cycloaddition. The influence of chemical functionalization (oxidation followed by silane/maleimide grafting) of MWCNTs as reinforcement in CFRP composite and the impact on mechanical, damping, and self-healing characteristics were evaluated.

- It was observed that the oxidation significantly affected the de-aggregation of MWCNTs as per HR-TEM and FE-SEM micrographs, and observed that MWCNTs experienced sufficient lateral and transverse exfoliation over 60 hours of oxidation.
- The characterization data of FTIR and NMR demonstrates the furan/oxirane ring presence in synthesized FGE. The chemical functionalization (oxidation 60 h and APTES silanization) followed by effective maleimide grafting on the surface of MWCNT was confirmed through XRD, FTIR, and TG-DTA data.
- According to TG-DSC data, the maximum number of DA/rDA bonds association (specific enthalpy 12.92 J/g) was observed for CFRP-45 (C-1.0). The impact of MWCNTBm percentage on the tensile strength and modulus of hybrid self-healing CFRP laminate was examined by reinforcing various wt.% (0.5,1.0 and 1.5) and found that CFRP-45 (C-1.0) tensile strength and modulus were increased to 891 MPa and 22.63 GPa respectively with regard to CFRP-45.
- Further, small aggregation was observed in 45 wt.%(C-1.5), resulting in decreased tensile properties. The healing efficiency of hybrid CFRP laminate was evaluated through flexural strength regaining, and it was found that the infused MWCNTBm not only improved the mechanical properties but also promoted healing efficiency, which confirms its dienophile nature.
- The CFRP-45 (C-1.0) exhibited high healing efficiency of 82 % than other grades because of the high stiffness, hydrophobic nature of silane/maleimide moieties, and high load-bearing capability of composite, which resulted in less deformation at fiber/filler/matrix interface.
- The resonant frequency of CFRP-45 (C-1.0) was improved, resulting in a high damping factor because of increased vibrational energy absorption throughout the composite.

- The fractographic investigation of damaged MWCNTBm infused CFRP-45 (C-1.0) composite exhibited reduced fiber/matrix delamination and de-bonding mechanism.
- Thus this work demonstrates the stiffness enhancement at the matrix/fiber/nanofiller interface of CFRPs and the healing behavior of MWCNTBm infused CFRP composite in a high performance application.

Chapter 7

Conclusions and Future scope

7.1 Conclusions

Restoration of the structural integrity of damaged CFRP composite through thermally reversible Diels-Alder bonds with the exact interface between matrix/fiber is extremely desirable for manufacturing high-performance self-healing laminates. This work demonstrates the fabrication of amine-functionalized maleimide-grafted GNP and MWCNT (with different weight ratios 0.5, 1.0, 1.5 wt.%) reinforced thermally reversible furan-maleimide self-healing polymer and CFRP composite. In evaluating high-performance GNPs and MWCNTs based carbon fiber composite, effective chemical functionalization of fillers for sufficient exfoliation and precise interface interactions with resin matrix are challenging to attain due to significant interlayer cohesive energy and inactive surfaces of composite. Herein, we demonstrate an effective way to produce CFRP composite with amended interfacial characteristics via the incorporation of MWCNT through oxidation followed by silane functionalization with their exfoliation levels(0/48/60/72h). The main objective of this work is to investigate matrix/fiber/nanofillers interface junction healing properties of the CFRP composite before and after damage. Furthermore, it is intended to re-form structural stability over the CFRP interface junction of the damaged area and also examine the mean healing efficiency. Further, the damping characteristics of CFRP were investigated using the impulse excitation technique (I.E.T.). This article aims to produce the most durable hybrid self-healing CFRP composite and analyze the mechanical and damping behavior based on different oxidation times followed by amine functionalization and maleimide grafting.

- Optimum stoichiometric ratio of self-healing resin:
    - 12 g BMI (0.027 mol) + 10.3 g FGE (0.054 mol) mixed at 90 ^{o}C about 5 minutes.
    - With mechanical stirring, 15.21 g DGEBA (45 wt. % in BMI, FGE and DGEBA compound) was added to the resultant solution and cured using MHHPA.
    - Curing condition, Autoclave - 85 ^{o}C / 8 h, 130 ^{o}C / 8 h, and 85 ^{o}C / 8 h.
    - Healing condition, Autoclave - 130 ^{o}C / 2 h, and 85 ^{o}C / 2 h

- The characterization data of ^{1}H NMR, ^{13}C NMR successfully demonstrates the interaction of furan and oxirane rings in synthesized FGE. TG-DSC data reveals a maximum enthalpy release of 8.16 J/g for 45DA due to superior DA-rDA bond formations.

- It was observed that the oxidation level significantly affected the de-aggregation of MWCNTs. The FE-SEM and HR-TEM analysis showed that the aggregated MWCNTs experienced sufficient transverse and lateral exfoliation over 60 hours of oxidation (OAC-60) and created a 2D networked structure.
- From the XRD data the mean crystalline size of the functionalized GNPs and MWCNTs was found to be 18.8 and 4.17 nm respectively and well confined with data in JCPDS file No (75-2078) and (41-1487) respectively. The EDX data supports the uniform adhesion of silane oligomers (O-H, C=O and COOH) to GNPs and MWCNTs surfaces.
- The DTA curves demonstrate that, for 60 h oxidation, the temperature associated with the maximal degradation rate is higher as a result of the stronger covalent connections between the silane moiety and GNP and MWCNT surface.
- Three new characteristic peaks were observed at 1047, 1019, 805 cm^{-1} attributes to asymmetric stretching of (Si-O-Si), deformation stretching of (Si-O-C) and (Si-OH) respectively confirms the effective silanization and 1140 cm^{-1} and 1450 cm^{-1} confirms the effective C-N-C group of bismaleimide functionalization according to FTIR spectra.
- The functionalized GNP and MWCNT is not only thermally stable and mechanically strong, but it also exhibits self-healing properties due to its dienophile nature.
- The homogeneous dispersion pattern of GNPBm was discovered with 0.5 and 1.0 wt % reinforcement and 1.5 wt. % GNPBm, there was little aggregation and porosity development was observed, leading to poor mechanical properties.
- FESEM morphological images of 45FMDA (Gr-1.0) demonstrate superior dispersion quality and toughing mechanisms, as GNPBm arrests crack propagation and provides crack diversion and the highest tensile strength and optimum healing percentage of 9.7 MPa and 90 % respectively was observed.
- Furthermore, 45DA (C-1.0) nanocomposite exhibits maximum tensile strength, elastic modulus and optimal healing percentage of 11.2 MPa, 2871 MPa and 89% respectively.

- With the incorporation of 1 wt.% OAC-60 in CFRP laminates, using sonication and vacuum bagging, significant improvement in tensile strength (1250 MPa) and modulus (30.60 GPa) about pure-CFRP was observed.
- The improved flexural strength (1252 MPa), modulus (74.27 GPa) and w.o.f. (54.85 GPa) with regard to pure CFRP was observed for CFRP-Si60(1.0) because of the high stiffness, load bearing capability of the composite, which resulted in less deformation at the fiber/matrix/filer interface.
- According to TG-DSC data, the maximum number of DA/rDA bonds association (specific enthalpy 12.92 J/g) was observed for CFRP-45 (C-1.0). The impact of MWCNTBm on mechanical performance of hybrid self-healing CFRP laminate was examined by reinforcing various wt.% (0.5,1.0 and 1.5) and found that CFRP-45 (C-1.0) tensile strength and modulus were increased to 891 MPa, 22.63 GPa respectively with regard to CFRP-45.
- Further, small aggregation was observed in 45 wt.%(C-1.5), resulting in decreased tensile properties. The healing efficiency of hybrid CFRP laminate was evaluated through flexural strength regaining, and it was found that the infused MWCNTBm not only improved the mechanical properties but also promoted healing efficiency, which confirms its dienophile nature.
- The CFRP-45 (C-1.0) exhibited high healing efficiency of 82 % than other grades because of the high stiffness, hydrophobic nature of silane/maleimide moieties, and high load-bearing capability of composite, which resulted in less deformation at fiber/filler/matrix interface.
- 1.0 wt.% of MWCNTs filler concentration and 85^{o}C/8 h, 130^{o}C/8 h, and 85^{o}C /8 h +2 bar healing condition are recommended to fabricate self-healing CFRP composite.
- The resonant frequency of CFRP-45 (C-1.0) was improved, resulting in a high damping factor because of increased vibrational energy absorption throughout the composite.
- The fractographic investigation of damaged MWCNTBm infused CFRP-45 (C-1.0) composite exhibited reduced fiber/matrix delamination and de-bonding mechanism.
- Thus this work demonstrates the stiffness enhancement at the matrix/fiber/nanofiller interface of CFRPs and the healing behavior of MWCNTBm infused CFRP composite in a high performance application.

7.2 Future scope

Even though the current study addressed several basic issues with the manufacturing and evaluation of self-healing capabilities in polymer composites, there is still much room for improvement. The factors listed below can be taken into account for future research.

- The combination of thermally reversible and microencapsulation-based self-healing CFRP composite fabrication
- Fatigue analysis of self-healing CFRP composites
- In the present study developed functionalized GNPs and MWCNTs are used to address structural integrity. However, developed functionalized GNPs and MWCNTs based system can be employed in other applications such as smart adhesive systems.
- Functionalized GNPs and MWCNTs reinforced CFRP can be evaluated for self-healing performance in various modes of fracture based on fracture toughness recovery
- Functionalized GNPs and MWCNTs reinforced epoxy and CFRP composite can be modelled and evaluated for optimum reinforcement wt.%, healing conditions and maximum healing efficiency at various environmental conditions.
- Machine learning approaches like data augmentation through ANN can be employed to predict the data at the nano level by taking a 1 % standard deviation

References

[1] White, S.R., Sottos, N.R., Geubelle, P.H., Moore, J.S., Kessler, M.R., Sriram, S.R., Brown, E.N. and Viswanathan, S., 2001. Autonomic healing of polymer composites. *Nature*, *409*(6822), pp.794-797.

[2] Brown, E.N., Sottos, N.R. and White, S.R., 2002. Fracture testing of a self-healing polymer composite. *Experimental mechanics*, *42*(4), pp.372-379.

[3] Kessler, M.R. and White, S.R., 2001. Self-activated healing of delamination damage in woven composites. *Composites Part A: applied science and manufacturing*, *32*(5), pp.683-699.

[4] Xu, Y., Li, Y., Chen, Q., Fu, L., Tao, L. and Wei, Y., 2018. Injectable and self-healing chitosan hydrogel based on imine bonds: design and therapeutic applications. *International Journal of Molecular Sciences*, *19*(8), p.2198.

[5] Grandview research. Self-healing Materials Market Size, Share & Trends Analysis report by product, by technology, by application and segment forecast 2019:GVR-1-68038-829-9.

[6] Dhanaraju, G., Ben, B.S. and Pittala, R.K., 2022. Thermally remendable bismalemide-MWCNT/DA-epoxy nanocomposite via Diels-Alder bonding. Polymer, 245, p.124734.

[7] Dhanaraju, G., Golla, S., Ben, B.S. and Vikram, K.A., 2022. Interfacial and matrix healing of thermally reversible bismaleimide infused Graphene Nano Platelets reinforced polymer nanocomposite through Diels-Alder bonding. Materials Today Communications, 31, p.103753.

[8] Mali, G., Chauhan, A.N.S., Chavan, K.A. and Erande, R.D., 2021. Development and Applications of Double Diels-Alder Reaction in Organic Synthesis. Asian Journal of Organic Chemistry, 10(11), pp.2848-2868.

[9] Bubert, H., Haiber, S., Brandl, W., Marginean, G., Heintze, M. and Brüser, V., 2003. Characterization of the uppermost layer of plasma-treated carbon nanotubes. Diamond and Related Materials, *12*(3-7), pp.811-815.

[10] Angelidis, N., 2004. Damage sensing in CFRP composites using electrical potential techniques.

[11] Inoue, H. and Ogi, K., 2007. Piezoresistance behaviour of CFRP cross-ply laminates with transverse cracking. In Key Engineering Materials (Vol. 334, pp. 961-964). Trans Tech Publications Ltd.

[12] Chen, H.H., 2013. Damage Detection of Carbon Fiber Reinforced Polymer Using Electrical Measurement and Analysis of Acoustic Emission Signals (Doctoral dissertation, University of Akron).

[12] Wang, S. and Chung, D.D.L., 2002. Mechanical damage in carbon fiber polymer-matrix composite, studied by electrical resistance measurement. Composite interfaces, 9(1), pp.51-60.

[13] White, S.R., Blaiszik, B.J., Kramer, S.L., Olugebefola, S.C., Moore, J.S. and Sottos, N.R., 2011. Self-healing Polymers and Composites: Capsules, circulatory systems and chemistry allow materials to fix themselves. American Scientist, 99(5), pp.392-399.

[14] Ullah, H., Harland, A.R. and Silberschmidt, V.V., 2014. Evolution and interaction of damage modes in fabric-reinforced composites under dynamic flexural loading. Composites Science and Technology, 92, pp.55-63.

[15] Blaiszik, B.J., Kramer, S.L., Olugebefola, S.C., Moore, J.S., Sottos, N.R. and White, S.R., 2010. Self-healing polymers and composites. Annual review of materials research, 40(1), pp.179-211.

[16] Wen, J., Xia, Z. and Choy, F., 2011. Damage detection of carbon fiber reinforced polymer composites via electrical resistance measurement. Composites Part B: Engineering, 42(1), pp.77-86.

[17] De Luca, I., Pedram, P., Moeini, A., Cerruti, P., Peluso, G., Di Salle, A. and Germann, N., 2021. Nanotechnology development for formulating essential oils in wound dressing materials to promote the wound-healing process: A review. Applied Sciences, 11(4), p.1713.

[18] Willocq, B., Odent, J., Dubois, P. and Raquez, J.M., 2020. Advances in intrinsic self-healing polyurethanes and related composites. RSC advances, 10(23), pp.13766-13782.

[19] Pittala, R.K. and Ben, B.S., 2019. Synthesis and characterization of amine hardener filled microcapsules for self-healing composite applications. Materials Research Express, 6(11), p.115318.

[20] Zhang, M.Q. and Rong, M.Z., 2012. Theoretical consideration and modeling of self-healing polymers. Journal of Polymer Science Part B: Polymer Physics, 50(4), pp.229-241.

[21] Ghorbani, M., Ebrahimnezhad-Khaljiri, H., Eslami-Farsani, R. and Vafaeenezhad, H., 2021. The synergic effect of microcapsules and titanium nanoparticles on the self-healing and self-lubricating epoxy coatings: A dual smart application. Surfaces and Interfaces, 23, p.100998.

[22] Mohammadi, M.A., Eslami-Farsani, R. and Ebrahimnezhad-Khaljiri, H., 2020. Experimental investigation of the healing properties of the microvascular channels-based self-healing glass fibers/epoxy composites containing the three-part healant. Polymer Testing, 91, p.106862.

[23] Pang, J.W. and Bond, I.P., 2005. A hollow fibre reinforced polymer composite encompassing self-healing and enhanced damage visibility. Composites Science and Technology, 65(11-12), pp.1791-1799.

[24] Deng, W., You, Y. and Zhang, A., 2015. Supramolecular network-based self-healing polymer materials. In Recent advances in smart self-healing polymers and composites (pp. 181-210). Woodhead Publishing.

[25] Menon, A.V., Madras, G. and Bose, S., 2019. The journey of self-healing and shape memory polyurethanes from bench to translational research. Polymer Chemistry, 10(32), pp.4370-4388.

[26] Markvicheva EA, Kuz'kina IF, Pashkin II, Plechko TN, Kirsh YE, Zubov VP. A novel technique for entrapment of hybridoma cells in synthetic thermally reversible polymers. Biotechnology techniques. 1991 May 1;5(3):223-6.

[27] Ebrahimnezhad-Khaljiri, H. and Eslami-Farsani, R., 2021. Experimental investigation of flexural properties of glass fiber–epoxy self-healable composite structures containing capsulated epoxy healing agent and NiCl2 (imidazole) 4 catalyst. Journal of Industrial Textiles, 51(5), pp.788-805.

[28] Utrera-Barrios, S., Verdejo, R., López-Manchado, M.A. and Santana, M.H., 2020. Evolution of self-healing elastomers, from extrinsic to combined intrinsic mechanisms: A review. Materials Horizons, 7(11), pp.2882-2902.

[29] Brown, E.N., Kessler, M.R., Sottos, N.R. and White, S.R., 2003. In situ poly (urea-formaldehyde) microencapsulation of dicyclopentadiene. Journal of microencapsulation, 20(6), pp.719-730.

[30] Yang, J., Keller, M.W., Moore, J.S., White, S.R. and Sottos, N.R., 2008. Microencapsulation of isocyanates for self-healing polymers. Macromolecules, 41(24), pp.9650-9655.

[31] Liu, X., Sheng, X., Lee, J.K. and Kessler, M.R., 2009. Synthesis and characterization of melamine-urea-formaldehyde microcapsules containing ENB-based self-healing agents. Macromolecular Materials and Engineering, 294(6-7), pp.389-395.

[32] Su, Y.S. and Manthiram, A., 2012. Lithium–sulphur batteries with a microporous carbon paper as a bifunctional interlayer. Nature communications, 3(1), pp.1-6.

[33] Cho SH, Andersson HM, White SR, Sottos NR, Braun P V. Polydiniethylsiloxane-based self-healing materials. Adv Mater 2006;18:997–1000.

[34] Ollier RP, Penoff ME, Alvarez VA. Microencapsulation of epoxy resins : Optimization of synthesis conditions. Colloids Surfaces A Physicochem Eng Asp 2016;511:27–38. https://doi.org/10.1016/j.colsurfa.2016.09.081.

[35] Dry, C.M., 2000. Three designs for the internal release of sealants, adhesives, and waterproofing chemicals into concrete to reduce permeability. Cement and Concrete Research, 30(12), pp.1969-1977.

[36] Trask, R.S., Williams, G.J. and Bond, I.P., 2007. Bioinspired self-healing of advanced composite structures using hollow glass fibres. Journal of the royal society Interface, 4(13), pp.363-371.

[37] Banshiwal, J.K. and Tripathi, D.N., 2019. Self-healing polymer composites for structural application. Funct. Mater, 10, pp.1-13.

[38] Yuan YC, Yin T, Rong MZ, Zhang MQ. Self healing in polymers and polymer composites. Concepts, realization and outlook: A review. Express Polym Lett 2008;2:238–50. https://doi.org/10.3144/expresspolymlett.2008.29.

[39] Toohey, K.S., Sottos, N.R. and White, S.R., 2009. Characterization of microvascular-based self-healing coatings. Experimental Mechanics, 49(5), pp.707-717.

[40] Hansen, C.J., Wu, W., Toohey, K.S., Sottos, N.R., White, S.R. and Lewis, J.A., 2009. Self-healing materials with interpenetrating microvascular networks. Advanced Materials, 21(41), pp.4143-4147.

[41] Patrick, J.F., Hart, K.R., Krull, B.P., Diesendruck, C.E., Moore, J.S., White, S.R. and Sottos, N.R., 2014. Continuous self-healing life cycle in vascularized structural composites. Advanced materials, 26(25), pp.4302-4308.

[42] Haase, M.F., Grigoriev, D.O., Möhwald, H. and Shchukin, D.G., 2012. Development of nanoparticle stabilized polymer nanocontainers with high content of the encapsulated active agent and their application in water-borne anticorrosive coatings. Advanced Materials, 24(18), pp.2429-2435.

[43] Zhong, N. and Post, W., 2015. Self-repair of structural and functional composites with intrinsically self-healing polymer matrices: A review. Composites Part A: Applied Science and Manufacturing, 69, pp.226-239.

[44] Chung, C.M., Roh, Y.S., Cho, S.Y. and Kim, J.G., 2004. Crack healing in polymeric materials via photochemical [2+ 2] cycloaddition. Chemistry of Materials, 16(21), pp.3982-3984.

[45] Hinton, Z.R., Shabbir, A. and Alvarez, N.J., 2019. Dynamics of supramolecular self-healing recovery in extension. Macromolecules, 52(6), pp.2231-2242.

[46] Sijbesma, R.P., Beijer, F.H., Brunsveld, L., Folmer, B.J., Hirschberg, J.K., Lange, R.F., Lowe, J.K. and Meijer, E.W., 1997. Reversible polymers formed from self-complementary monomers using quadruple hydrogen bonding. Science, 278(5343), pp.1601-1604.

[47] Burattini, S., Greenland, B.W., Merino, D.H., Weng, W., Seppala, J., Colquhoun, H.M., Hayes, W., Mackay, M.E., Hamley, I.W. and Rowan, S.J., 2010. A healable supramolecular polymer blend based on aromatic π− π stacking and hydrogen-bonding interactions. Journal of the American Chemical Society, 132(34), pp.12051-12058.

[48] Burattini, S., Colquhoun, H.M., Fox, J.D., Friedmann, D., Greenland, B.W., Harris, P.J., Hayes, W., Mackay, M.E. and Rowan, S.J., 2009. A self-repairing, supramolecular polymer system: healability as a consequence of donor–acceptor π–π stacking interactions. Chemical communications, (44), pp.6717-6719.

[49] Grande, A.M., Coppi, S., Di Landro, L., Sala, G., Giacomuzzo, C., Francesconi, A. and Rahman, M.A., 2012, March. An experimental study of the self-healing behavior of ionomeric systems under ballistic impact tests. In Behavior and Mechanics of Multifunctional Materials and Composites 2012 (Vol. 8342, pp. 163-169). SPIE.

[50] Way, A.E., Hsu, L., Shanmuganathan, K., Weder, C. and Rowan, S.J., 2012. pH-responsive cellulose nanocrystal gels and nanocomposites. ACS Macro Letters, 1(8), pp.1001-1006.

[51] Anderson, C.A., Jones, A.R., Briggs, E.M., Novitsky, E.J., Kuykendall, D.W., Sottos, N.R. and Zimmerman, S.C., 2013. High-affinity DNA base analogs as supramolecular, nanoscale promoters of macroscopic adhesion. Journal of the American Chemical Society, 135(19), pp.7288-7295.

[52] Schmatloch, S., González, M.F. and Schubert, U.S., 2002. Metallo-supramolecular diethylene glycol: water-soluble reversible polymers. Macromolecular rapid communications, 23(16), pp.957-961.

[53] Li, C.H. and Zuo, J.L., 2020. Self-healing polymers based on coordination bonds. Advanced Materials, 32(27), p.1903762.

[54] Chen, X., Dam, M.A., Ono, K., Mal, A., Shen, H., Nutt, S.R., Sheran, K. and Wudl, F., 2002. A thermally re-mendable cross-linked polymeric material. Science, 295(5560), pp.1698-1702.

[55] Iacono, S.D., Martone, A. and Amendola, E., 2018. Diels-Alder Chemistry to Develop Self-Healing Epoxy Resins and Composites Thereof. Paint and Coatings Industry.

[56] Wool RP, O'Connor KM. A theory of crack healing in polymers. J Appl Phys 1981;52:5953–63. https://doi.org/10.1063/1.328526.

[57] Kim, Y.H. and Wool, R.P., 1983. A theory of healing at a polymer-polymer interface. Macromolecules, 16(7), pp.1115-1120.

[58] Jud, K. and Kausch, H.H., 1979. Load transfer through chain molecules after interpenetration at interfaces. Polymer Bulletin, 1(10), pp.697-707.

[59] Lin, C.B., Lee, S. and Liu, K.S., 1990. Methanol-Induced crack healing in poly (methyl methacrylate). Polymer Engineering & Science, 30(21), pp.1399-1406.

[60] Chen, X., Wudl, F., Mal, A.K., Shen, H. and Nutt, S.R., 2003. New thermally remendable highly cross-linked polymeric materials. Macromolecules, 36(6), pp.1802-1807.

[61] Liu, Y.L. and Hsieh, C.Y., 2006. Crosslinked epoxy materials exhibiting thermal remendablility and removability from multifunctional maleimide and furan compounds. Journal of Polymer Science Part A: Polymer Chemistry, 44(2), pp.905-913.

[62] Liu, Y.L. and Chen, Y.W., 2007. Thermally reversible cross-linked polyamides with high toughness and self-repairing ability from maleimide-and furan-functionalized aromatic polyamides. Macromolecular Chemistry and Physics, 208(2), pp.224-232.

[63] Plaisted, T.A. and Nemat-Nasser, S., 2007. Quantitative evaluation of fracture, healing and re-healing of a reversibly cross-linked polymer. Acta Materialia, 55(17), pp.5684-5696.

[64] Tian, Q., Rong, M.Z., Zhang, M.Q. and Yuan, Y.C., 2010. Synthesis and characterization of epoxy with improved thermal remendability based on Diels-Alder reaction. Polymer International, 59(10), pp.1339-1345.

[65] Barthel, M.J., Rudolph, T., Teichler, A., Paulus, R.M., Vitz, J., Hoeppener, S., Hager, M.D., Schacher, F.H. and Schubert, U.S., 2013. Self-healing materials via reversible crosslinking of poly (ethylene oxide)-block-poly (furfuryl glycidyl ether)(peo-b-pfge) block copolymer films. Advanced Functional Materials, 23(39), pp.4921-4932.

[66] Hilf, J., Scharfenberg, M., Poon, J., Moers, C. and Frey, H., 2015. Aliphatic Polycarbonates Based on Carbon Dioxide, Furfuryl Glycidyl Ether, and Glycidyl Methyl Ether: Reversible Functionalization and Cross-Linking. Macromolecular Rapid Communications, 36(2), pp.174-179.

[67] Deng, M., Guo, F., Liao, D., Hou, Z. and Li, Y., 2018. Aluminium-catalyzed terpolymerization of furfuryl glycidyl ether with epichlorohydrin and ethylene oxide: synthesis of thermoreversible polyepichlorohydrin elastomers with furan/maleimide covalent crosslinks. Polymer Chemistry, 9(1), pp.98-107.

[68] Araya-Hermosilla, R., Broekhuis, A.A. and Picchioni, F., 2014. Reversible polymer networks containing covalent and hydrogen bonding interactions. European Polymer Journal, 50, pp.127-134.

[69] Fischer, H.R. and García, S.J., 2016. Active protective coatings: Sense and heal concepts for organic coatings. In Active Protective Coatings (pp. 139-156). Springer, Dordrecht.

[70] Orozco, F., Niyazov, Z., Garnier, T., Migliore, N., Zdvizhkov, A.T., Raffa, P., Moreno-Villoslada, I., Picchioni, F. and Bose, R.K., 2021. Maleimide Self-Reaction in Furan/Maleimide-Based Reversibly Crosslinked Polyketones: Processing Limitation or Potential Advantage?. Molecules, 26(8), p.2230.

[71] Zolghadr, M., Shakeri, A., Zohuriaan-Mehr, M.J. and Salimi, A., 2019. Self-healing semi-IPN materials from epoxy resin by solvent-free furan–maleimide Diels–Alder polymerization. Journal of Applied Polymer Science, 136(40), p.48015.

[72] Farshchi, N., Gedan-Smolka, M. and Stommel, M., 2021. Preparation and Characterization of Self-Healing Polyurethane Powder Coating Using Diels–Alder Reaction. Polymers, 13(21), p.3803.

[73] Xu, Z., Zhao, Y., Wang, X. and Lin, T., 2013. A thermally healable polyhedral oligomeric silsesquioxane (POSS) nanocomposite based on Diels–Alder chemistry. Chemical communications, 49(60), pp.6755-6757.

[74] Tian, Q., Yuan, Y.C., Rong, M.Z. and Zhang, M.Q., 2009. A thermally remendable epoxy resin. Journal of Materials Chemistry, 19(9), pp.1289-1296.

[75] Amendola, E. and National Research Council, 2015. Epoxy thermosets with self-healing ability. Journal of Materials Science and Chemical Engineering, 3(07), p.162.

[76] Allen, M.J., Tung, V.C. and Kaner, R.B., 2010. Honeycomb carbon: a review of graphene. Chemical reviews, 110(1), pp.132-145.

[77] Zhu, Y., Murali, S., Cai, W., Li, X., Suk, J.W., Potts, J.R. and Ruoff, R.S., 2010. Graphene and graphene oxide: synthesis, properties, and applications. Advanced materials, 22(35), pp.3906-3924.

[78] Forro, L., Salvetat, J.P., Bonard, J.M., Bacsa, R., Thomson, N.H., Garaj, S., Thien-Nga, L., Gaal, R., Kulik, A., Ruzicka, B. and Degiorgi, L., 2002. Electronic and mechanical properties of carbon nanotubes. In Science and Application of Nanotubes (pp. 297-320). Springer, Boston, MA.

[79] Lee, C., Wei, X., Kysar, J.W. and Hone, J., 2008. Measurement of the elastic properties and intrinsic strength of monolayer graphene. science, 321(5887), pp.385-388.

[80] Zakaria, M.R., Kudus, M.H.A., Akil, H.M. and Thirmizir, M.Z.M., 2017. Comparative study of graphene nanoparticle and multiwall carbon nanotube filled epoxy nanocomposites based on mechanical, thermal and dielectric properties. Composites Part B: Engineering, 119, pp.57-66.

[81] Ates, M., Eker, A.A. and Eker, B., 2017. Carbon nanotube-based nanocomposites and their applications. Journal of adhesion science and Technology, 31(18), pp.1977-1997.

[82] Fiedler, B., Gojny, F.H., Wichmann, M.H., Nolte, M.C. and Schulte, K., 2006. Fundamental aspects of nano-reinforced composites. Composites science and technology, 66(16), pp.3115-3125.

[83] Stankovich, S., Dikin, D.A., Dommett, G.H., Kohlhaas, K.M., Zimney, E.J., Stach, E.A., Piner, R.D., Nguyen, S.T. and Ruoff, R.S., 2006. Graphene-based composite materials. nature, 442(7100), pp.282-286.

[84] Park, M.J., Lee, J.K., Lee, B.S., Lee, Y.W., Choi, I.S. and Lee, S.G., 2006. Covalent modification of multiwalled carbon nanotubes with imidazolium-based ionic liquids: effect of anions on solubility. Chemistry of materials, 18(6), pp.1546-1551.

[85] Economopoulos, S.P., Rotas, G., Miyata, Y., Shinohara, H. and Tagmatarchis, N., 2010. Exfoliation and chemical modification using microwave irradiation affording highly functionalized graphene. ACS nano, 4(12), pp.7499-7507.

[86] Andrade-Guel, M., Cabello-Alvarado, C., Cruz-Delgado, V.J., Bartolo-Perez, P., De León-Martínez, P.A., Sáenz-Galindo, A., Cadenas-Pliego, G. and Ávila-Orta, C.A., 2019. Surface modification of graphene nanoplatelets by organic acids and ultrasonic radiation for enhance uremic toxins adsorption. Materials, 12(5), p.715.

[87] Kathi, J., Rhee, K.Y. and Lee, J.H., 2009. Effect of chemical functionalization of multi-walled carbon nanotubes with 3-aminopropyltriethoxysilane on mechanical and morphological properties of epoxy nanocomposites. Composites Part A: Applied Science and Manufacturing, 40(6-7), pp.800-809.

[88] Lee, J.H., Rhee, K.Y. and Park, S.J., 2011. Effects of silane modification and temperature on tensile and fractural behaviors of carbon nanotube/epoxy nanocomposites. Journal of Nanoscience and Nanotechnology, 11(1), pp.275-280.

[89] Nie, Y. and Hübert, T., 2012. Surface modification of carbon nanofibers by glycidoxysilane for altering the conductive and mechanical properties of epoxy composites. Composites Part A: Applied Science and Manufacturing, 43(8), pp.1357-1364.

[90] Xu, Z., Zhao, Y., Wang, X. and Lin, T., 2013. A thermally healable polyhedral oligomeric silsesquioxane (POSS) nanocomposite based on Diels–Alder chemistry. Chemical communications, 49(60), pp.6755-6757.

[91] Wang, F., Drzal, L.T., Qin, Y. and Huang, Z., 2016. Effects of functionalized graphene nanoplatelets on the morphology and properties of epoxy resins. High Performance Polymers, 28(5), pp.525-536.

[92] Lin, C., Sheng, D., Liu, X., Xu, S., Ji, F., Dong, L., Zhou, Y. and Yang, Y., 2017. A self-healable nanocomposite based on dual-crosslinked Graphene Oxide/Polyurethane. Polymer, 127, pp.241-250.

[93] Ma, P.C., Kim, J.K. and Tang, B.Z., 2007. Effects of silane functionalization on the properties of carbon nanotube/epoxy nanocomposites. Composites science and technology, 67(14), pp.2965-2972.

[94] Yaghoubi, A. and Nikje, M.M.A., 2018. Silanization of multi-walled carbon nanotubes and the study of its effects on the properties of polyurethane rigid foam nanocomposites. Composites Part A: Applied Science and Manufacturing, 109, pp.338-344.

[95] Ayatollahi, M.R., Shadlou, S. and Shokrieh, M.M., 2011. Fracture toughness of epoxy/multi-walled carbon nanotube nano-composites under bending and shear loading conditions. Materials & Design, 32(4), pp.2115-2124.

[96] Shekar, K.C., Prasad, B.A. and Prasad, N.E., 2014. Effect of amino multi walled carbon nanotubes reinforcement on the flexural properties of neat epoxy. In Applied mechanics and materials (Vol. 592, pp. 912-916). Trans Tech Publications Ltd.

[97] Lee, J.H., Rhee, K.Y. and Park, S.J., 2010. The tensile and thermal properties of modified CNT-reinforced basalt/epoxy composites. Materials Science and Engineering: A, 527(26), pp.6838-6843.

[98] Park, J.S., Darlington, T., Starr, A.F., Takahashi, K., Riendeau, J. and Hahn, H.T., 2010. Multiple healing effect of thermally activated self-healing composites based on Diels–Alder reaction. Composites Science and Technology, 70(15), pp.2154-2159.

[99] Kostopoulos, V., Kotrotsos, A., Sousanis, A. and Sotiriadis, G., 2019. Fatigue behaviour of open-hole carbon fibre/epoxy composites containing bis-maleimide based polymer blend interleaves as self-healing agent. Composites Science and Technology, 171, pp.86-93.

[100] Zhang, W., Duchet, J. and Gérard, J.F., 2014. Self-healable interfaces based on thermo-reversible Diels–Alder reactions in carbon fiber reinforced composites. Journal of colloid and interface science, 430, pp.61-68.

[101] Kotrotsos, A., Tsokanas, P., Tsantzalis, S. and Kostopoulos, V., 2019. Healing of carbon fiber reinforced plastics by Diels–Alder based polymers: Effects of healing agent concentration and curing cycle. Journal of Applied Polymer Science, 136(19), p.47478.

[102] Mauldin, T.C. and Kessler, M.R., 2010. Self-healing polymers and composites. International Materials Reviews, 55(6), pp.317-346.

[103] Kirkby, E.L., Rule, J.D., Michaud, V.J., Sottos, N.R., White, S.R. and Månson, J.A.E., 2008. Embedded shape-memory alloy wires for improved performance of self-healing polymers. Advanced Functional Materials, 18(15), pp.2253-2260.

[104] Shokrian, M.D., Shelesh-Nezhad, K. and Najjar, R., 2019. Toughening effect of nanocomposite-wall microcapsules on the fracture behavior of epoxy. Polymer, 168, pp.104-115.

[105] Jin, H., Miller, G.M., Sottos, N.R. and White, S.R., 2011. Fracture and fatigue response of a self-healing epoxy adhesive. Polymer, 52(7), pp.1628-1634.

[106] Abdelal, N.R., Al-Saleh, M.H. and Irshidat, M.R., 2018. Utilizing vacuum bagging process to prepare carbon fiber/CNT-modified-epoxy composites with improved mechanical properties. Polymer-Plastics Technology and Engineering, 57(3), pp.175-184.

[107] Zeng, C., Seino, H., Ren, J., Hatanaka, K. and Yoshie, N., 2013. Self-healing bio-based furan polymers cross-linked with various bis-maleimides. Polymer, 54(20), pp.5351-5357.

[108] Shabani, P., Shokrieh, M.M. and Saeedi, A., 2020. A novel model to simulate the formation and healing of cracks in self-healing cross-ply composites under flexural loading. Composite Structures, 235, p.111750.

[109] Peterson, A.M., Jensen, R.E. and Palmese, G.R., 2011. Thermoreversible and remendable glass–polymer interface for fiber-reinforced composites. Composites Science and Technology, 71(5), pp.586-592.

[110] Wu P, Liu L, Wu Z. Synthesis of Diels-Alder Reaction-Based Remendable Epoxy Matrix and Corresponding Self-healing Efficiency to Fibrous Composites. Macromolecular Materials and Engineering. 2020 Oct;305(10):2000359.

[111] Post, W., Cohades, A., Michaud, V., Van Der Zwaag, S. and Garcia, S.J., 2017. Healing of a glass fibre reinforced composite with a disulphide containing organic-inorganic epoxy matrix. Composites Science and Technology, 152, pp.85-93.

[112] Sakellariou, G., Ji, H., Mays, J.W., Hadjichristidis, N. and Baskaran, D., 2007. Controlled covalent functionalization of multiwalled carbon nanotubes using [4+ 2] cycloaddition of benzocyclobutenes. Chemistry of Materials, 19(26), pp.6370-6372.

[113] Roos, K., Dolci, E., Carlotti, S. and Caillol, S., 2016. Activated anionic ring-opening polymerization for the synthesis of reversibly cross-linkable poly (propylene oxide) based on furan/maleimide chemistry. Polymer Chemistry, 7(8), pp.1612-1622.

[114] Tian, Q., Rong, M.Z., Zhang, M.Q. and Yuan, Y.C., 2010. Synthesis and characterization of epoxy with improved thermal remendability based on Diels-Alder reaction. Polymer International, 59(10), pp.1339-1345.
[115] Sadek, E.M., El-Nashar, D.E., Ward, A.A. and Ahmed, S.M., 2018. Study on the properties of multi-walled carbon nanotubes reinforced poly (vinyl alcohol) composites. Journal of Polymer Research, 25, pp.1-13.

[116] Siddiqui, N.A., Woo, R.S., Kim, J.K., Leung, C.C. and Munir, A., 2007. Mode I interlaminar fracture behavior and mechanical properties of CFRPs with nanoclay-filled epoxy matrix. Composites Part A: Applied science and manufacturing, 38(2), pp.449-460.

[117] Aliyeva, S., Alosmanov, R., Buniyatzadeh, I., Eyvazova, G., Azizov, A. and Maharramov, A., 2019. Functionalized graphene nanoplatelets/modified polybutadiene hybrid composite. Colloid and Polymer Science, 297, pp.1529-1540.

[118] Yadav, S.K. and Cho, J.W., 2013. Functionalized graphene nanoplatelets for enhanced mechanical and thermal properties of polyurethane nanocomposites. Applied surface science, 266, pp.360-367.

[119] Moriche, R., Prolongo, S.G., Sánchez, M., Jiménez-Suárez, A., Sayagués, M.J. and Ureña, A., 2015. Morphological changes on graphene nanoplatelets induced during dispersion into an epoxy resin by different methods. Composites Part B: Engineering, 72, pp.199-205.

[120] Gupta, R. and Singh, B., 2019. Enhancement of electrical conductivity and magnetic properties of bimetallic Schiff base complex on grafting to MWCNTs. Journal of Materials Science: Materials in Electronics, 30, pp.11888-11906.

[121] Manafi, P., Ghasemi, I., Karrabi, M., Azizi, H., Manafi, M.R. and Ehsaninamin, P., 2015. Thermal stability and thermal degradation kinetics (model-free kinetics) of nanocomposites based on poly (lactic acid)/graphene: the influence of functionalization. Polymer Bulletin, 72, pp.1095-1112.

[122] Tang, H., Song, N., Gao, Z., Chen, X., Fan, X., Xiang, Q. and Zhou, Q., 2007. Synthesis and properties of 1, 3, 4-oxadiazole-containing high-performance bismaleimide resins. Polymer, 48(1), pp.129-138.

[123] Bindu, P. and Thomas, S., 2014. Estimation of lattice strain in ZnO nanoparticles: X-ray peak profile analysis. Journal of Theoretical and Applied Physics, 8, pp.123-134.

[124] Chang, C.M. and Liu, Y.L., 2009. Functionalization of multi-walled carbon nanotubes with furan and maleimide compounds through Diels–Alder cycloaddition. Carbon, 47(13), pp.3041-3049.

[125] Vigolo, B., Mamane, V., Valsaque, F., Le, T.H., Thabit, J., Ghanbaja, J., Aranda, L., Fort, Y. and McRae, E., 2009. Evidence of sidewall covalent functionalization of single-walled carbon nanotubes and its advantages for composite processing. Carbon, 47(2), pp.411-419.

[126] Batakliev, T., Petrova-Doycheva, I., Angelov, V., Georgiev, V., Ivanov, E., Kotsilkova, R., Casa, M., Cirillo, C., Adami, R., Sarno, M. and Ciambelli, P., 2019. Effects of graphene nanoplatelets and multiwall carbon nanotubes on the structure and mechanical properties of poly (lactic acid) composites: a comparative study. Applied Sciences, 9(3), p.469.

[127] Halder, N.C. and Wagner, C.N.J., 1966. Separation of particle size and lattice strain in integral breadth measurements. Acta Crystallographica, 20(2), pp.312-313.

[128] Ma, P.C., Kim, J.K. and Tang, B.Z., 2006. Functionalization of carbon nanotubes using a silane coupling agent. Carbon, 44(15), pp.3232-3238.

[129] Liang, F., Sadana, A.K., Peera, A., Chattopadhyay, J., Gu, Z., Hauge, R.H. and Billups, W.E., 2004. A convenient route to functionalized carbon nanotubes. Nano Letters, 4(7), pp.1257-1260.

[130] Nath, D., Singh, F. and Das, R., 2020. X-ray diffraction analysis by Williamson-Hall, Halder-Wagner and size-strain plot methods of CdSe nanoparticles-a comparative study. Materials Chemistry and Physics, 239, p.122021.

[131] Lavorgna, M., Romeo, V., Martone, A., Zarrelli, M., Giordano, M., Buonocore, G.G., Qu, M.Z., Fei, G.X. and Xia, H.S., 2013. Silanization and silica enrichment of multiwalled carbon nanotubes: Synergistic effects on the thermal-mechanical properties of epoxy nanocomposites. European polymer journal, 49(2), pp.428-438.

[132] Kathi, J. and Rhee, K.Y., 2008. Surface modification of multi-walled carbon nanotubes using 3-aminopropyltriethoxysilane. Journal of Materials Science, 43, pp.33-37.

[133] Vennerberg, D., Hall, R. and Kessler, M.R., 2014. Supercritical carbon dioxide-assisted silanization of multi-walled carbon nanotubes and their effect on the thermo-mechanical properties of epoxy nanocomposites. Polymer, 55(16), pp.4156-4163.

[134] Bello, R.H., Coelho, L.A. and Becker, D., 2018. Role of chemical funcionalization of carbon nanoparticles in epoxy matrices. Journal of Composite Materials, 52(4), pp.449-464.

[135] Hoa, S.V., 2009. Principles of the manufacturing of composite materials. DEStech Publications, Inc.

[136] Li, C., Tan, J., Gu, J., Qiao, L., Zhang, B. and Zhang, Q., 2016. Rapid and efficient synthesis of isocyanate microcapsules via thiol-ene photopolymerization in Pickering emulsion and its application in self-healing coating. Composites science and technology, 123, pp.250-258.

[137] Shen, B., Zhai, W., Tao, M., Lu, D. and Zheng, W., 2013. Chemical functionalization of graphene oxide toward the tailoring of the interface in polymer composites. Composites Science and Technology, 77, pp.87-94.

[138] Li, Q.T., Jiang, M.J., Wu, G., Chen, L., Chen, S.C., Cao, Y.X. and Wang, Y.Z., 2017. Photothermal conversion triggered precisely targeted healing of epoxy resin based on thermoreversible diels–alder network and amino-functionalized carbon nanotubes. ACS applied materials & interfaces, 9(24), pp.20797-20807.

[139] Koval'chuk, A.A., Shevchenko, V.G., Shchegolikhin, A.N., Nedorezova, P.M., Klyamkina, A.N. and Aladyshev, A.M., 2008. Effect of carbon nanotube functionalization on the structural and mechanical properties of polypropylene/MWCNT composites. Macromolecules, 41(20), pp.7536-7542.

[140] Chen, Q., Wu, W., Zhao, Y., Xi, M., Xu, T. and Fong, H., 2014. Nano-epoxy resins containing electrospun carbon nanofibers and the resulting hybrid multi-scale composites. Composites Part B: Engineering, 58, pp.43-53.

[141] Chou, T.W., Gao, L., Thostenson, E.T., Zhang, Z. and Byun, J.H., 2010. An assessment of the science and technology of carbon nanotube-based fibers and composites. Composites Science and Technology, 70(1), pp.1-19.

[142] Sharma, H., Kumar, A., Rana, S. and Guadagno, L., 2022. An overview on carbon fiber-reinforced epoxy composites: effect of graphene oxide incorporation on composites performance. Polymers, 14(8), p.1548.

[143] Sánchez, M., Campo, M., Jiménez-Suárez, A. and Ureña, A., 2013. Effect of the carbon nanotube functionalization on flexural properties of multiscale carbon fiber/epoxy composites manufactured by VARIM. Composites Part B: Engineering, 45(1), pp.1613-1619.

[144] Fan, Z., Santare, M.H. and Advani, S.G., 2008. Interlaminar shear strength of glass fiber reinforced epoxy composites enhanced with multi-walled carbon nanotubes. Composites Part A: Applied science and manufacturing, 39(3), pp.540-554.

[145] Wan, Y.J., Gong, L.X., Tang, L.C., Wu, L.B. and Jiang, J.X., 2014. Mechanical properties of epoxy composites filled with silane-functionalized graphene oxide. Composites Part A: Applied Science and Manufacturing, 64, pp.79-89.

[146] Pathak, A.K., Borah, M., Gupta, A., Yokozeki, T. and Dhakate, S.R., 2016. Improved mechanical properties of carbon fiber/graphene oxide-epoxy hybrid composites. Composites Science and Technology, 135, pp.28-38.

[147] Khan, S.U., Li, C.Y., Siddiqui, N.A. and Kim, J.K., 2011. Vibration damping characteristics of carbon fiber-reinforced composites containing multi-walled carbon nanotubes. Composites science and technology, 71(12), pp.1486-1494.

[148] Tehrani, M., Boroujeni, A.Y., Hartman, T.B., Haugh, T.P., Case, S.W. and Al-Haik, M.S., 2013. Mechanical characterization and impact damage assessment of a woven carbon fiber reinforced carbon nanotube–epoxy composite. Composites Science and Technology, 75, pp.42-48.

[149] Harris, B., 2003. A historical review of the fatigue behaviour of fibre-reinforced plastics. In Fatigue in composites (pp. 3-35). Woodhead Publishing.

[150] Pekturk, H.Y., Elitas, M., Goktas, M., Demir, B. and Birhanu, S., 2022. Evaluation of the effect of MWCNT amount and dispersion on bending fatigue properties of non-crimp CFRP composites. Engineering Science and Technology, an International Journal, 34, p.101081.

[151] Brown, E.N., 2011. Use of the tapered double-cantilever beam geometry for fracture toughness measurements and its application to the quantification of self-healing. The Journal of Strain Analysis for Engineering Design, 46(3), pp.167-186.

[152] Tsangouri, E., Aggelis, D. and Van Hemelrijck, D., 2015. Quantifying thermoset polymers healing efficiency: a systematic review of mechanical testing. Progress in Polymer Science, 49, pp.154-174.

[153] Wu, G., Ma, L., Liu, L., Wang, Y., Xie, F., Zhong, Z., Zhao, M., Jiang, B. and Huang, Y., 2016. Interface enhancement of carbon fiber reinforced methylphenylsilicone resin composites modified with silanized carbon nanotubes. Materials & Design, 89, pp.1343-1349.

[154] Di Franco, G., Marannano, G., Pasta, A. and VIRZI'MARIOTTI, G., 2011. Design and use of a fatigue test machine in plane bending for composite specimens and bonded joints. In Advances in Composite Materials-Ecodesign and Analysis (Vol. 2011, pp. 491-516). InTech.

[155] Fronk, T.H., Akula, V.M. and Fugal, S.R., 2002, June. Passive damping of laminated composite materials with engineered defects. In Smart structures and materials 2002: damping and isolation (Vol. 4697, pp. 43-50). SPIE.

List of publication

a) International Journals

1) Dhanaraju G, Ben BS, Pittala RK. Thermally remendable bismalemide-MWCNT/DA-epoxy nanocomposite via Diels-Alder bonding. Polymer. 2022 Apr 6;245:124734. https://doi.org/10.1016/j.polymer.2022.124734 **(SCI) IF:4.43**

2) Dhanaraju G, Golla S, Ben BS, Vikram KA. Interfacial and matrix healing of thermally reversible bismaleimide infused Graphene Nano Platelets reinforced polymer nanocomposite through Diels-Alder bonding. Materials Today Communications. 2022 Jun 1;31:103753. https://doi.org/10.1016/j.mtcomm.2022.103753 **(SCI) IF:3.662**

3) Dhanaraju G, Raj Kumar Pittala, B Satish Ben, B Avinash Ben Amine functionalization with maleimide grafted MWCNT - CFRP composite interfacial healing and mechanical performance through thermally reversible cycloaddition **(Under Review)**

4) Dhanaraju G, Raj Kumar Pittala, B Satish Ben, V Suresh Babu. Evaluation of exfoliation level effect by oxidation followed by silane functionalized MWCNT infusion on mechanical performance and damping behavior of CFRP composites **(Under Review)**

b) International conferences

1) Dhanaraju. G, Raj Kumar Pittala, B Satish Ben, Synthesis and Characterization of Thermally Remendable Epoxy Polymer Composite through Diels-Alder Bonding, ICRAM, Aug, 25-27, 2022, IIT Jodhpur